ENERGY RESOLUTION OF A LITHIUM-DRIFTED SILICON SEMICONDUCTOR DETECTOR ALPHA PARTICLE SPECTROMETER

by

ROBERT ALAN NUTTELMAN

B. S, Kansas State University, 1967

A MASTER'S THESIS

submitted in partial fulfillment of the
requirements for the degree

MASTER OF SCIENCE

Department of Nuclear Engineering
KANSAS STATE UNIVERSITY
Manhattan, Kansas

1969

Approved by:

N. Dean Eckhoff

Richard E. Faw

Major Professors

TABLE OF CONTENTS

		Page
1.0	INTRODUCTION.	1
2.0	THEORETICAL DEVELOPMENT	3
	2.1 Theory of Energy Resolution Spreading	3
	2.2 Particle Statistics in the Detector	8
	2.3 Incomplete Charge Collection.	10
	2.4 Fluctuations of the Energy Loss for an Alpha Particle Traversing a Thin Absorber.	12
	2.5 Amplifier and Detector Equivalent Circuit	13
	2.6 Detector Signal.	15
	2.7 Energy Resolution Spreading Due to Amplifier and Detector Noise.	16
	2.8 Summary of Theoretical Expressions	34
3.0	EXPERIMENTAL DEVELOPMENT.	36
	3.1 Theory.	36
	3.2 Apparatus	38
	3.3 Determination of Detector Capacitance	44
	3.4 Instrument Checkout and Calibration	51
	3.5 Procedure	54
4.0	RESULTS AND DISCUSSION.	58
	4.1 Amplifier Noise Contribution to Energy Resolution Spreading.	58
	4.2 Detector Noise Contribution to Energy Resolution Spreading	60
	4.3 Spectrometer Response to ^{241}Am Alpha Particles.	68
	4.4 Conclusions	82

TABLE OF CONTENTS (continued)

		Page
5.0	SUGGESTIONS FOR FURTHER STUDY.	83
6.0	ACKNOWLEDGEMENTS.	84
7.0	LITERATURE CITED.	85
8.0	APPENDIX A (Theory of the Lithium-Drifted Semiconductor Detector).	87
9.0	APPENDIX B (Variance and Mean of the Total Energy Resolution Spreading Normal Distribution Due to Normally Distributed Energy Resolution Effects)	94
10.	APPENDIX C (Relationship Between the FWHM and Standard Deviation of a Normal Pulse-Height Energy Distribution).	98
11.	APPENDIX D (Determination of the Mean Energy Loss and Energy Loss Variance Due to Source Self-Absorption).	100
12.	APPENDIX E (Determination of the Mean Energy Loss and Energy Loss Variance Due to the Detector Window).	102
13.	APPENDIX F (Calculation of Detector Capacitance)	104
14.	APPENDIX G (Tabulated Experimental Results).	105

LIST OF TABLES

Page

I. Equipment List. 47

II. Alpha particle energy spectrum FWHM for different data fitting procedures. 74

LIST OF FIGURES

		Page
1.	Ideal Alpha Particle Energy Distribution.	4
2.	Actual Alpha Particle Energy Distribution	4
3.	Effects of Energy Resolution Spreading Upon an Ideal Alpha Particle Energy Distribution.	7
4.	Energy Distribution of Uncollimated Alpha Particles from a Point Monoenergetic Source After Traversing a Thin Absorber .	7
5.	Equivalent Circuit of the Detector, Amplifier, and Time Constant Circuitry.	14
6.	Theoretical Voltage Pulse from the Detector.	14
7.	Equivalent Circuit of the Thermal Noise Generator.	18
8.	Circuit Used to Determine $V_{BB'_{max}}/V_{AA'_{max}}$	28
9.	Block Diagram of the Alpha Particle Spectrometer.	39
10.	Equipment Comprising the Alpha Particle Spectrometer.	40
11.	^{241}Am Alpha Particle Source	41
12.	Lithium-Drifted Silicon Semiconductor Detector.	41
13.	Uncovered Detector Vacuum Chamber Showing Alpha Particle Source, Shutter, Detector, and Heat Sink.	42
14.	Detail of Vacuum System and Detector Chamber Cooling Bath . .	45
15.	4096 Channel Pulse-Height Analyzer.	46
16.	Equipment Used to Measure Detector Capacitance.	49
17.	Circuit Used to Measure Detector Capacitance.	50
18.	Detector Capacitance Calibration Curve.	52
19.	Check of Pulse-Height Analyzer Integral Linearity	55
20.	Energy Resolution Spreading Due to Amplifier Noise as a Function of Amplifier Time Constant	59
21.	Detector Leakage Current Variation with Detector Bias Voltage	61

22. Variation of Energy Resolution Spreading Due to Detector Noise with Detector Leakage Current (τ = 0.8 μsec) 63

23. Variation of Energy Resolution Spreading Due to Detector Noise with Amplifier Time Constant (Detector Bias = 40 Volts). . 65

24. Variation of Energy Resolution Spreading Due to Detector Noise with Amplifier Time Constant (Detector Bias = 70 Volts). . 66

25. Variation of Energy Resolution Spreading Due to Detector Noise with Amplifier Time Constant (Detector Bias = 100 Volts) 67

26. Least Squares Fit of Several Functions to the Energy Resolution Spreading FWHM Due to Detector Noise as a Function of $I_d\tau$. 69

27. Measured Alpha Particle Energy Spectrum Showing Three Different Data Fitting Procedures (V_{bias} = 40 Volts and τ = 0.4 μsec). . . 70

28. Measured Alpha Particle Energy Spectrum Showing Three Different Data Fitting Procedures (V_{bias} = 100 Volts and τ = 0.4 μsec) . . 71

29. Variation of the Energy Resolution of the Spectrometer to ^{241}Am Alpha Particles with Detector Bias Voltage (τ = 0.8 μsec). 75

30. Variation of the Energy Resolution of the Spectrometer to ^{241}Am Alpha Particles with Amplifier Time Constant (V_{bias} = 40 Volts) . 76

31. Variation of the Energy Resolution of the Spectrometer to ^{241}Am Alpha Particles with Amplifier Time Constant (V_{bias} = 70 Volts) . 77

32. Variation of the Energy Resolution of the Spectrometer to ^{241}Am Alpha Particles with Amplifier Time Constant (V_{bias} = 100 Volts). 78

33. Variation of Excess Energy Resolution Spreading FWHM with Detector Bias Voltage (τ = 0.8 μsec). 80

34. Variation of Excess Energy Resolution Spreading FWHM with Amplifier Time Constant (V_{bias} = 40, 70, and 100 Volts). 81

NOMENCLATURE

A	Detector area
e	Electronic charge
E_o	Emitted energy of alpha particle
E_{RMS}	Root-mean-squared voltage at amplifier output
$\overline{E}$	Mean, or most probably alpha particle energy
$\overline{E}_o'$	Mean energy of alpha particles after traversing the source window
f	Frequency
F	Fano factor
F_{sc}^2	Space charge smoothing factor
FWHM	Full-width at half-maximum
G_o	Frequency independent amplifier gain
g_m	Vacuum tube mutual conductance
$\langle i^2 \rangle$	Mean squared value of the current i
I_a	Vacuum tube mean anode current
I_d	Detector leakage current
I_g	Vacuum tube grid current
k	Boltzmann's constant
k'	Dielectric constant of silicon
$p(E)$	Probability density per unit energy
PHA	Pulse-height analyzer
Q	Total charge collected in the detector per incident particle
R	Total amplifier input shunt resistance
RMS	Root-mean-squared

T	Temperature
t_c	Detector collection time
t_l	Mean free carrier time
$\langle v^2 \rangle$	Mean squared value of the voltage v
V_{bias}	Detector bias voltage
VTVM	Vacuum tube voltmeter
w	Mean energy required to produce one ion pair (electron-hole pair) in silicon
window	Thin alpha particle absorbing material
W	Energy of alpha particle entering sensitive region of the detector
W_{dd}	Detector depletion depth
ε	Base of natural logarithms (2.718)
ε_1	$\overline{E}_o' / E_o$
σ	Standard deviation
σ^2	Variance
ΣC	Total amplifier input capacitance
τ	Amplifier time constant
ω	Angular frequency

1.0 INTRODUCTION

Semiconductor detectors have become an important tool in charged particle energy spectroscopy. For some uses these devices have been shown to possess energy resolution characteristics second only to mass spectrographs. However, mass spectrographs suffer from high cost and low counting efficiency, shortcomings not characteristic of semiconductor detectors.

Lithium-drifted semiconductor detectors have been shown to possess good energy resolution at room temperature and relatively thick sensitive regions to absorb the energy of high energy charged particles. They suffer from charge collection difficulties and a relatively high noise level compared to other types of semiconductor detectors. A brief discussion of lithium-drifted detectors is given in Appendix A.

Goulding and Hansen (10) have studied the effect of detector and amplifier noise on the energy resolution of semiconductor junction radiation detectors. Monteith (18) has correlated detector leakage current with detector noise in lithium-drifted semiconductor detectors and predicted the effect of this noise upon detector energy resolution. Masuda and Takeda (17) have studied the problem of leakage current and noise in surface barrier type semiconductor detectors.

The purpose of this work is to study the energy resolution of a lithium-drifted semiconductor detector and its associated electronics to 5.477 MeV alpha particles from an ^{241}Am source. The effects on resolution of varying the detector bias voltage, amplifier time constant, and detector temperature were studied. Theoretical expressions were reviewed for the resolution degradation due to amplifier noise, detector noise, particle statistics, and

detector "window". These expressions were used with a given value for the alpha particle source self-absorption to predict the full-width-at-half-maximum (FWHM) of an alpha particle energy spectrum. Theoretical values of the amplifier and detector noise and FWHM of the alpha spectrum were compared with experimental values.

2.0 THEORETICAL DEVELOPMENT

2.1 Theory of Energy Resolution Spreading

In an experiment designed to measure the energy of monoenergetic alpha particles, the following events occur. Alpha particles impinging on the detector release charge in proportion to the incident alpha particle energy absorbed. Associated electronic equipment convert the charge pulses to voltage pulses, amplify, and further process the signal. A multichannel pulse-height analyzer (PHA) sorts the amplified voltage pulses according to height (magnitude of voltage) and stores this information. Pulse heights are assumed to be proportional to the alpha particle energies. Ideally, for monoenergetic incident alpha particles, an energy distribution similar to Fig. (1) would be expected. All particles would be of energy E_o. In practice, this degree of energy resolution is never achieved. The actual results of the experiment described above are shown in Fig. (2). It can be seen in Fig. (2) that all alpha particles counted by the multichannel analyzer do not have the same energy. There is now a "spread" or distribution of energies. $\overline{E}$ corresponds to the mean, or most probable energy.

Resolution, as defined for this study is a measure of the width of the distribution of Fig. (2). Energy resolution spreading refers to various effects acting to increase the width of the energy distribution. Good resolution generally means a narrow energy distribution, and poor resolution refers to a relatively wide energy distribution exhibiting much energy resolution spreading.

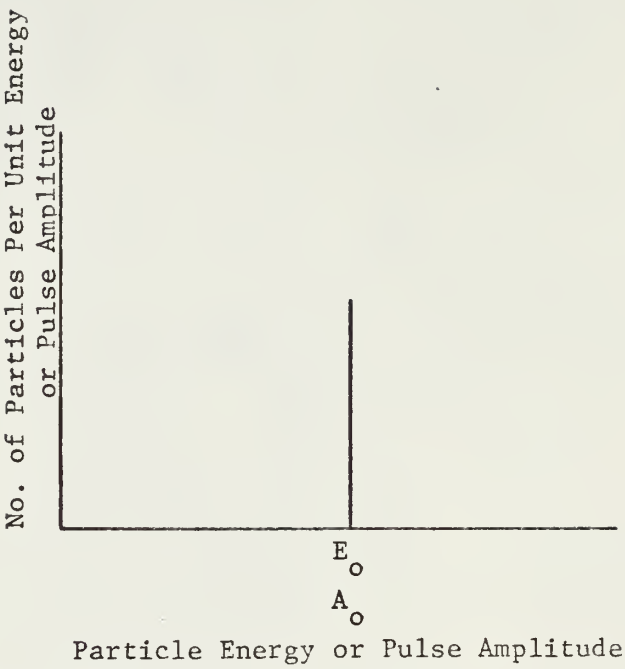

Fig. 1. Ideal Alpha Particle Energy Distribution

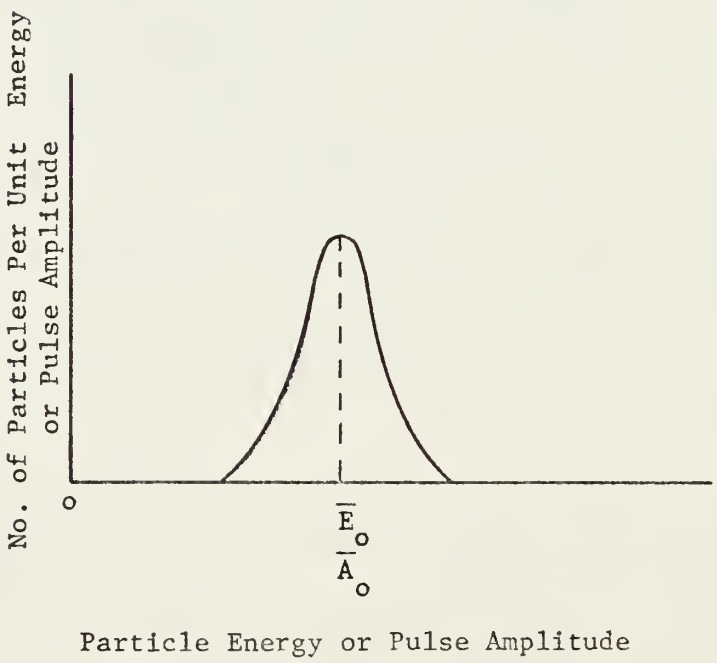

Fig. 2. Actual Alpha Particle Energy Distribution

Many effects contribute to the energy resolution spreading of spectra represented by Fig. (2). These effects, to be discussed later in detail, include alpha source self-absorption, detector "window" energy loss, particle statistics in the detector, and spurious electrical noise generated in the detector and amplifier. It will be assumed that each of the effects contributing to the resolution spreading are distributed according to the normal distribution. This assumption will be examined in detail for each resolution spreading effect. The normal distribution function, p(E), is the probability per unit incremental energy that the contribution for each effect to the measured particle energy will lie between E and E + dE.

$$p(E) = \frac{1}{\sqrt{2\pi}\sigma} \exp\left\{ \frac{-(E-\bar{E})^2}{2\sigma^2} \right\} , \qquad (1)$$

where $\bar{E}$ = mean particle energy,

σ = standard deviation.

$\bar{E}$ corresponds to the most probable energy contribution. The standard deviation is a measure of the distribution width.

The normal distribution is subject to the normalization condition

$$\int_{-\infty}^{\infty} p(E)dE = 1 \qquad (2)$$

since the probability that E will assume some value between negative infinity and infinity is unity.

Each normally distributed spreading effect previously mentioned is characterized by a normal distribution such as Eq. (1). Each has its own characteristic mean energy $\bar{E}$, and standard deviation, σ. It can be shown that the total resolution spreading due to all effects is also character-

ized by a normal distribution with a characteristic $\overline{E}$ and σ (see Appendix B):

$$\sigma_{total} = [\sum_i \sigma_i^2]^{1/2} \quad , \tag{3}$$

where σ_i = standard deviation of the i_{th} resolution spreading distribution.

$$\overline{E}_{total} = \sum_i \overline{E}_i \quad , \tag{4}$$

where $\overline{E}_i$ = mean energy of the i_{th} resolution spreading distribution. The particle energy distribution curve exhibited in Fig. (2) is a normal distribution incorporating the total energy resolution spreading due to the effects previously mentioned. Fig. (3) illustrates the spreading due to several effects. Curve A is the unspread distribution similar to Fig. (1). Curve B represents the resulting distribution of Curve A and a spreading effect such as input resistance noise in the amplifier with $\overline{E} = 0$ and a characteristic σ. Curve C represents distribution B further spread by absorption in the detector window. The mean of the distribution representing detector window energy loss is greater than zero.

The total standard deviation of the particle energy spectrum is related to the full-width of the peak at half of the maximum peak height (FWHM) by the following relationship (see Appendix C):

$$FWHM = 2.35 \ \sigma \quad . \tag{5}$$

Thus the FWHM decreases as the standard deviation decreases.

The standard deviation of the energy resolution spreading distribution due to each previously mentioned noise effect can be predicted in terms of its RMS voltage appearing at the amplifier output. A quantity of charge can be determined which, if released at the amplifier input,

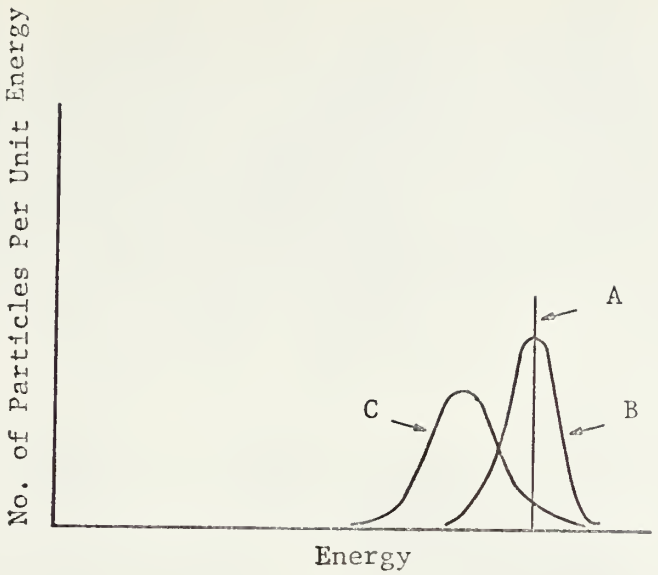

Fig. 3. Effects of Energy Resolution Spreading Upon an Ideal Alpha Particle Energy Distribution

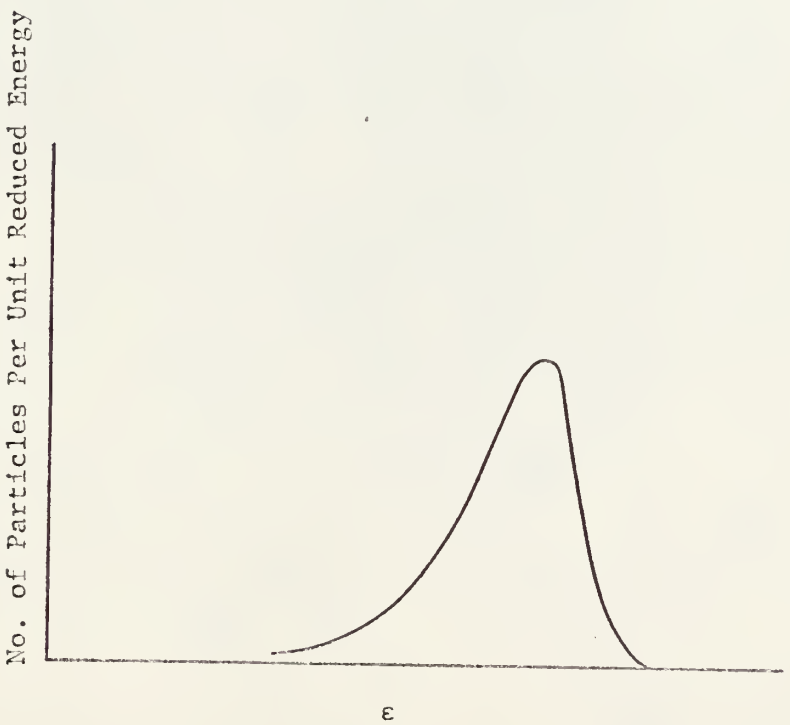

Fig. 4. Energy Distribution of Uncollimated Alpha Particles from a Point Monoenergetic Source After Traversing a Thin Absorber

will produce a pulse at the amplifier output whose maximum amplitude is equal to the RMS value of the noise at the amplifier output. The charge can then be expressed in terms of the energy of an ionizing particle traversing the detector and releasing the given charge. The standard deviation of this equivalent particle energy is the standard deviation (in units of energy) of the energy resolution spreading distribution due to the noise effect of interest. This procedure is described in detail later in this work.

The standard deviations of the energy resolution spreading distributions due to source self-absorption, detector window, and particle statistics are determined later in this work.

2.2 Particle Statistics in the Detector

An important resolution spreading effect is that due to fluctuations in N, the number of ion pairs produced by an alpha particle in the sensitive region of the detector. Alpha particles lose energy in absorbers by excitation and ionization of the absorber atoms. The energy loss occurs by the interaction of the coulomb field of the alpha particles with those of the bound electrons of the absorber. Since the mass of alpha particles is much greater than that of the bound electrons, the alpha particles are not deflected significantly from their original paths. The alpha particles are finally brought to rest by a large number of small energy losses of varying magnitudes. There are variations in both the number of ion pairs produced and in the amount of energy transfer per event (21). If each ionizing event is independent of the others, $p(N)dN$, the probability of producing exactly N ion pairs per incident particle in an incremental dN, varies according to the Poisson distribution (25):

$$p(N)dN = \frac{\bar{N}^N \varepsilon^{-\bar{N}} dN}{N!} \quad , \tag{7}$$

where $\bar{N}$ = mean or average number of ion pairs produced per incident alpha particle.

Eq. (7) applies only for integral values of N.

The standard deviation in N for the Poisson distribution is (21)

$$\sigma_p = \sqrt{\bar{N}} \quad . \tag{8}$$

For the special case of $\bar{N}$ large and $|\bar{N} - N| << \bar{N}$, the Poisson distribution is approximated well by the continuous normal distribution, and the standard deviation of the normal distribution is approximated by (21)

$$\sigma_{\bar{N}} \doteq \sqrt{\bar{N}} \quad . \tag{9}$$

The signal produced by the detector due to an incident alpha particle releasing N ion pairs is an induced charge Q given by the expression

$$Q = Ne \quad , \tag{10}$$

where e = electronic charge (Coulomb).

It is assumed that all of the ion pairs released in the detector contribute to the signal Q. If the ionization process is characterized by completely independent events, the standard deviation in Q is

$$\sigma_{\bar{Q}} = e\sqrt{\bar{N}} \quad . \tag{11}$$

Fano (8) has shown that when ionization along the entire particle range is considered, the ionization events should not be treated as entirely independent. The relationship between the true standard deviation and that predicted by Eq. (9) is (5)

$$\sigma_{F\bar{N}} = \sqrt{F\bar{N}} \quad , \tag{12}$$

where F = Fano factor (usually determined empirically).

The Fano factor for silicon detector material has been determined to be 0.07 (14).

The standard deviation in Q becomes

$$\sigma_{F\bar{Q}} = e\sqrt{F\bar{N}} \quad . \tag{13}$$

$\bar{N}$ can be expressed in terms of the incident alpha particle energy:

$$\bar{N} = \frac{W}{w} \quad , \tag{14}$$

where W = incident alpha particle energy (keV),

w = mean energy required to produce one ion pair in silicon (keV/ion pair).

For 5 MeV alpha particles in silicon, w is 3.61 $\pm$ .01 eV/ion pair (5).

By substituting Eq. (14) into Eq. (13), the standard deviation of charge is obtained:

$$\sigma_{F\bar{Q}} = e\sqrt{FW/w} \quad . \tag{15}$$

This standard deviation in Q must be converted to a standard deviation in units of energy. This is accomplished by multiplying both sides of Eq. (15) by $\frac{w}{e}$ (5), thus

$$\sigma_{\substack{\text{particle} \\ \text{statistics}}} = \sqrt{FwW} \quad . \tag{16}$$

2.3 Incomplete Charge Collection

Incomplete charge collection can affect adversely the resolution of a solid state detector. Ion pairs produced in the detector fail to reach the collecting electrodes by two mechanisms: trapping and recombination. These two mechanisms occur at trapping and recombination centers which are localized detector crystal impurities or imperfections. These centers have associated with them energy levels in the forbidden energy gap of the

detector material. Densely ionizing alpha particles produce large numbers of ion pairs in a very localized area in the detector. Before the detector electric field can separate the positive and negative charges, some of the charges may become immobilized at the recombination centers. An oppositely charged carrier also can be immobilized at the recombination center and recombine with the original immobilized charge carrier. This eliminates the contribution of the ion pair to the detector signal. Since the recombination centers are scattered randomly in the detector, fluctuations develop in the amount of recombined charge. The appearance of fluctuations depends on whether or not ion pairs are released near a recombination center. The fluctuations contribute to the energy resolution spreading by producing variations in the number of ion pairs collected and thus in pulse height at the amplifier output and measured particle energy. Energy resolution deterioration due to recombination has been predicted qualitatively to be important for lithium-ion-drifted detectors (5). Increasing the detector electric field (by increasing the detector bias voltage) will reduce recombination losses by reducing the time available for recombination to take place (2).

After the detector electric field has separated them, the positive and negative charge carriers may become immobilized at trapping centers in the detector. A charge carrier may be trapped for an indefinite length of time. It may be released, to contribute to the detector signal, and subsequently be trapped again. It will contribute a fluctuating component to the detector signal, or, if trapped for a time comparable with the amplifier time constant of differentiation, contribute nothing to the signal. Trapped charge reduces the detector internal electric field and aggravates further the charge collection problem.

2.4 Fluctuations of the Energy Loss for an Alpha Particle Traversing a Thin Absorber

A very important contributor to the energy resolution spreading is the detector "window" effect. This effect appears when an alpha particle traverses a thin absorber before entering the sensitive volume of the detector. Three opportunities exist for the window effect to become important. They are the alpha particle source self-absorption, the detector insensitive region or window, and the energy loss in the medium existing between the source and the detector. The standard deviation of the energy loss distribution due to source self-absorption is generally specified by the manufacturer. The third effect can be made negligible in a properly designed experiment.

When an alpha particle passes through a thin absorber, it undergoes a small energy loss. The mean value of this energy loss is $\overline{\Delta E}$. Considerable fluctuations of the energy loss occur about the mean energy loss. Roux (22) has calculated and experimentally verified the shape of the energy loss distribution in thin absorbers. Roux found that the shape of the energy distribution of alpha particles which had traversed a thin absorber depended on the collimation of the alpha particle beam. For alpha particles entering the absorber material from many different directions prior to detection, the energy distribution of the exiting alpha particles resembled the distribution given in Fig. (4). If the alpha particles are well collimated, the energy distribution may be approximated by a normal distribution. For 5 MeV alpha particles in a silicon absorber, Roux calculated the standard deviation in the energy distribution to be

$$\sigma_s = 0.01\ (1-\varepsilon_1)^{1/2} \quad , \tag{17}$$

where $\varepsilon_1 = \frac{\overline{E}_o'}{E_o}$,

$\overline{E}_o'$ = mean alpha particle energy after traversing the absorber,

E_o = energy of the incident alpha particle.

Since σ_s was derived in terms of the reduced energy, the standard deviation in terms of "true" energy is

$$\sigma_{window} = E_o\ [0.01(1-\varepsilon_1)^{1/2}] \quad . \tag{18}$$

2.5 Amplifier and Detector Equivalent Circuit

In order to analyze the energy resolution spreading due to amplifier and detector noise, it is necessary to assume an equivalent circuit for the combination of the detector, amplifier, and time constant circuitry. Fig. (5) is an equivalent circuit recommended by Gillespie (9) for use with ionization chamber detectors. The grid of the first vacuum tube in the amplifier is considered to be connected to terminal A of Fig. (5). (ΣC) represents the total input capacitance of the amplifier including the capacitance of the detector, detector-to-amplifier coaxial cable, grid to cathode capacitance of the first vacuum tube, and stray capacitance. R represents the total amplifier input shunt resistance due to the parallel combination of the amplifier input resistance and detector resistance. The input terminals of the amplifier are at A and A' of Fig. (5). C_1 and R_1 comprise the time constant circuit of differentiation. This circuit determines the lower-frequency cutoff of the amplifier and is used to improve the time resolution of the system. Time resolution refers to the maximum number of pulses per unit time the amplifier can handle and still maintain

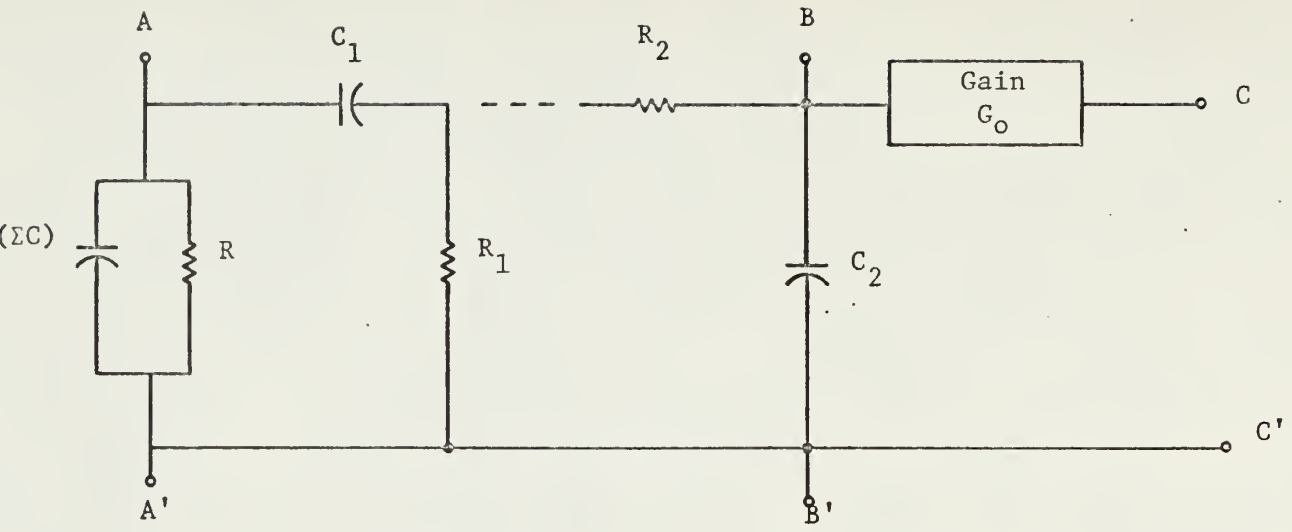

Fig. 5. Equivalent Circuit of the Detector, Amplifier, and Time Constant Circuitry

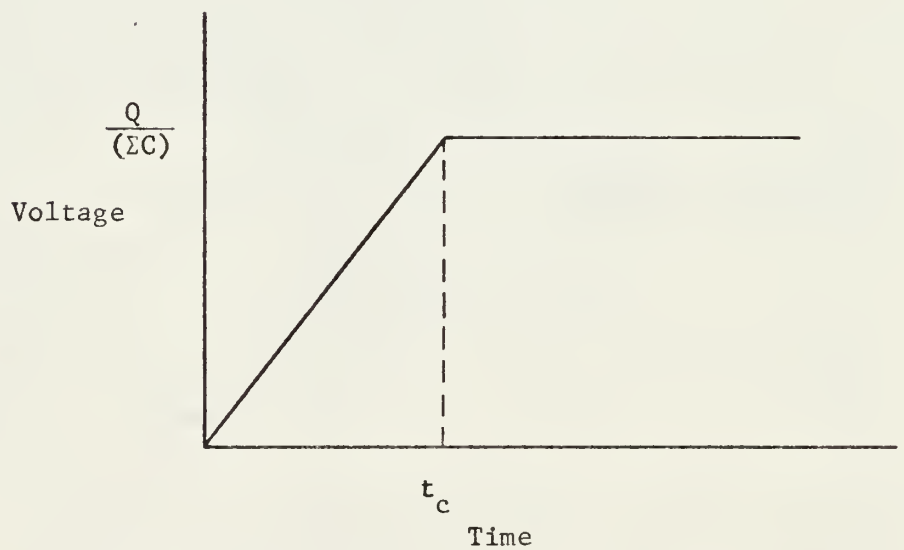

Fig. 6. Theoretical Voltage Pulse from the Detector

linearity between the input and output signal amplitude. Gillespie (9) gives a more detailed description of the use of the differentiating circuit.

C_2 and R_2 comprise the circuit of the time constant of integration. This circuit determines the upper-frequency cutoff of the amplifier and affects the rise and delay time of the pulses. Further information concerning the use of this circuit may be found in Price (21). It may be assumed that the two time constant circuits operate independently of each other since in practice they are located in isolated stages of the amplifier (9). G_o represents the gain of the amplifier. G_o is assumed to remain constant over the whole frequency spectrum. The time constant circuits of $\tau_1(R_1C_1)$ and $\tau_2(R_2C_2)$ determine the frequency response of the amplifier.

Goulding and Hansen (10) have suggested that the equivalent circuit of Fig. (5) may be used for solid-state junction detectors with the qualification that the junction detector has a lower impedance, greater capacitance, and higher leakage current than the ionization chamber. It will be assumed that the equivalent circuit applies to the lithium-drifted silicon detector of interest in this work.

In energy spectrometry, where maximum energy resolution is the prime consideration, the time constant of differentiation, τ_1, is set equal to the time constant of integration, τ_2. This is done to approximate the condition of minimum total amplifier noise (7). This arrangement is not satisfactory if good time resolution is needed.

2.6 Detector Signal

The input pulse signal from the detector to the amplifier at A - A' in Fig. (5) is assumed to rise linearly from zero to a voltage of

$V_o = Q/(\Sigma C)$ in a time t_c as shown in Fig. (6). Q is the total charge collected in the detector per incident particle. V_o is assumed to remain constant for a time which is long compared to τ (9). A more detailed description of the actual input signal has been given by Price (21).

The collection time of the detector, t_c, is defined as the longest possible transit time for the slowest charge carriers to be collected (25). The actual collecting time may vary with alpha particle energy as will the shape of the signal at A - A'. In order to obtain strict linearity with energy, the differentiating time constant should be greater than five times the maximum collecting time (25).

2.7 Energy Resolution Spreading Due to Amplifier and Detector Noise

The important contributions to energy resolution spreading due to noise are the amplifier input resistance noise, tube shot noise, tube flicker or $^1/_f$ noise, tube grid current noise, detector generation-recombination noise, and $^1/_f$ detector noise. Vacuum tube noise contributions are considered from only the first tube in the amplifier. The gain of subsequent tubes in the amplifier renders this noise more important than that generated in later stages. Input resistance noise results from a more basic phenomenon called Johnson or thermal noise. Thermal noise arises from the random motion of the free electrons in a conductor. These charge movements are minute fluctuating currents and give rise to small voltage fluctuations as measured across the ends of the conductor. The mean, or average value of this voltage with respect to time, is zero. However, the mean squared noise voltage in a bandwidth df measured across a conductor of resistance R is not zero and is given by the expression (16)

$$< v_t^2 (f) > df = 4kTRdf \quad , \tag{19}$$

where k = Boltzmann's constant
$(1.37 \times 10^{-23}$ Joules/$^oK)$,

T = conductor temperature (^oK),

R = conductor resistance equal to amplifier input resistance (ohms).

The conductor may be considered to be equivalent to a noise source generating a mean square voltage of magnitude 4kTRdf in a bandwidth (frequency) of df. This voltage may be considered to act in series with a noiseless resistor of resistance R equal to the amplifier input resistance. This treatment follows directly from Thevinin's theorem. The equivalent circuitry is shown in Fig.(7).

The thermal noise has a "white" spectrum. That is, the noise power is uniformly distributed over a large frequency band which includes frequencies of interest in this work (9). The thermal noise generator in Fig. (7) is shunted by the capacitance (ΣC). This capacitance serves to shunt the higher frequency voltage components and acts as a frequency dependent potentiometer. The mean squared thermal noise voltage in a bandwidth df appearing across the capacitance (ΣC) at A - A' is (5)

$$< v_t^2(f) > df = \frac{4kTRdf}{1+[\omega R(\Sigma C)]^2} \quad . \tag{20}$$

Since the angular frequency

$$\omega = 2\pi f, \tag{21}$$

and

$$df = \frac{d\omega}{2\pi} \quad , \tag{22}$$

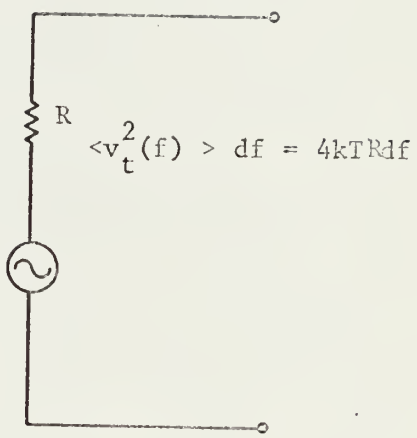

Fig. 7. Equivalent Circuit of the Thermal Noise Generator

Eq. (20) may be expressed as the mean squared thermal noise voltage in an angular frequency bandwidth $d\omega$:

$$< v_t^2(\omega) >d\omega = \frac{4kTRd\omega}{2\pi\{1+[\omega R(\Sigma C)]^2\}} \quad . \tag{23}$$

Since $\omega R(\Sigma C)$ is much greater than 1 (10),

$$<v_t^2(\omega)> d\omega \doteq \frac{2kTd\omega}{\pi\omega^2 R(\Sigma C)^2} \quad . \tag{24}$$

The mean squared spectral densities of the other noise contributors will be discussed before further use is made of Eq. (24).

Tube shot noise is the name applied to the fluctuations about the mean vacuum tube anode current. These fluctuations are caused by the random emission of electrons from the heated cathode. When all of the electrons emitted are collected by the anode, the mean squared anode fluctuation current in a bandwidth df is given by (23)

$$<i_s^2 (f)> df = 2eI_a df \quad , \tag{25}$$

where e = electronic charge (Coulombs),

I_a = mean anode current (Amperes) .

This expression is valid over the frequency range of interest in this work (9). In practical vacuum tube circuits, the tube is operated under space charge limited conditions. That is, the cathode emission may be many times greater than the anode current. The fluctuations in the anode current are similarly reduced and

$$\langle i_s^2(f)\rangle \, df = 2eI_a F_{sc}^2 df, \tag{26}$$

where F_{sc}^2 = space charge smoothing factor ($F_{sc}^2 < 1$).

For low power receiving type vacuum tubes, F_{sc}^2 is approximated by (9)

$$F_{sc}^2 \doteq \frac{0.12\, g_m}{I_a} , \tag{27}$$

where g_m = tube mutual conductance.

Eq. (26) may be expressed in terms of a voltage fluctuation instead of a current fluctuation:

$$\langle v_s^2(f)\rangle \, df = \frac{2eI_a F_{sc}^2 \, df}{g_m^2} . \tag{28}$$

Eq. (27) may be substituted into Eq. (28) with the result

$$\langle v_s^2(f)\rangle \, df \doteq \frac{0.24\, edf}{g_m} . \tag{29}$$

Eq. (29) may be expressed in terms of the incremental angular frequency, $d\omega$:

$$\langle v_s^2(\omega)\rangle \, d\omega \doteq \frac{0.12\, ed\omega}{\pi g_m}. \tag{30}$$

Eq. (30) expresses the mean squared shot noise voltage fluctuation in an angular frequency bandwidth $d\omega$ (9).

Vacuum tube flicker noise, or $1/f$ noise, is a fluctuation of the anode current and has its greatest contribution at low frequencies. It is thought to be caused by the random appearance of impurity centers on the surface of the cathode, affecting electron emission in the impurity areas (9). The mean squared flicker noise voltage fluctuation in a frequency bandwidth df is given approximately by (11)

$$\langle v_f^2(f)\rangle \, df \doteq \frac{10^{-13} df}{f} \quad . \tag{31}$$

Eq. (31) is a valid expression for the vacuum tube $^1/_f$ noise for the frequency range in which this noise component is an important noise contribution (9). This expression may be given in terms of the angular frequency, ω:

$$\langle v_f^2(\omega)\rangle \, d\omega \doteq \frac{10^{-13} d\omega}{\omega} \quad . \tag{32}$$

Eq.'s (30) and (32), which represent the mean squared voltage fluctuations in an angular frequency bandwidth $d\omega$ due to tube shot and tube flicker noise, express the noise generated inside the first vacuum tube. These expressions represent equivalent voltages appearing at A - A'; however, the input resistance and capacitance do not act as a voltage shunt for these noise signals.

Current may flow in the grid circuit of a vacuum tube. This grid current results from grid capture of cathode electrons and capture of positive ions produced by electron collisions with residual gas atoms in the tube envelope. The mean squared grid current fluctuations in a frequency bandwidth df is given by (9)

$$\langle i_g^2(f)\rangle \, df = 2eI_g df \quad . \tag{33}$$

The impedance in the grid circuit consists of the capacity (ΣC) in parallel with the total shunt resistance R. The spectral density of the mean squared shot effect voltage fluctuations due to the grid current is (9)

$$\langle v_g^2 (f)\rangle \, df = 2eI_g \frac{R^2 \, df}{1+\omega^2 R^2 (\Sigma C)^2} \quad . \tag{34}$$

The frequency dependence of Eq. (34) may be replaced by the angular frequency yielding

$$\langle v_g^2(\omega) \rangle \, d\omega = \frac{eI_g}{\pi} \cdot \frac{R^2 \, d\omega}{1+\omega^2 R^2 (\Sigma C)^2} \quad . \tag{35}$$

Since

$$\omega^2 R^2 (\Sigma C)^2 >> 1 \quad , \tag{36}$$

$$\langle v_g^2(\omega) \rangle \, d\omega \doteq \frac{eI_g \, d\omega}{\pi \omega^2 (\Sigma C)^2} \quad . \tag{37}$$

Eq. (37) gives the mean squared voltage fluctuations due to grid current in an angular frequency bandwidth $d\omega$. This mean squared voltage acts at A - A' in Fig. (5).

Noise due to the lithium-drifted silicon detector comes from several sources: thermal noise, leakage current shot noise, generation-recombination noise, and excess, or $^1/_f$, noise. The thermal noise generated has been included in Eq.'s (19) to (24) since the detector resistance was included in the total amplifier input resistance R. Shockley (24) has described a temperature correction for Eq. (19) to compensate for the absorption by electrons in the detector material of energy of the detector electric field. This correction was not used in this work since resistance noise is a very minor contributor to the total detector noise.

The detector leakage current is closely associated with detector noise. The leakage current is believed to come from three sources (17): diffusion current due to the diffusion of minority carriers into the depletion region, the space charge generating current due to the production of charge carriers by thermal generation at recombination centers in the depletion zone, and the surface leakage current. Generally, the diffusion

current is much smaller than the other currents. The surface current may be the major contributor to the reverse current (17).

The detector leakage current can be responsible for three different types of noise: shot noise, generation-recombination noise, and excess, or $^{1}/_{f}$, noise. The mean squared shot noise current fluctuation is derived in the same manner as Eq. (25). Substituting the relationship

$$df = \frac{d\omega}{2\pi} \tag{38}$$

into Eq. (25) yields

$$\langle i^2_{s_{det}}(\omega)\rangle \, d\omega = \frac{e\, I_d \, d\omega}{\pi} , \tag{39}$$

where I_d = mean detector leakage current (Amperes).

The mean squared voltage fluctuation in an angular frequency bandwidth $d\omega$ appearing across the amplifier input capacitance (ΣC) is given by (10)

$$\langle v^2_{s_{det}}(\omega)\rangle \, d\omega \doteq \frac{eI_d \, d\omega}{\pi\omega^2(\Sigma C)^2} . \tag{40}$$

Generation-recombination noise occurs when pairs of carriers in the depletion region of the detector recombine and regenerate at trapping sites in the crystal. The mean free time of the carriers, t_1, is the mean lifetime of a carrier between generation and recombination. If t_1 is less than the detector collection time, t_c, generation and recombination can be an important contributor to fluctuations in the detector leakage current. Prediction of generation-recombination noise is usually treated in a manner similar to that of shot noise. Dearnaley and Northrop (5) have suggested that generation-recombination noise and shot noise of a detector may be mutually exclusive. The shot noise formula gives a maximum contribution

to the noise when no correlation exists between the carriers. Generation-recombination effects act to correlate the carriers and reduce shot noise while increasing generation-recombination noise. In this work, shot noise is assumed to be the dominant effect. The mean carrier lifetime is assumed to be the dominant effect. The mean carrier lifetime is assumed to be less than the collection time. The expression for full shot noise is used since it is assumed to compensate somewhat for generation-recombination effects.

Monteith (18) has found that for moderate detector bias voltages, detector noise was predicted well by the shot noise contribution of the leakage current. As the detector bias was increased, the leakage current appeared to approach a saturation. As bias voltage was further increased, the detector leakage current and noise began to sharply increase. Monteith attributed the increase in noise to $^1/_f$ noise which has a more pronounced effect at lower frequencies. Often $^1/_f$ noise is the most important detector noise contributor (5). It may be reduced by reducing the low frequency response of the amplifier. Van der Ziel (26) treats the problem of $^1/_f$ noise in detail.

Expressions have been derived for the mean squared voltage fluctuation in an angular frequency bandwidth $d\omega$ for each important noise contributor. These noise components have been assumed to appear at terminals A - A' of Fig. (5). It is desired to find the total contribution of these components at C - C'. The attenuation of the time constant of differentiation to sinusoidal voltage components is

$$\left[\frac{1 + \omega^2 \tau^2}{\omega^2 \tau^2} \right]^{1/2} .$$

The attenuation of sinusoidal voltage components by the time constant of integration is (9)

$$[\ 1 + \omega^2\tau^2\ ]^{1/2} \quad .$$

The signal at C - C' of Fig. (5) differs from that at B - B' only by the amplifier gain, G_o. Therefore, a generalized expression for the total mean squared voltage at C - C' due to each noise component appearing at A - A' can be written:

$$\langle v_i^2 \rangle = G_o^2 \int_o^\infty \langle v_i^2(\omega) \rangle \left[\frac{\omega^2\tau^2}{(1+\omega^2\tau^2)} \right] \left[\frac{1}{(1+\omega^2\tau^2)} \right] d\omega \ , \qquad (41)$$

where $\langle v_i^2(\omega) \rangle\ d\omega$ = the mean squared voltage fluctuation in an angular frequency bandwidth $d\omega$ due to the i_{th} noise component appearing at A - A',

τ = amplifier time constant.

With Eq. (41), a list of mean squared voltage contributions can be compiled using the mean squared spectral densities already calculated: Amplifier input resistance thermal noise,

$$\langle v_t^2 \rangle \doteq G_o^2 \int_o^\infty \frac{2kT}{\pi\omega^2 R(\Sigma C)^2} \left[\frac{\omega^2\tau^2}{(1+\omega^2\tau^2)} \right] \left[\frac{1}{(1+\omega^2\tau^2)} \right] d\omega \ , \qquad (42)$$

or

$$\langle v_t^2 \rangle \doteq \frac{G_o^2\ kT\tau}{2R\ (\Sigma C)^2} \ . \qquad (43)$$

Tube shot noise,

$$\langle v_s^2 \rangle \doteq G_o^2 \int_o^\infty \frac{0.12e}{\pi g_m} \left[\frac{\omega^2\tau^2}{(1+\omega^2\tau^2)} \right] \left[\frac{1}{(1+\omega^2\tau^2)} \right] d\omega \ , \qquad (44)$$

or

$$\langle v_s^2 \rangle \doteq \frac{.030\ G_o^2\ e}{g_m \tau} \ . \qquad (45)$$

Tube $^1/_f$ noise,

$$\langle v_f^2 \rangle \doteq G_o^2 \int_o^\infty \frac{10^{-13}}{\omega} \left[\frac{\omega^2\tau^2}{(1+\omega^2\tau^2)} \right] \left[\frac{1}{(1+\omega^2\tau^2)} \right] d\omega \ , \qquad (46)$$

or

$$\langle v_f^2 \rangle \doteq 5 \times 10^{-14}\ G_o^2 \ . \qquad (47)$$

Tube grid current noise,

$$\langle v_g^2 \rangle \doteq G_o^2 \int_o^\infty \frac{eI_g}{\pi\omega^2(\Sigma C)^2} \left[\frac{\omega^2\tau^2}{(1+\omega^2\tau^2)} \right] \left[\frac{1}{(1+\omega^2\tau^2)} \right] d\omega, \qquad (48)$$

or

$$\langle v_g^2 \rangle \doteq \frac{G_o^2\ eI_g \tau}{4(\Sigma C)^2} \ . \qquad (49)$$

Detector shot noise,

$$\langle v_{s_{det}}^2 \rangle \doteq G_o^2 \int_o^\infty \frac{eI_d}{\pi\omega^2(\Sigma C)^2} \left[\frac{\omega^2\tau^2}{(1+\omega^2\tau^2)} \right] \left[\frac{1}{(1+\omega^2\tau^2)} \right] d\omega \ , \qquad (50)$$

or

$$\langle v_{s_{det}}^2 \rangle \doteq \frac{G_o^2\ eI_d \tau}{4(\Sigma C)^2} \ . \qquad (51)$$

It is necessary to determine the amplifier input signal which would produce a maximum output at C - C' in Fig. (5) equal to the total mean squared noise voltage of each energy resolution spreading component. The maximum signal voltage at C - C' is related to the maximum signal at B - B' by the relationship

$$V_{CC'_{max}} = G_o \; V_{BB'_{max}} \quad , \tag{52}$$

where G_o = frequency independent amplifier gain.

The relationship between the maximum pulse voltages at B - B' and A - A' are governed by the time constants of differentiation and integration. The circuit of Fig. (8) is useful in determining the ratio of $V_{BB'_{max}}$ to $V_{AA'_{max}}$. This circuit represents the amplifier time constants of differentiation and integration as shown in Fig. (5). A time dependent voltage source $e_i(t)$ is shown connected to the input of the differentiating circuit. The two time constant circuits act independently and

$$\tau = R_1C_1 = R_2C_2 \quad . \tag{53}$$

The input function to the circuit of Fig. (8), $e_{i_1}(t)$, is assumed to be similar to the function shown in Fig. (6):

$$e_{i_1}(t) = \frac{V_o}{t_c} \cdot t - \frac{V_o}{t_c}(t-t_c)u(t-t_c) \quad , \tag{54}$$

where

$$V_o = \frac{Q}{(\Sigma C)} \; ,$$

t_c = detector collecting time,

$$u(t-t_c) = \begin{cases} 0 \text{ for } t<t_c \\ 1 \text{ for } t \geq t_c \end{cases} \; ,$$

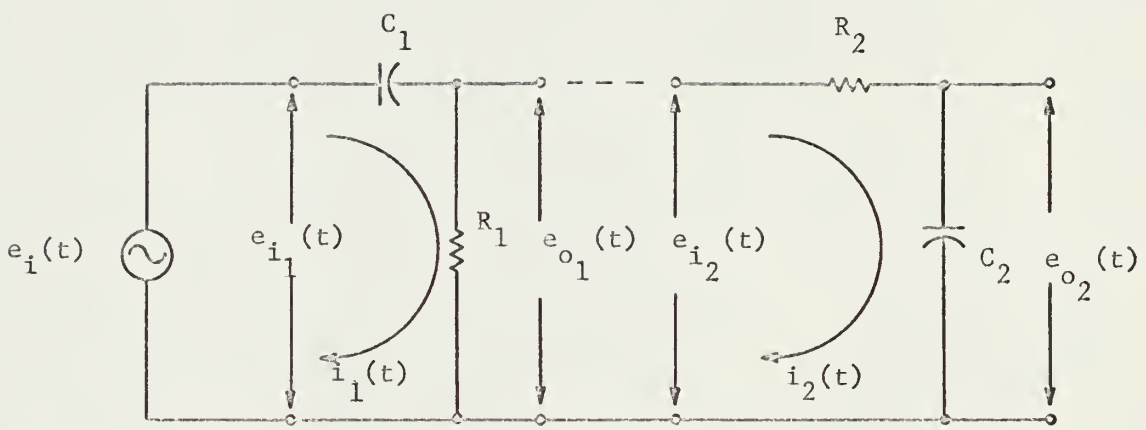

Fig. 8. Circuit Used to Determine $V_{BB'_{max}}/V_{AA'_{max}}$

Kirchoff's voltage law may be used on the differentiation circuit of Fig. (8) yielding

$$e_{i_1}(t) = \frac{1}{C} \int i_1(t)dt + i_1(t)R \quad . \tag{55}$$

Since

$$i_1(t) = \frac{dq_1}{dt} \quad , \tag{56}$$

$$e_{i_1}(t) = \frac{q_1}{C} + R\frac{dq_1}{dt} \tag{57}$$

and

$$e_{o_1}(t) = Ri_1(t) = R\frac{dq_1}{dt} \quad . \tag{58}$$

The Laplace transforms of Eqs. (57) and (58) are

$$E_{i_1}(s) = \frac{Q_1(s)}{C} + RsQ_1(s) \tag{59}$$

and

$$E_{o_1}(s) = RsQ_1(s) \tag{60}$$

which yield

$$\frac{E_{o_1}(s)}{E_{i_1}(s)} = \frac{RsQ_1(s)}{\frac{Q_1(s)}{C} + RsQ_1(s)} \tag{61}$$

or

$$E_{o_1}(s) = E_{i_1}(s) \cdot \frac{s}{(s + 1/\tau)} \quad . \tag{62}$$

$E_{i_1}(s)$, the Laplace transform of $e_{i_1}(t)$, is

$$E_{i_1}(s) = \frac{V_o}{t_c} \cdot \frac{1}{s^2} - \frac{V_o}{t_c} \cdot \frac{e^{-st_c}}{s^2} \quad . \tag{63}$$

Eq. (63) may be substituted into Eq. (62) yielding

$$E_{o_1}(s) = \frac{V_o}{t_c}\left[\frac{1}{s(s+1/\tau)} - \frac{e^{-st_c}}{s(s+1/\tau)}\right] . \qquad (64)$$

The Kirchoff's voltage law equation of the integration circuit is

$$e_{i_2}(t) = i_2(t)R + \frac{1}{C}\int i_2(t)dt . \qquad (65)$$

Since

$$e_{i_2}(t) = e_{o_1}(t) , \qquad (66)$$

and

$$i_2(t) = \frac{dq_2}{dt} ,$$

Eq. (65) becomes

$$e_{o_1}(t) = R\frac{dq_2}{dt} + \frac{q_2}{C} . \qquad (68)$$

The output voltage of the integration circuit is given by

$$e_{o_2}(t) = \frac{1}{C}\int i_2(t)dt , \qquad (69)$$

or

$$e_{o_2}(t) = \frac{q_2}{C} . \qquad (70)$$

The Laplace transforms of Eq.'s (68) and (70) are

$$E_{o_1}(s) = RsQ_2(s) + \frac{Q_2(s)}{C} \qquad (71)$$

and

$$E_{o_2}(s) = \frac{Q_2(s)}{C} . \qquad (72)$$

Therefore,

$$\frac{E_{o_2}(s)}{E_{o_1}(s)} = \frac{\frac{Q_2(s)}{C}}{RsQ_2(s) + \frac{Q_2(s)}{C}} \tag{73}$$

or

$$E_{o_2}(s) = \frac{1/\tau}{(s+1/\tau)} \cdot E_{o_1}(s) \quad . \tag{74}$$

Eq. (64) may be substituted into Eq. (74):

$$E_{o_2}(s) = \frac{V_o}{\tau t_c} \left[\frac{1}{s(s+1/\tau)^2} - \frac{e^{-st_c}}{s(s+1/\tau)^2} \right] \quad . \tag{75}$$

The inverse Laplace transform of Eq. (75) is

$$e_{o_2}(t) = \frac{\tau V_o}{t_c} \left\{ (1-\frac{te^{-t/\tau}}{\tau} - e^{-t/\tau}) - u(t-t_c) \left[1 - \frac{(t-t_c)e^{-t/\tau}e^{t_c/\tau}}{\tau} - e^{-t/\tau}e^{t_c/\tau}\right] \right\}, \tag{76}$$

where $\tau = R\ C$,

$$u(t-t_c) = \begin{cases} 0 \text{ for } t < t_c \\ 1 \text{ for } t \geq t_c \end{cases} .$$

The maximum value of the function $e_{o_2}(t)$ occurs after $t = t_c$ (9). The maximum value is obtained by differentiating Eq. (76) with respect to time, setting the result equal to zero, solving for t_{max}, and substituting t_{max} into Eq. (76):

$$\frac{e_{o_{2_{max}}}}{V_o} = \frac{\tau}{t_c} \left\{ e^{-a} \left[-(a+1) + e^{t_c/\tau} \left(a+1 - \frac{t_c}{\tau}\right)\right] \right\} \tag{77}$$

where $a = \dfrac{t_c}{\tau(1-e^{-t_c/\tau})}$.

If t_c/τ is small, Eq. (77) reduces to

$$\frac{e_{o_{2_{max}}}}{V_o} \doteq .368 \quad . \tag{78}$$

The quantity $e_{o_{2_{max}}}/V_o$ is identical to the ratio of the maximum voltage appearing at B - B' in Fig. (5) to the maximum voltage appearing at A - A' due to the input signal of Fig. (6) at A - A'. Therefore,

$$V_{BB'_{max}} \doteq .368\ V_{AA'_{max}} \quad . \tag{79}$$

Eq. (79) may be substituted into Eq. (52) yielding

$$V_{CC'_{max}} \doteq .368\ G_o\ V_{AA'_{max}} \quad . \tag{80}$$

If the input signal $V_{AA'}$ is a small pulse of charge Q across the amplifier input capacitance (ΣC),

$$V_{CC'_{max}} \doteq \frac{.368\ Q\ G_o}{(\Sigma C)} \quad . \tag{81}$$

Therefore, the mean squared detector charge input at A - A' producing a maximum signal equal to the mean squared voltage of the i_{th} energy resolution spreading component (due to noise) at the amplifier output is

$$< Q_i^2 > \doteq \frac{< v_i^2 > (\Sigma C)^2}{G_o^2\ (.368)^2} \quad , \tag{82}$$

where $< v_i^2 > = i_{th}$ mean squared noise component voltage at C-C'.

The quantity $< Q_i^2 >$ may be expressed in terms of the mean squared energy required to release $< Q_i^2 >$ in a silicon detector:

$$< E_i^2 > \; = \; < Q_i^2 > \frac{w^2}{e^2} \quad , \tag{83}$$

where w = 3.61 eV/electron-hole pair in silicon for 5 MeV alpha particles,

$e = 1.6 \times 10^{-19}$ Coulomb/electron-hole pair.

Eq. (82) may be substituted into Eq. (83) yielding

$$< E_i^2 > \doteq \frac{< v_i^2 > (\Sigma C)^2 \, w^2}{G_o^2 \, e^2 \, (.368)^2} \quad . \tag{84}$$

According to Taylor (25), the mean squared noise (in this case converted to units of energy squared) of the i_{th} resolution spreading noise component is equal to the variance, σ_i^2 , of that component. Therefore,

$$\sigma_i^2 = < E_i^2 > \tag{85}$$

or

$$\sigma_i^2 \doteq \frac{< v_i^2 > (\Sigma C)^2 \, w^2}{G_o^2 \; (.368)^2 \, e^2} \quad . \tag{86}$$

The total variance due to all noise components is given by

$$\sigma^2_{\substack{\text{total} \\ \text{noise}}} \doteq \frac{(\Sigma C)^2 \; w^2}{G_o^2 (.368)^2 \, e^2} \sum_i < v_i^2 > \tag{87}$$

or

$$\text{FWHM}_{\substack{\text{total} \\ \text{noise}}} \doteq 2.35 \left\{ \frac{7.38 (\Sigma C)^2 \, w^2}{G_o^2 \, e^2} \sum_i < v_i^2 > \right\}^{1/2} \quad . \tag{88}$$

2.8 Summary of Theoretical Expressions

Eq. (88) gives the expected FWHM of an alpha particle energy spectrum assuming only amplifier and detector noise. To this expression must be added the variances due to source self-absorption, detector window, and particle statistics:

$$FWHM_{total} \doteq 2.35 \left\{ \frac{7.38(\Sigma C)^2 w^2}{G_o^2 e^2} \sum_i \langle v_i^2 \rangle + \sigma^2_{\substack{\text{source} \\ \text{self-} \\ \text{absorption}}} + \sigma^2_{\substack{\text{detector} \\ \text{window}}} + \sigma^2_{\substack{\text{particle} \\ \text{statistics}}} \right\}^{1/2} \quad (89)$$

or

$$FWHM_{total} \doteq 2.35 \left\{ \frac{7.38(\Sigma C)^2 w^2}{e^2} \left[\frac{kT\tau}{2R(\Sigma C)^2} + \frac{.03e}{g_m \tau} + 5 \times 10^{-14} \right. \right.$$

$$\left. \left. + \frac{e\tau}{4(\Sigma C)^2} (I_g + I_d) \right] + \sigma^2_{\substack{\text{source} \\ \text{self-} \\ \text{absorption}}} + \sigma^2_{\substack{\text{detector} \\ \text{window}}} + FwW \right\}^{1/2} \text{keV} , \quad (90)$$

where

e = 1.59×10^{-19} Coulomb/electron,

F = Fano factor of silicon (.07),

g_m = mutual conductance of the first vacuum tube in the preamplifier (Amperes/Volt),

I_d = detector leakage current (Amperes),

I_g = tube grid current (2×10^{-9}A),

k = 1.37×10^{-23} Joules/^oK,

R = total amplifier input resistance (Ohms),

T = ambient temperature of amplifier and detector (^oK),

w = $3.61 \pm .01 \times 10^{-3}$ keV/ion pair for 5 MeV alpha particles in silicon,

W = energy of alpha particle incident into the sensitive region of the detector (keV),

$\sigma^2_{\substack{\text{detector}\\\text{window}}}$ = [see Appendix (E)],

$\sigma^2_{\substack{\text{source}\\\text{self-absorption}}}$ = [see Appendix (D)],

(ΣC) = total amplifier input capacitance (Farads),

τ = amplifier time constant (seconds).

The expression for the FWHM due to only amplifier noise is obtained from Eq. (90) by deleting the detector shot noise term, the particle statistics term, the source self-absorption term, and the detector window term:

$$\text{FWHM}_{\substack{\text{amplifier}\\\text{noise}}} \doteq 2.35 \left\{ \frac{7.38(\Sigma C)^2 w^2}{e^2} \left[\frac{kT\tau}{2R(\Sigma C)^2} + \frac{.03e}{g_m \tau} + 5\times10^{-14} + \frac{e\tau I_g}{4(\Sigma C)^2} \right] \right\}^{1/2} \text{keV}. \quad (91)$$

The FWHM due to detector leakage current shot noise is obtained from Eq. (90) by deleting all terms except the term involving detector leakage current:

$$\text{FWHM}_{det} \doteq 3.2w \sqrt{I_d \tau / e} \quad \text{keV} . \quad (92)$$

3.0 EXPERIMENTAL DEVELOPMENT

3.1 Theory

The following method of experimentally determining the energy resolution spreading due to amplifier and detector noise is described in Ref. (15). The FWHM contribution to the energy resolution due to noise is determined by measuring the RMS noise voltage output of the amplifier and applying an experimental calibration factor to the results. The first step in this procedure is to calibrate the mercury pulser (pulse generator) with respect to energy. The shape of the pulse from the pulser is adjusted to correspond to previous detector signal pulse shape assumptions.

If a known alpha particle energy spectrum is collected with a PHA, a channel number corresponding to the mean particle energy can be identified. The pulser calibration procedure involves determining the amplitude of the pulser signal necessary for it to be sorted by the PHA into the channel number corresponding to the mean alpha particle energy.

The pulser pulse amplitude is determined by the dial setting of the pulser potentiometer. It will be assumed [see Sect. (3.4)] that a linear relationship exists between the pulser dial setting and the channel number that the pulser pulse is sorted into by the PHA. Therefore by this method, the pulser dial is calibrated directly in units of particle energy.

The RMS voltage measured at the amplifier output (E_{RMS}) is a measure of the standard deviation (σ) of the energy resolution spreading distribution [see Eq. (85)]. This RMS voltage is related to σ by the relationship (15)

$$\sigma = \frac{1.13\ E_{RMS}\ E_{dial}}{E_{ao}} \text{ keV} , \qquad (93)$$

where E_{dial} = dial setting of pulser potentiometer in keV. The quantity E_{ao} is determined by measuring with an oscilloscope the peak voltage of the pulser signal at the amplifier output due to a pulser signal of amplitude E_{dial}. The factor 1.13 is a noise-to-RMS meter correction for average-indicating RMS voltmeters (15).

Thus

$$FWHM_{exp} = \frac{2.35\ (1.13)\ E_{RMS}E_{dial}}{E_{ao}} \text{ keV} \qquad (94)$$

or

$$FWHM_{exp} = \frac{2.67\ E_{RMS}E_{dial}}{E_{ao}} \text{ keV} . \qquad (95)$$

The FWHM due to amplifier noise can be obtained by measuring E_{RMS} with a capacitance equal to the detector and detector-to-preamplifier cable connected to the input of the amplifier. The total FWHM due to both detector and amplifier noise can be obtained by measuring E_{RMS} with the detector connected to the amplifier input.

Since the squared FWHM's are directly proportional to the variances, assuming normally distributed energy resolution spreading distributions, the FWHM due to detector noise only can be found by the relationship

$$(FWHM_{det})^2 + (FWHM_{amp})^2 = (FWHM_{total})^2 \qquad (96)$$

or

$$FWHM_{det} = [(FWHM_{total})^2 - (FWHM_{amp})^2]^{1/2} . \quad (97)$$

The FWHM of an alpha particle energy spectrum is obtained by fitting the PHA data (counts in each channel) to a Gaussian (normal) curve. The FWHM is linearly related to the Gaussian fit parameter σ [see Eq. (5)].

3.2 Apparatus

The equipment used to take data for this work was assembled as shown in the schematic diagram, Fig. (9), and the photograph, Fig. (10). The Americium-241 (^{241}Am) source [see Fig. (11)] supplied 5.477 MeV alpha particles. It was specially prepared to have a very low self-absorption. The manufacturer of the source advised that the typical energy spreading of sources similar to the one used was 8 keV FWHM (6). The lithium-drifted silicon detector used [see Fig. (12)] had a depletion depth of 0.5 mm and an area of 110 mm^2. The distance between the source and detector inside the vacuum chamber was 4.5 cm. The vacuum chamber held the detector and source in place and provided for electrical connection to the detector [see Fig. (13)]. Chamber vacuum was maintained at approximately .02 Torr to eliminate energy degradation of the alpha particles between the source and detector (13). The chamber also assured that moisture would not affect the surface of the detector. A metal shutter was available in the chamber to reduce radiation damage to the detector when the detector was not in use. The detector was mounted on a copper plate, silver soldered to the top of the vacuum chamber, which served as a heat sink. This heat sink was used to cool the detector and stabilize its temperature. The temperature of the heat sink was monitored with a Cu-Constantin thermocouple, potentiometer,

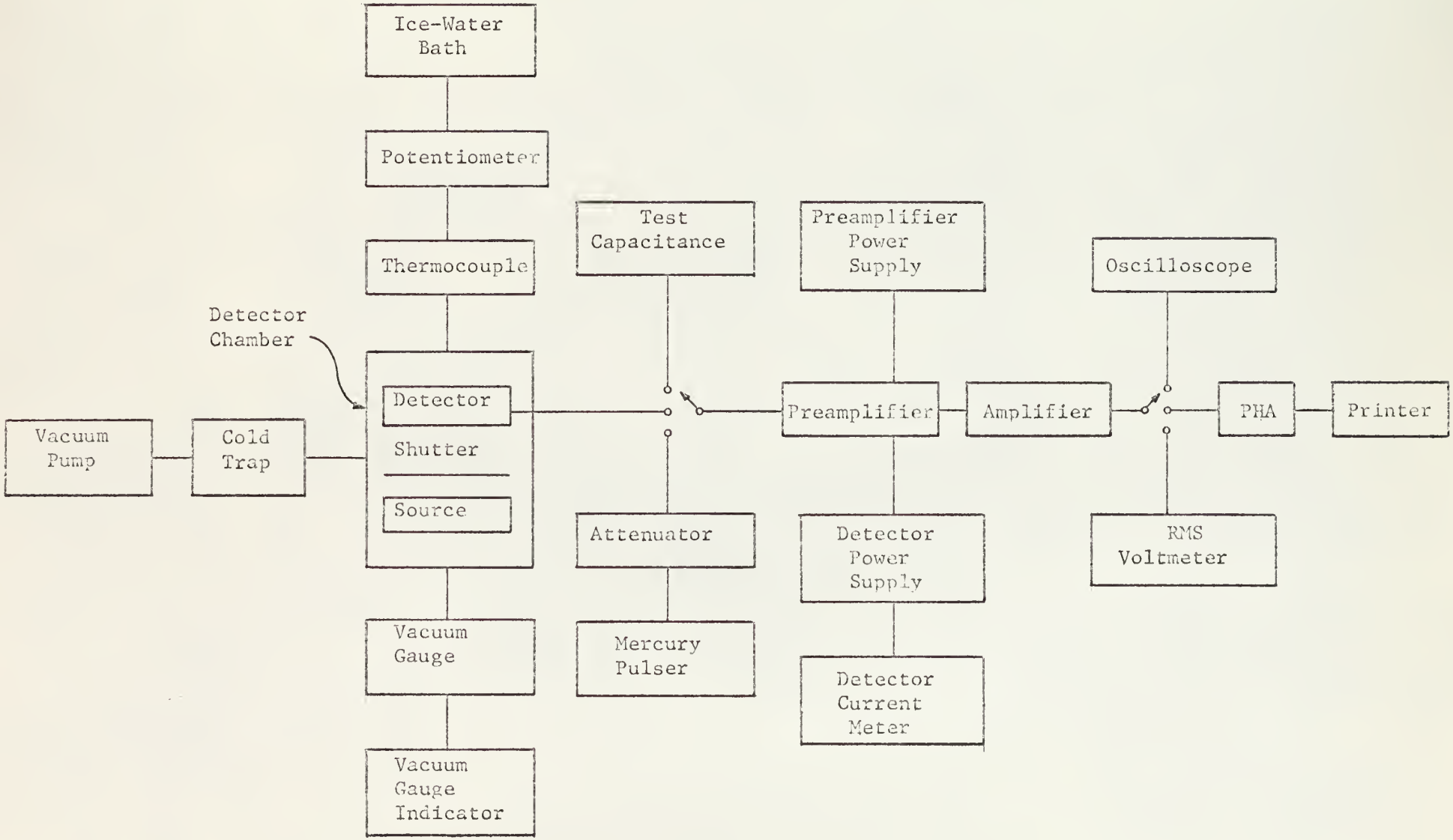

Fig. 9. Block Diagram of the Alpha Particle Spectrometer

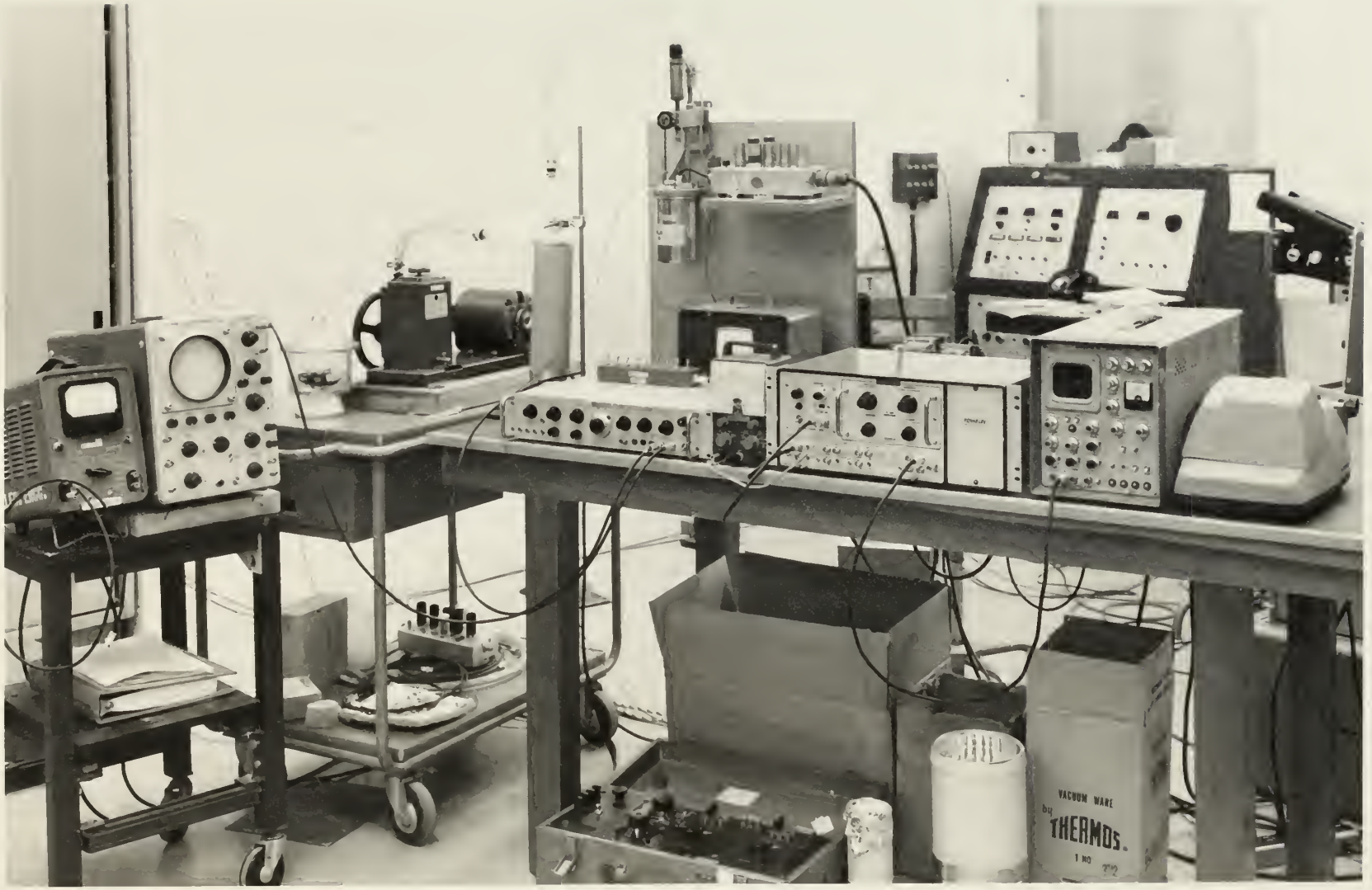

Fig. 10. Equipment Comprising the Alpha Particle Spectrometer

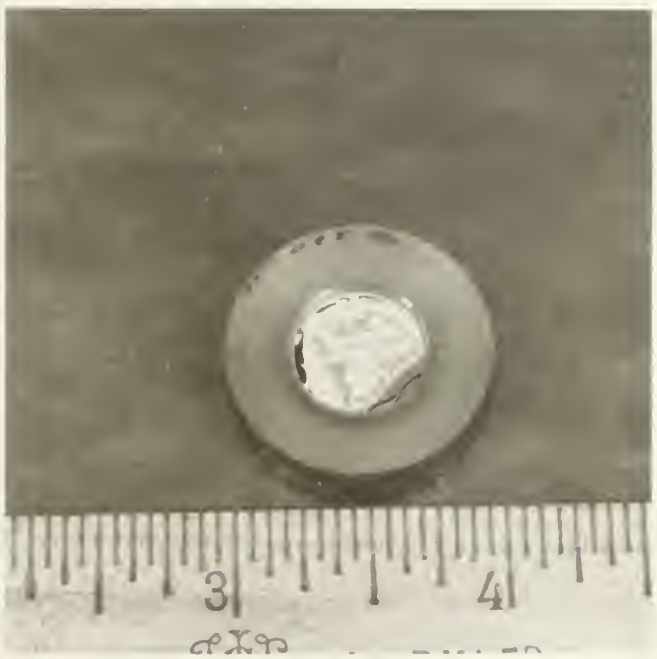

Fig. 11. ^{241}Am Alpha Particle Source

Fig. 12. Lithium-Drifted Silicon Semiconductor Detector

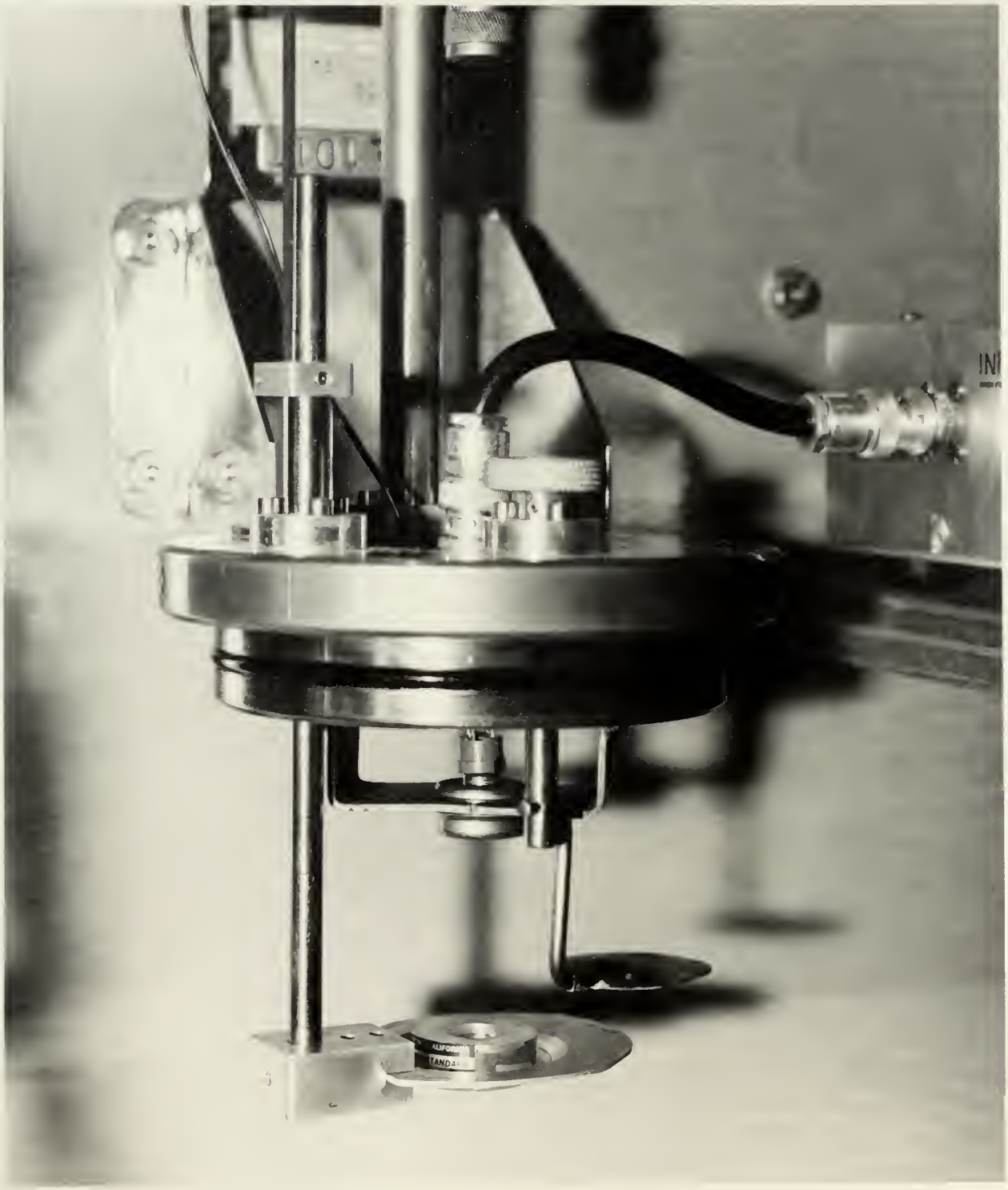

Fig. 13. Uncovered Detector Vacuum Chamber Showing Alpha Particle Source, Shutter, Detector, and Heat Sink

and ice-water bath for the standard electrode. Chamber vacuum was maintained with a rotary mechanical vacuum pump. Chamber vacuum was monitored with a thermocouple vacuum gauge and external readout device.

A charge sensitive preamplifier was used to amplify the detector pulses and match the impedance of the amplifier. A separate power supply was used for the preamplifier. The main amplifier added a further gain to the signal and shaped the signal pulses by variable differentiation and integration networks.

The detector reverse bias supply was built into the amplifier chassis. The supply could deliver a bias voltage of either polarity of from zero to 1000 Volts potential. Detector leakage current was determined by measuring the voltage drop across a 1 megohm standard resistor with a vacuum-tube-voltmeter (VTVM). Thus a voltage drop of 1 Volt across the resistor corresponded to a leakage current of one microampere.

The output of the amplifier was available for analysis by each of three instruments: an oscilloscope, a 100 channel PHA, and an RMS voltmeter. The oscilloscope was used to view the shape of detector and test pulses and to measure their zero-to-peak voltage. The PHA was used to record the number of particles having a pulse height in each of 100 voltage increments. The PHA was used with an external data printer. The RMS voltmeter was used to measure the root-mean-square noise voltages at the amplifier output in various parts of the experimentation.

Test pulses were produced by the pulser. These pulses could be formed with accurately determined amplitudes, rise times, widths, and frequencies. An attenuator was used with the pulser for convenience in selecting pulse amplitudes.

In the final portion of the experimentation, the detector chamber was

immersed in a large Dewar flask filled with ice-water [see Fig. (14)]. A 4096 channel analyzer [see Fig. (15)] in a 1024 channel configuration was used in this part of the experimentation to achieve a smaller energy width per channel and increased energy resolution.

A list of equipment used, with serial numbers, types, and manufacturers' names is given in Table (I).

3.3 Determination of Detector Capacitance

The capacitance of the detector was determined by two independent methods. Technical Measurements Corp. (TMC) (21) gives the following equation to be used for calculating the capacitance of their detectors:

$$C_{det} = \frac{1.1\ k'A \times 10^{-12}}{4\pi W_{dd}} \quad , \tag{98}$$

where k' = relative permittivity of silicon (12),

A = detector area (cm^2),

W_{dd} = detector depletion depth (cm).

This equation expresses the capacitance of a parallel plate capacitor. The detector capacitance was calculated from this equation to be 23 pF (see Appendix D).

A simple experimental technique described by Dearnaley and Northrop (5) was employed to check the results of Eq. (98). The equipment used in the capacitance determination of the detector is shown in Fig. (16). The circuit of Fig. (17) was constructed. The detector is represented by its capacitance C_{det}. The voltage source V_{bias} served as the detector reverse bias supply. C_b blocked the d.c. bias voltage V_{bias} from the oscilloscope. A voltage pulse of amplitude v from a pulser was fed through the known capacitance C_o. This deposited a quantity of charge vC_o on the detector capacitance C_{det}. A pulse of amplitude

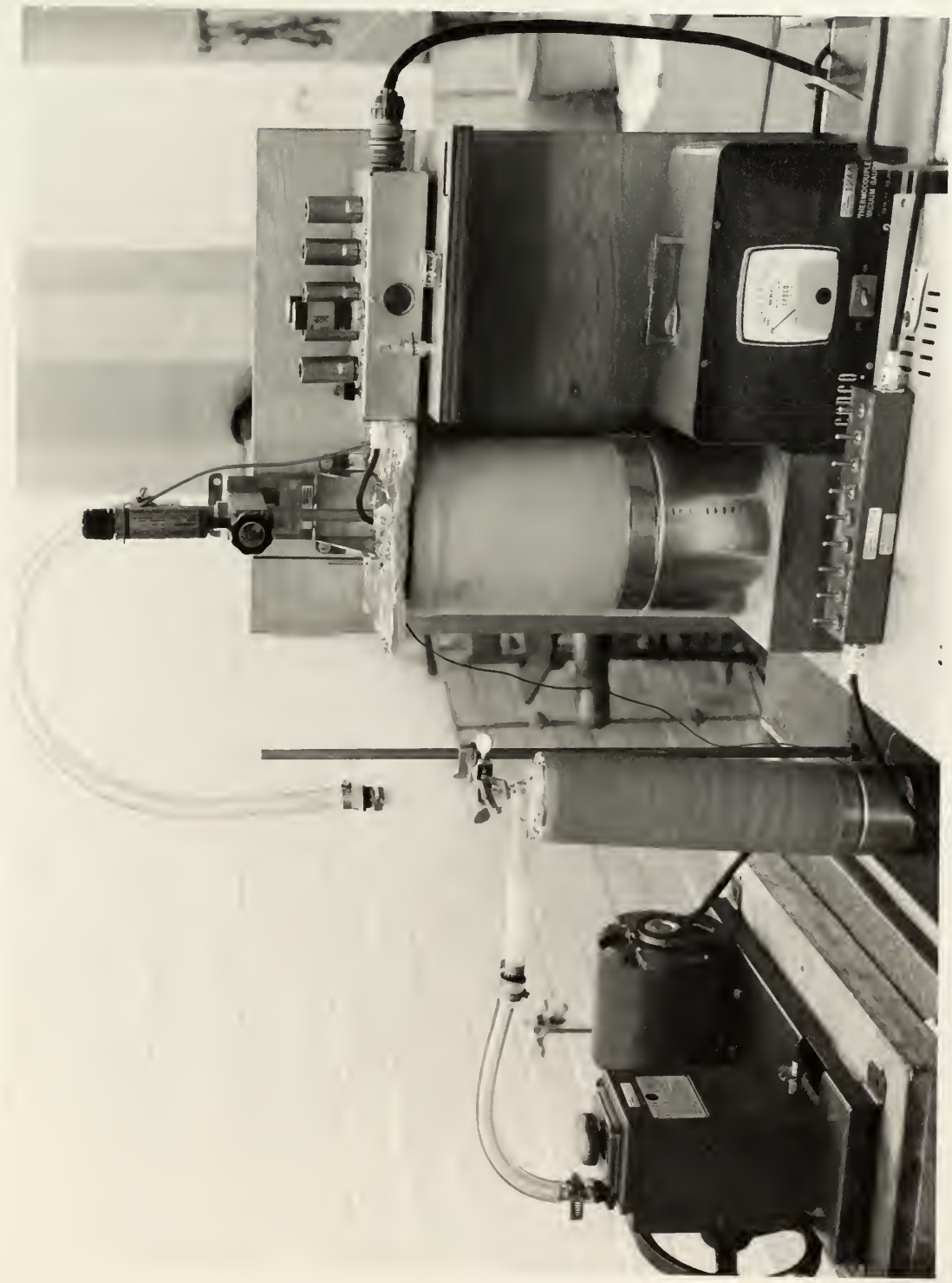

Fig. 14. Detail of Vacuum System and Detector Chamber Cooling Bath

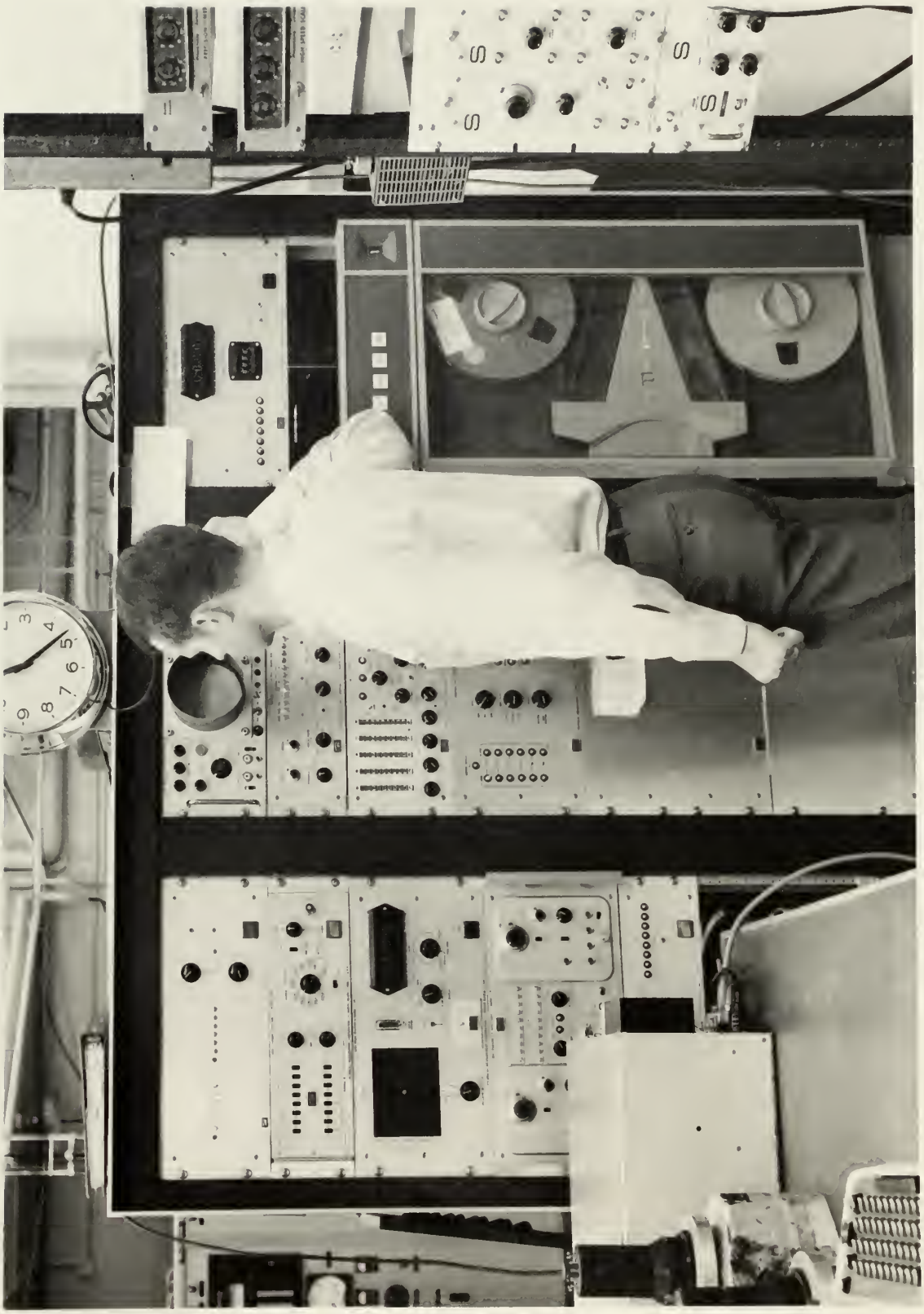

Fig. 15. 4096 Channel Pulse-Height Analyzer

TABLE I EQUIPMENT LIST

Description	Type	Manufacturer	Serial No.
^{241}Am Alpha particle source (0.1 μCurie activity)	RS-61	Nuclear Supplies Inc.	330-4
Vacuum pump	HYVAC	Central Scientific Co.	55541
Cold trap	-----	Central Scientific Co.	-----
Detector chamber	804	Oak Ridge Technical Enterprises Corp.	72
Thermocouple vacuum gauge	D1	NRC Equipment Corp.	-----
Vacuum gauge indicator	94178	Central Scientific Co.	-----
Preamplifier	100A	Tennelec Instrument Co.	163
Preamplifier power supply	900	Tennelec Instrument Co.	233
Amplifier	TC-200	Tennelec Instrument Co.	812
Pulse-height analyzer (100 channels)	102	Technical Measurements Corp.	13007
Pulse-height analyzer (4096 multi-parameter system, KSU Physics Dept.)	-----	Technical Measurements Corp.	-----
Serial printer	001G11	Monroe	M-117264-D
RMS VTVM (KSU EE Dept.)	400D	Hewlett-Packard	5124
VTVM	V-7A	Heath	-----
Pulse generator	GL-3	Berkeley Nucleonics Corp.	600
Attenuator	1/452C	Kay Electric Co.	3355

Oscilloscope	515A	Tektronix Inc.	009358
Detector	W80-1/2	Technical Measurements Corp.	SN1533
Thermocouple potentiometer (KSU ME Dept.)	-----	Leeds and Northrup Co.	1042511
Thermocouple wire	Cu-Constantin	----------	------
Dewar flask	-----	Central Scientific Co.	------
Dewar flask	-----	Central Scientific Co.	------
Digital Voltmeter	TDVM5001	Electronic Associates Inc.	47
Detector Power Supply	TC907B	Tennelec Instrument Co.	------
DC calibration power supply	6434B	Hewlett-Packard	208
Low frequency oscillator	400-C(R)	Krohn-Hite	------

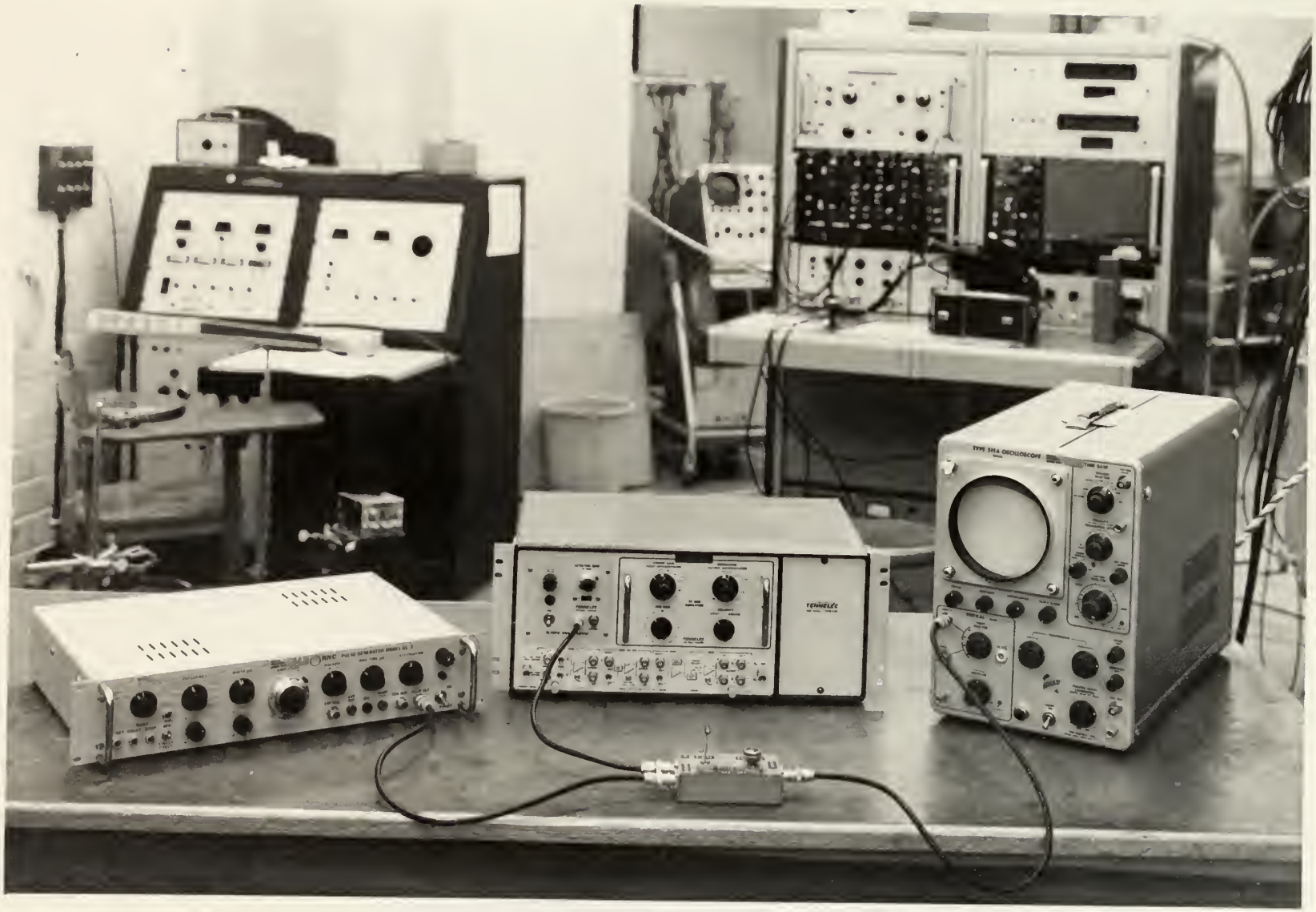

Fig. 16. Equipment Used to Measure Detector Capacitance

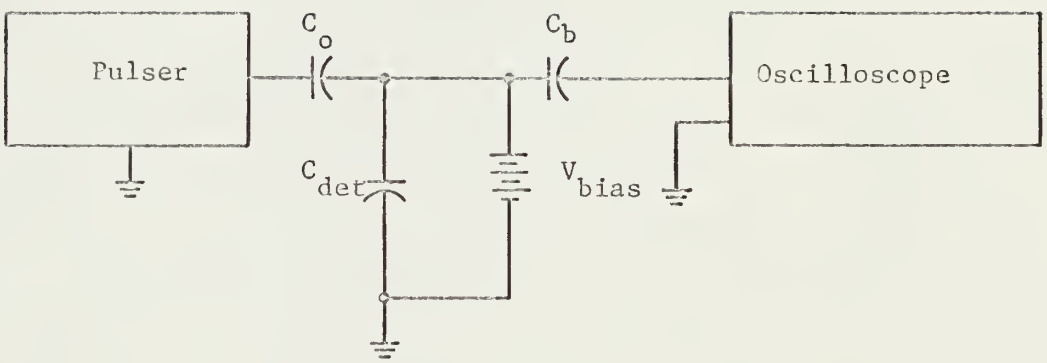

Fig. 17. Circuit Used to Measure Detector Capacitance

$$v_{out} = v \frac{C_o}{C_{det}} \qquad (99)$$

was measured by the oscilloscope. The circuit was calibrated by substituting known values of capacitance for the detector and measuring the resulting output pulse amplitude. The results of this calibration are shown in Fig. (18). These results were fitted by a linear least-squares analysis and found to be represented by the equation

$$C \doteq 261. - 57.3\ v_{out}(\text{pF.}) . \qquad (100)$$

The detector was then substituted for the calibration capacitance. Output voltages (v_{out}) were measured as the detector bias was varied. v_{out} was found to remain relatively constant for the bias range of 20 to 100 Volts. This v_{out} was then substituted into Eq. (100) to yield a value of detector capacitance of 24 pF. This value is in good agreement with that predicted by Eq. (98).

3.4 Instrument Checkout and Calibration

Instruments requiring calibration were the HP (Hewlett-Packard) RMS voltmeter, Heath VTVM, and the Tektronix oscilloscope. The calibration of the RMS voltmeter was checked by a procedure recommended by the manufacturer. In this procedure, the RMS voltmeter was used to measure the root-mean-square voltage of a standard 400 cps sinusoidal voltage of 0.3 Volts RMS. No accurately calibrated sinusoidal voltage source was available. Therefore a standard sine wave generator was accurately calibrated with respect to sine wave amplitude by the following procedure. The pulse generator used in the data collection part of this work had a pulse amplitude precision of $\pm$ .5 per cent over the range from 0.1 Volts to 10.1 Volts. The pulse generator was adjusted to deliver a pulse amplitude of .424 Volts into an oscilloscope. This voltage amplitude corresponded to the maximum amplitude

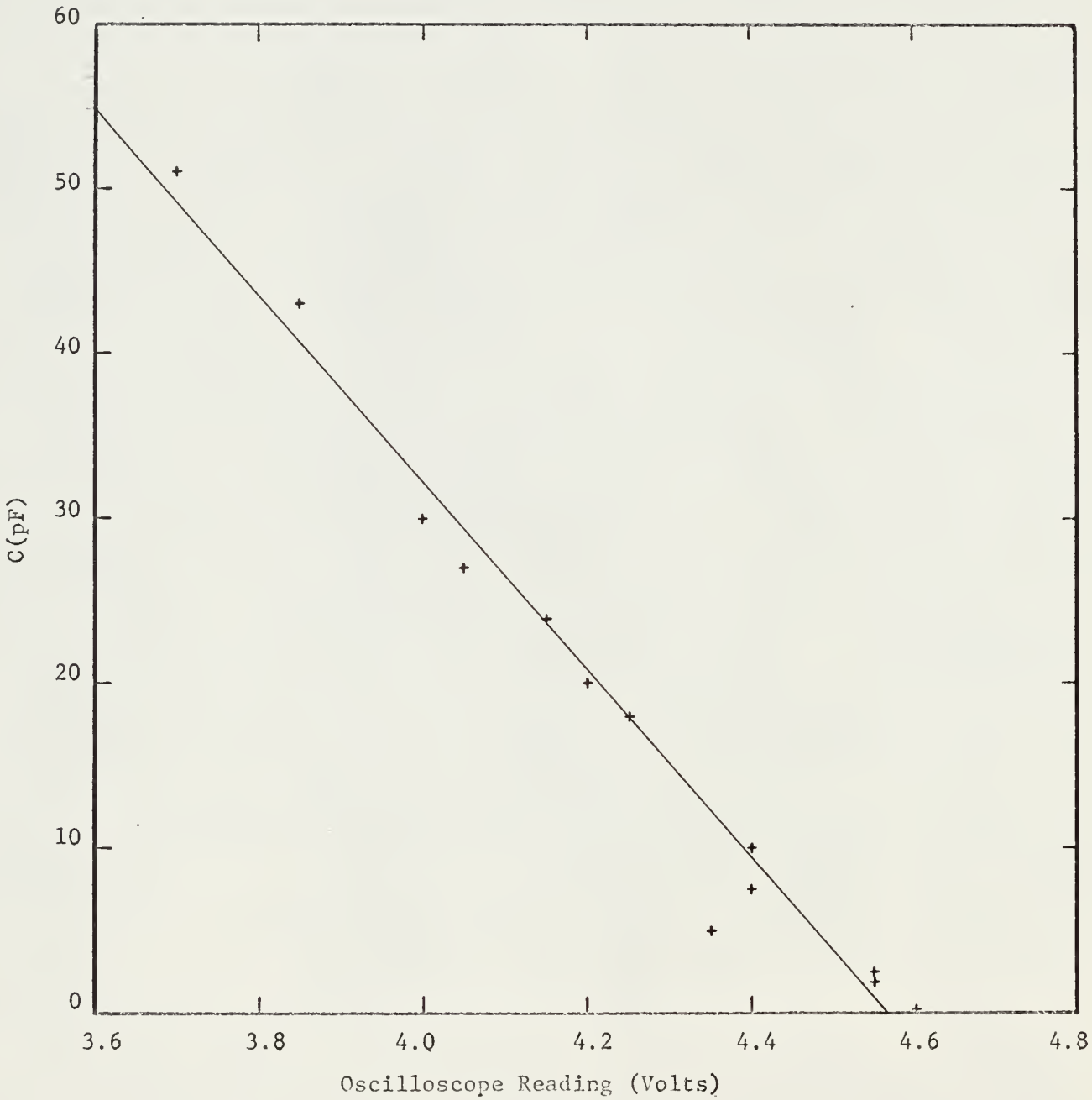

Fig. 18. Detector Capacitance Calibration Curve

of a sinusoidal voltage whose RMS value was 0.3 Volts. The sinusoidal voltage generator output was adjusted until its maximum amplitude, as observed in the oscilloscope, was equal to that of the pulse generator signal. It was estimated that the heights of the two signals were compared by the oscilloscope trace to a least 1 per cent precision. The RMS voltmeter was then adjusted until its meter displayed 0.3 Volts RMS when connected to the calibrated sine wave generator.

The Heath VTVM was calibrated by measuring a voltage of approximately 1.5 Volts d.c. supplied by the Hewlett-Packard power supply. The power supply voltage was accurately known by measurement with the EAI (Electronic Associates Inc.) digital voltmeter whose precision was $\pm$ .01 per cent. After calibration, the precision of the Heath VTVM was at least $\pm$ 3 per cent of full scale (1).

The calibration of the oscilloscope was facilitated by a build-in square wave generator. The generator supplied square wave signals of various amplitudes. The wave forms could be viewed on the oscilloscope and the oscilloscope gain adjusted to give a calibrated trace deflection for the known input signal amplitude. The oscilloscope, adjusted in this manner, was capable of $\pm$ 3 per cent precision (12).

The preamplifier was checked for low noise by measuring the output noise voltage with the HP RMS voltmeter. The amplifier input was left unconnected during this measurement. A low-noise first input vacuum tube was selected by tube substitution.

A brief check of the PHA integral linearity was performed as follows: The mercury pulser was used to generate pulses of four different heights within the pulse height range of the PHA. The channel numbers into which

the pulses were sorted by the PHA were plotted vs. the PHA potentiometer setting. Height of the generated pulses was assumed to be linear with pulser potentiometer setting. A linear relationship was found between pulse height and channel number [see Fig. (19)].

3.5 Procedure

The experimental procedure used in the accumulation of the data consisted of the following sequential series of steps:

(1) The detector temperature was measured by monitoring the output voltage of the thermocouple attached to the detector chamber.

(2) The alpha particle source (which had been covered to prevent radiation damage to the detector) was uncovered.

(3) The VTVM monitoring the detector leakage current was calibrated to read zero Volts with no leakage current passing through the one megohm standard resistance.

(4) The detector bias voltage was adjusted to the desired magnitude.

(5) The detector leakage current was measured by the voltage drop appearing across the one megohm standard resistor.

(6) An alpha particle energy spectrum was accumulated in the PHA during a time of 10 minutes. The PHA channel number was noted in which the highest number of pulses was stored.

(7) The alpha source was covered by the movable shutter inside the detector chamber.

(8) The RMS voltage appearing at the amplifier output was measured with the RMS voltmeter.

(9) The detector bias was removed slowly. A capacitance simulating the detector and cable capacitance (ΣC) was connected to the

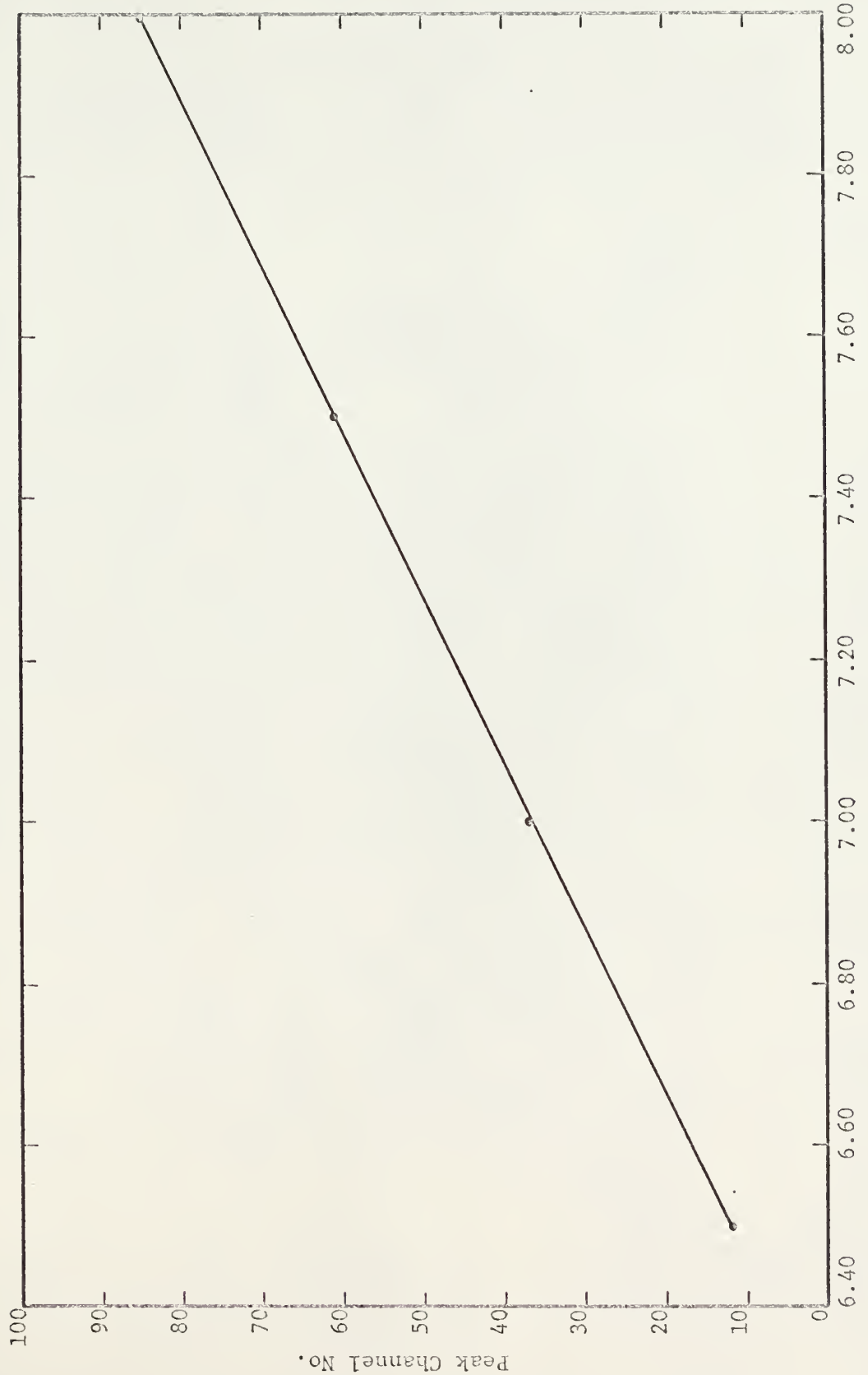

Fig. 19. Check of Pulse-Height Analyzer Integral Linearity

amplifier input.

(10) The RMS voltage appearing at the amplifier output was measured.

(11) The pulser signal amplitude was adjusted to correspond with the mean alpha particle pulse height as measured by the PHA.

(12) The pulser potentiometer was adjusted to the pulse magnitude which produced a pulse collected in channel number 90 of the PHA.

(13) The pulser potentiometer was adjusted to the pulse magnitude which produced a pulse collected in channel number 10 of the PHA.

(14) The oscilloscope was calibrated.

(15) The pulser potentiometer was adjusted to produce a pulse corresponding in magnitude to the mean alpha particle pulse height (E_{dial}). The magnitude of the pulse (E_{ao}) was measured at the amplifier output with the oscilloscope.

(16) The detector was reconnected to the preamplifier.

This procedure was followed three times for each set of equipment conditions. The detector bias voltage was varied from 10 to 100 Volts in 10 Volt increments for an amplifier time constant of 0.8 μsec. For three values of detector bias voltage (40, 70, and 100 Volts), the amplifier time constant (τ) was varied by a factor of 2 for each increment from 0.05 μsec. to 3.2 μsec. All of these measurements were taken at room temperature ($298^{\circ}K$).

The last data were taken by making three procedure sequences with the following equipment conditions: Detector bias = 100 Volts, τ = 0.4 μsec., and detector temperature approximately $10^{\circ}C$. An ice-water bath was used to cool the detector chamber. Lower detector temperatures were attempted using

a dry ice and ethanol bath and a liquid nitrogen detector chamber bath. The resulting lower temperatures tended to embrittle the sealing gasket on the detector chamber and vacuum was quickly lost.

Noise data were converted to the FWHM's of energy resolution spreading distributions according to Eq.'s (95) and (97). FWHM's of the alpha particle energy spectra were obtained from a computer program which fit Gaussian curves to the PHA data and gave values of the FWHM of each fit (3).

4.0 RESULTS AND DISCUSSION

4.1 Amplifier Noise Contribution to Energy Resolution Spreading

The amplifier noise contribution to the energy resolution spreading, as predicted by Eq. (91), was plotted in Fig. (20) as a function of τ, the amplifier time constant. Experimental results are included for comparison. The shape of the theoretical curve follows the data trend. In all cases, experimental noise FWHM was greater than the theoretically predicted values. However, agreement is good for large values of τ. Eq. (91) predicts that the terms for input resistance noise and grid current noise are important for large values of τ. However, tube shot noise is important for small values of τ. Also, it can be noted from Eq. (91) that the terms for input resistance and grid current noise are independent of the quantity (ΣC). The shot noise term is proportional to the square of (ΣC). The value of (ΣC) is probably the least well known of the quantities in Eq. (91). Its total value was not measured, only the values of contributors to (ΣC) such as detector capacitance, were measured. Capacitance contributions from the detector housing, cable connectors, etc. were estimated. Thus, error due to the uncertainty of the value of (ΣC) would appear only for low values of τ.

At large values of τ, both input resistance noise and tube grid current contributions to the total FWHM become much greater than that of $1/_f$ noise. Therefore, error due to the former two sources would be suspected. The determination of the amplifier input resistance was based on the approximation that this resistance was adequately represented by the parallel combination of the detector resistance and the detector load resistance. The value of I_g

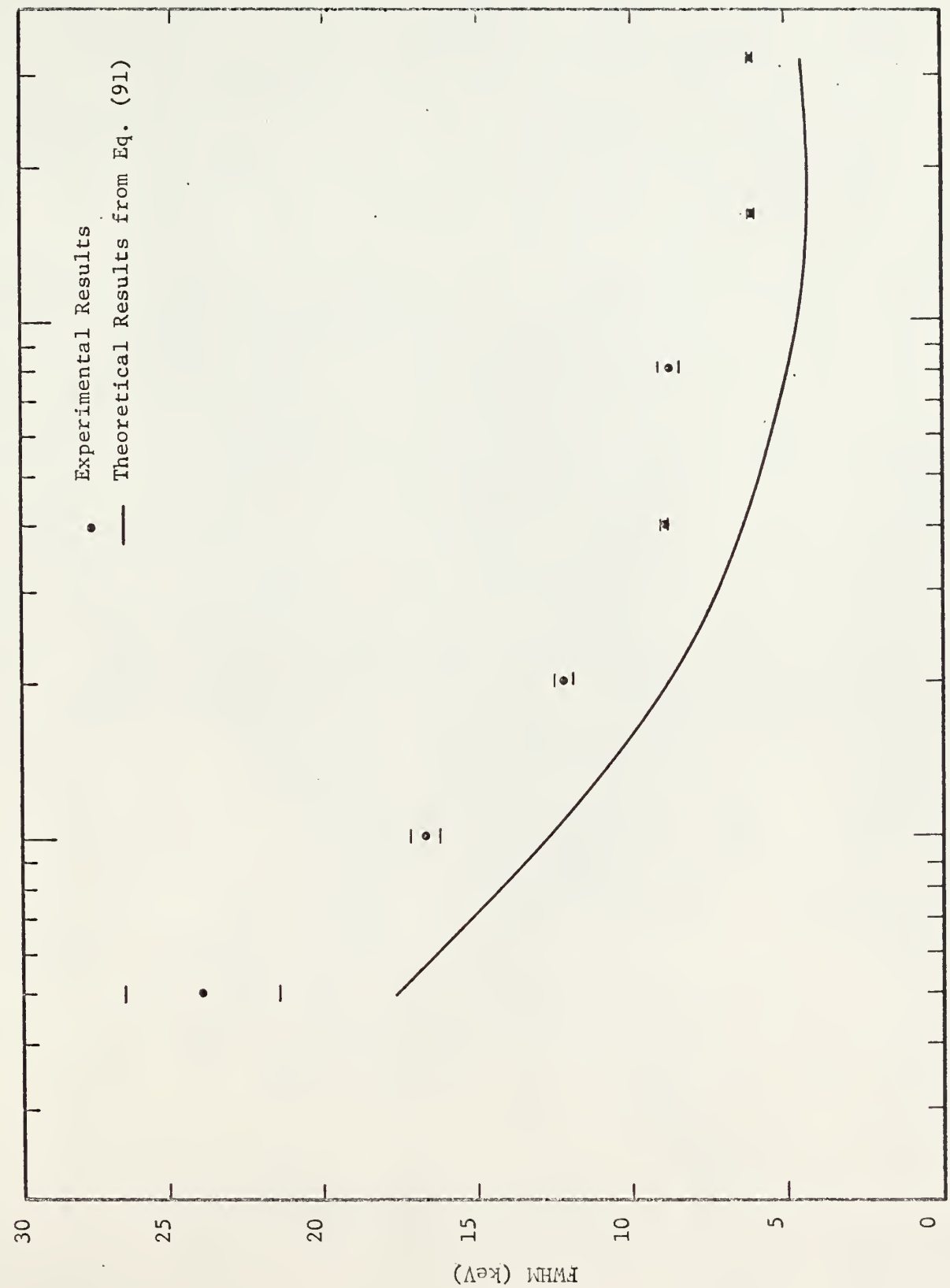

Fig. 20. Energy Resolution Spreading Due to Amplifier Noise as a Function of Amplifier Time Constant

was also an approximation (10).

The choice of an optimum amplifier time constant based only on amplifier noise can be made from the theoretical expression by differentiating Eq. (91) with respect to τ, setting the result equal to zero, and solving for $\tau_{optimum}$. The optimum value of τ is 1.9 μsec. The experimental results support this choice. The value of the FWHM at $\tau_{optimum}$ is obtained by substituting $\tau_{optimum}$ into Eq. (91) and solving for the FWHM. The optimum FWHM at $\tau_{optimum}$ is 4.3 keV. This compares favorably with the lowest experimental FWHM of 6.06 $\pm$ .10 keV which occurs at τ = 1.6 μsec.

4.2 Detector Noise Contribution to Energy Resolution Spreading

The theoretical expression for detector energy resolution spreading (FWHM) due to shot effect noise (Eq. 92) is a function of the experimental variables I_d, the detector leakage current, and τ, the amplifier time constant. Therefore, a great deal of attention was given to the experimental determination of the detector leakage current. Leakage data were taken immediately upon placing the detector into the detector chamber under vacuum and also during the course of the experimentation. These data are exhibited in Fig. (21). Leakage current data taken by the manufacturer are also included in this figure. It was noticed that the leakage current stabilized after a few days and remained constant over the data collection period (approximately one month). Equilibrium values of leakage current were much greater than the manufacturer's results and those results obtained immediately after removing the detector from the storage dessicator. It is possible that the detector surface may have become contaminated with vacuum pump oil which reduced its resistivity. It is known that this type of detector is very sensitive to surface condition and treatment (20).

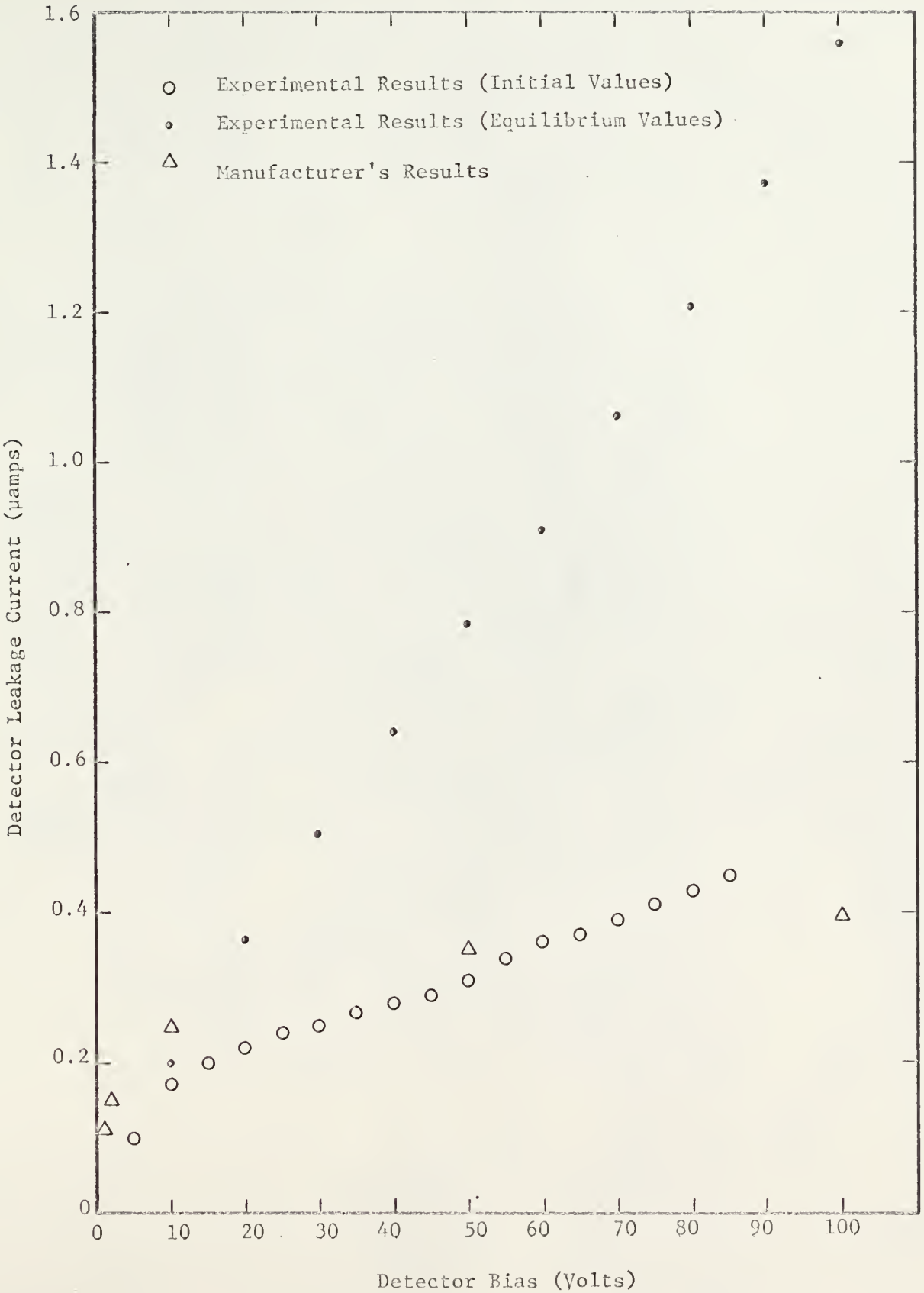

Fig. 21, Detector Leakage Current Variation with Detector Bias Voltage

Eq. (92) does not account for thermal noise produced in the detector since detector thermal noise is a negligibly small contributor to the total detector noise. Eq. (92) predicts energy resolution spreading due to detector leakage current shot noise. It has been assumed that effects of generation-recombination noise were adequately accounted for in Eq. (92). The variation of the energy resolution spreading (FWHM) due to detector noise as a function of detector leakage current is given in Fig. (22). Both experimental and theoretical results are given. The theoretical expression generally overestimates the detector noise contribution to the FWHM. This overestimation of the FWHM is contrary to the results of Monteith (18) who found that the detector leakage current shot effect noise was generally an underestimate of the detector noise contribution to the FWHM. A possible explanation of this disagreement follows: Masuda and Takeda (17) state that the detector leakage current consists of two component currents, one of which is correlated with detector noise, and one component current which is not correlated with the noise. The current not associated with the noise was attributed to surface leakage current and comprised a large fraction of the total leakage current (17). The theoretical detector noise FWHM as predicted by Eq. (92) was based on the detector leakage current data exhibited in Fig. (21). These leakage current values are unusually large and have been assumed to contain much surface leakage due to effects previously mentioned. Therefore, Eq. (92) could be expected to yield unusually large theoretical values of FWHM.

The higher values of experimental detector noise FWHM at low leakage currents can be attributed to increased detector capacitance at the low detector bias voltages (less than 20 Volts) associated with the low leakage currents. The increased detector capacitance resulted in increased amplifier

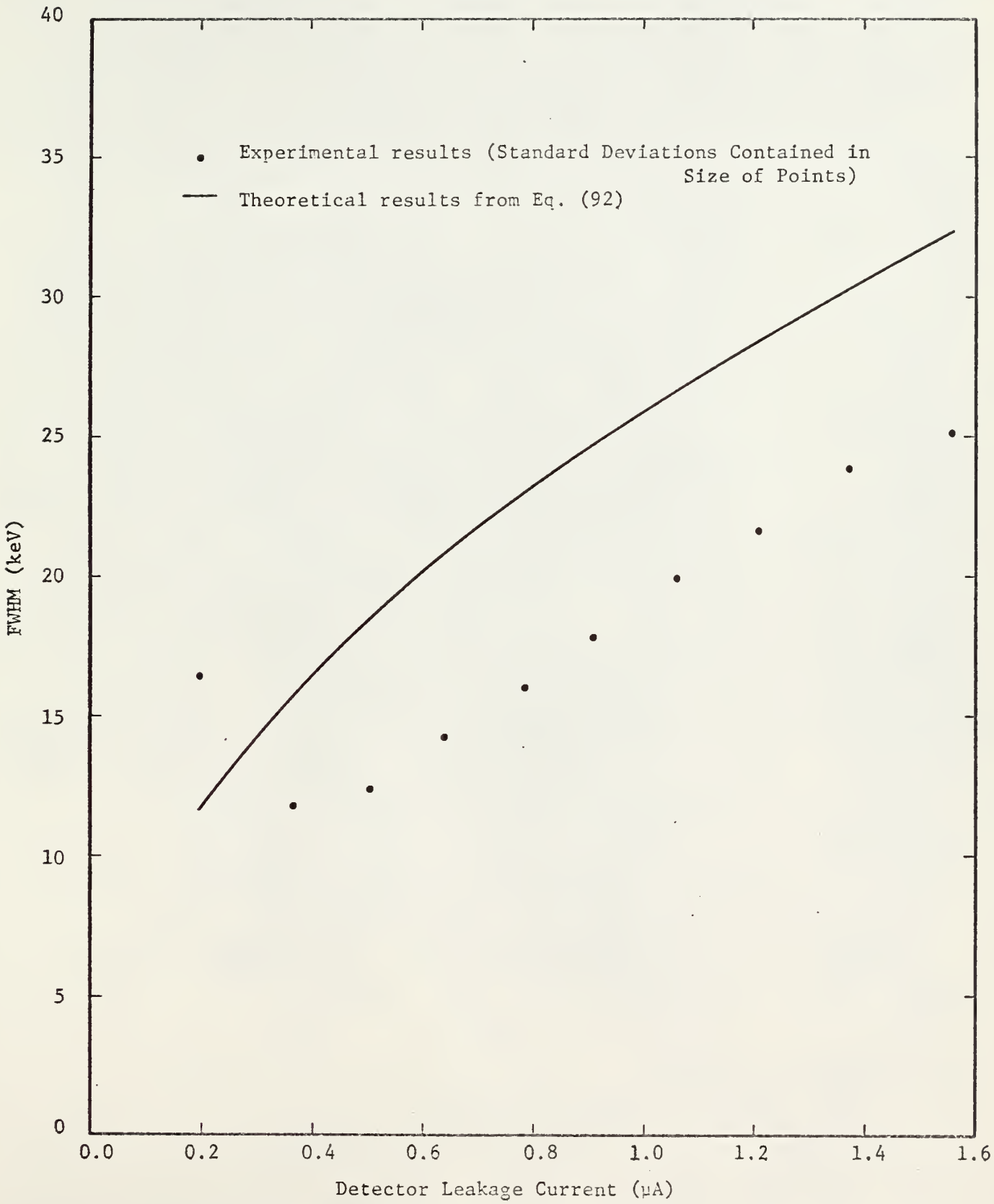

Fig. 22. Variation of Energy Resolution Spreading Due to Detector Noise with Detector Leakage Current (τ = 0.8 μsec)

shot noise [see Eq. (91)]. According to Eq. (97) the detector noise contribution to the FWHM is equal to the square root of the difference of the amplifier plus detector noise FWHM squared and the amplifier noise FWHM squared. The increased amplifier shot noise contributed to the amplifier plus detector noise FWHM in Eq. (97). However, the amplifier noise FWHM was measured while the original constant value of capacitance was connected to the amplifier input. Therefore, the detector noise FWHM showed an increase in value.

The effects of varying the amplifier time constant on the detector noise FWHM are shown in Fig. (23) for V_{bias} = 40 Volts, Fig. (24) for V_{bias} = 70 Volts, and Fig. (25) for V_{bias} = 100 Volts. Both theoretical and experimental results are given. General agreement exists between theoretical and experimental results, especially at higher bias voltages. Eq. (92) underestimates the FWHM at low values of τ and overestimates the FWHM at high values of τ. The overestimation can be explained by the arguments presented earlier about the excess leakage current effect on the shot noise prediction which is proportional to τ. The underestimation may be explained by the following arguments: At low values of τ, the shot noise prediction of the FWHM will be low [see Eq. (92)]. It has been stated earlier that $1/f$ noise would be expected to remain constant when the effect of the pulse-shaping circuits is taken into account. The experimental values of FWHM as a function of τ for all three bias voltages reach a minimum value of about 9 keV. This value may be assigned to the $1/f$ noise. This author can give no explanation for the slight increase in experimental FWHM at low bias voltages and low values of τ. This effect does not appear at V_{bias} = 100 Volts.

Although fairly good agreement exists between experimental values of

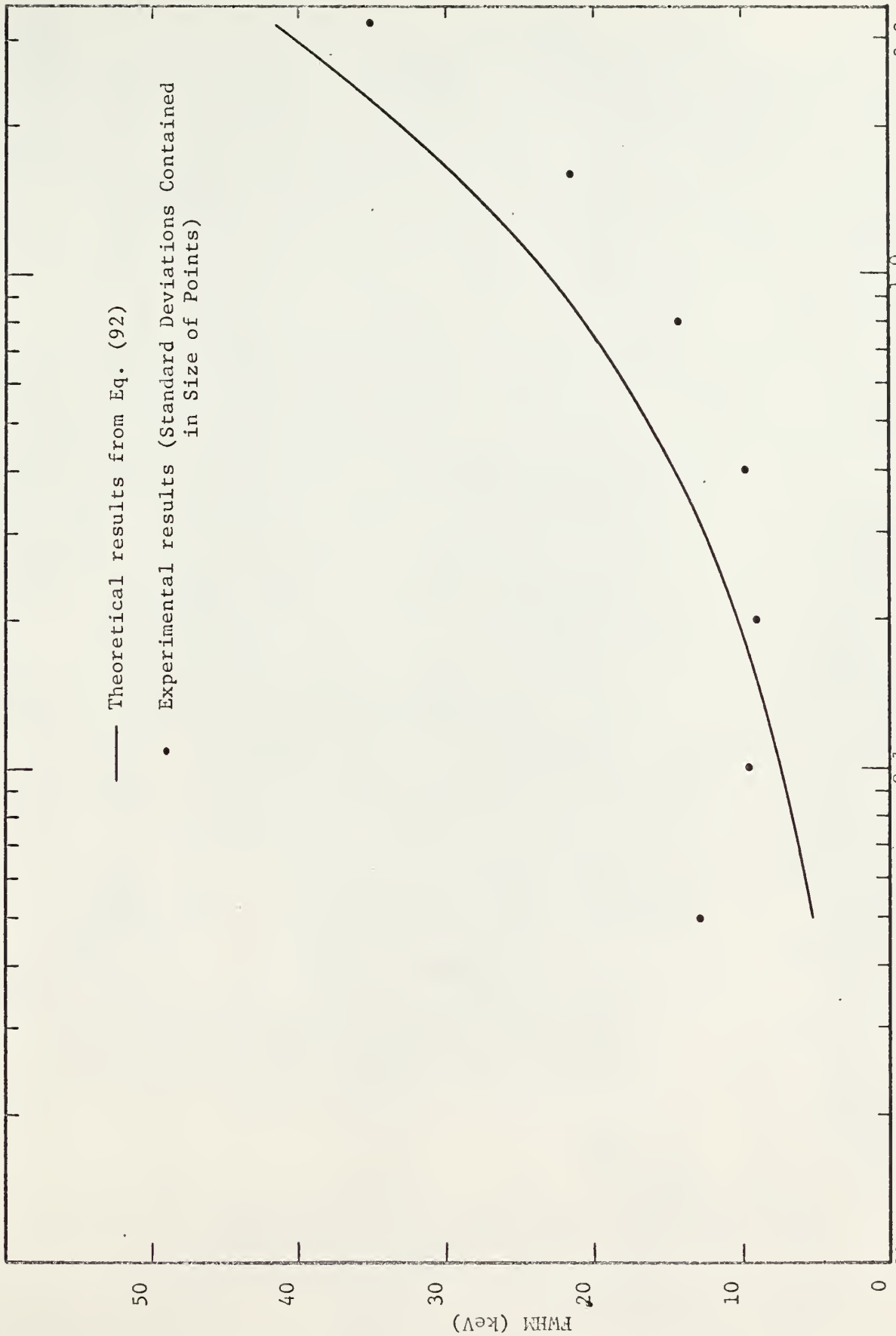

Fig. 23. Variation of Energy Resolution Spreading Due to Detector Noise with Amplifier Time Constant (Detector Bias = 40 Volts)

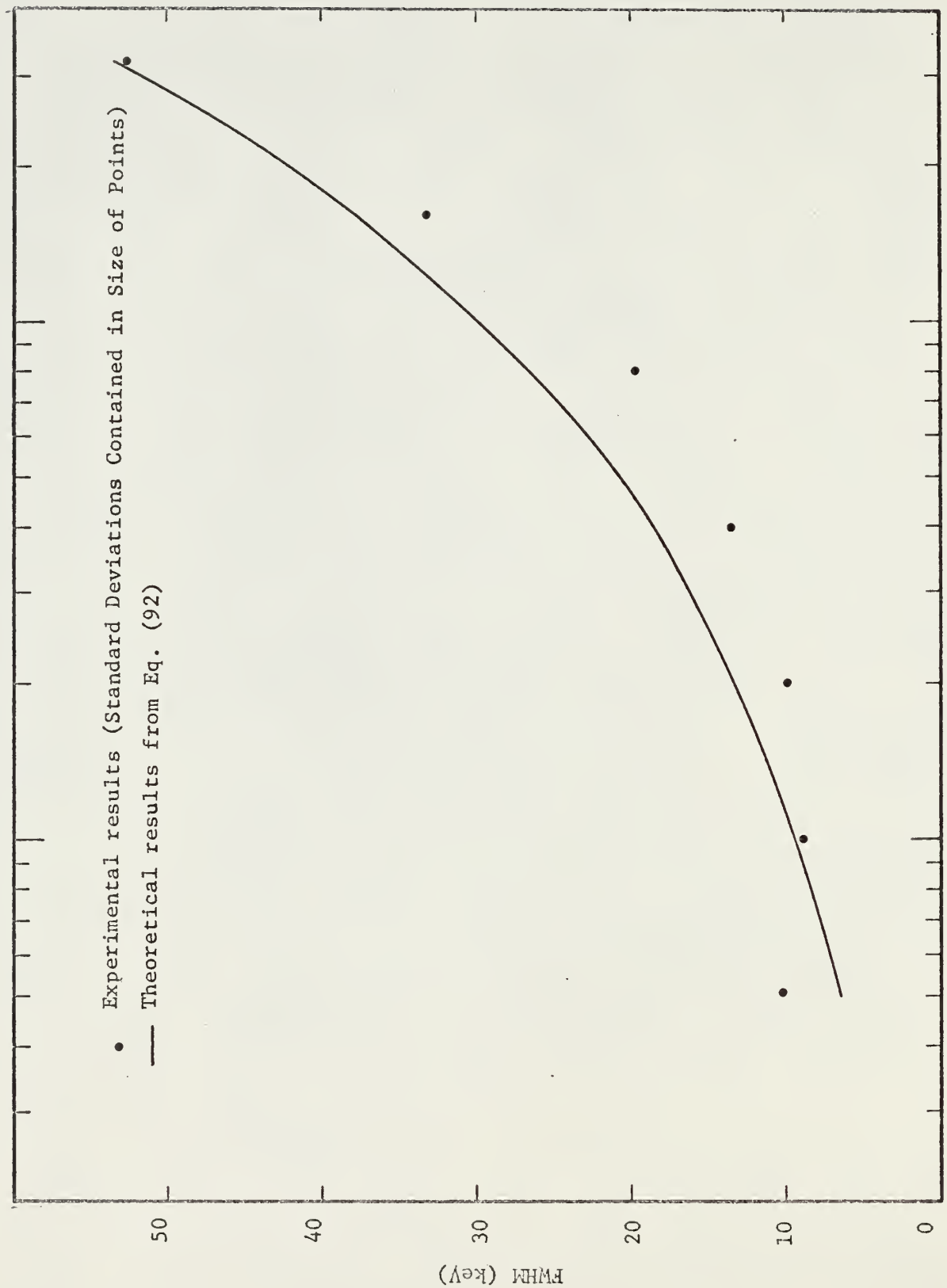

Fig. 24. Variation of Energy Resolution Spreading Due to Detector Noise with Amplifier Time Constant (Detector Bias = 70 Volts)

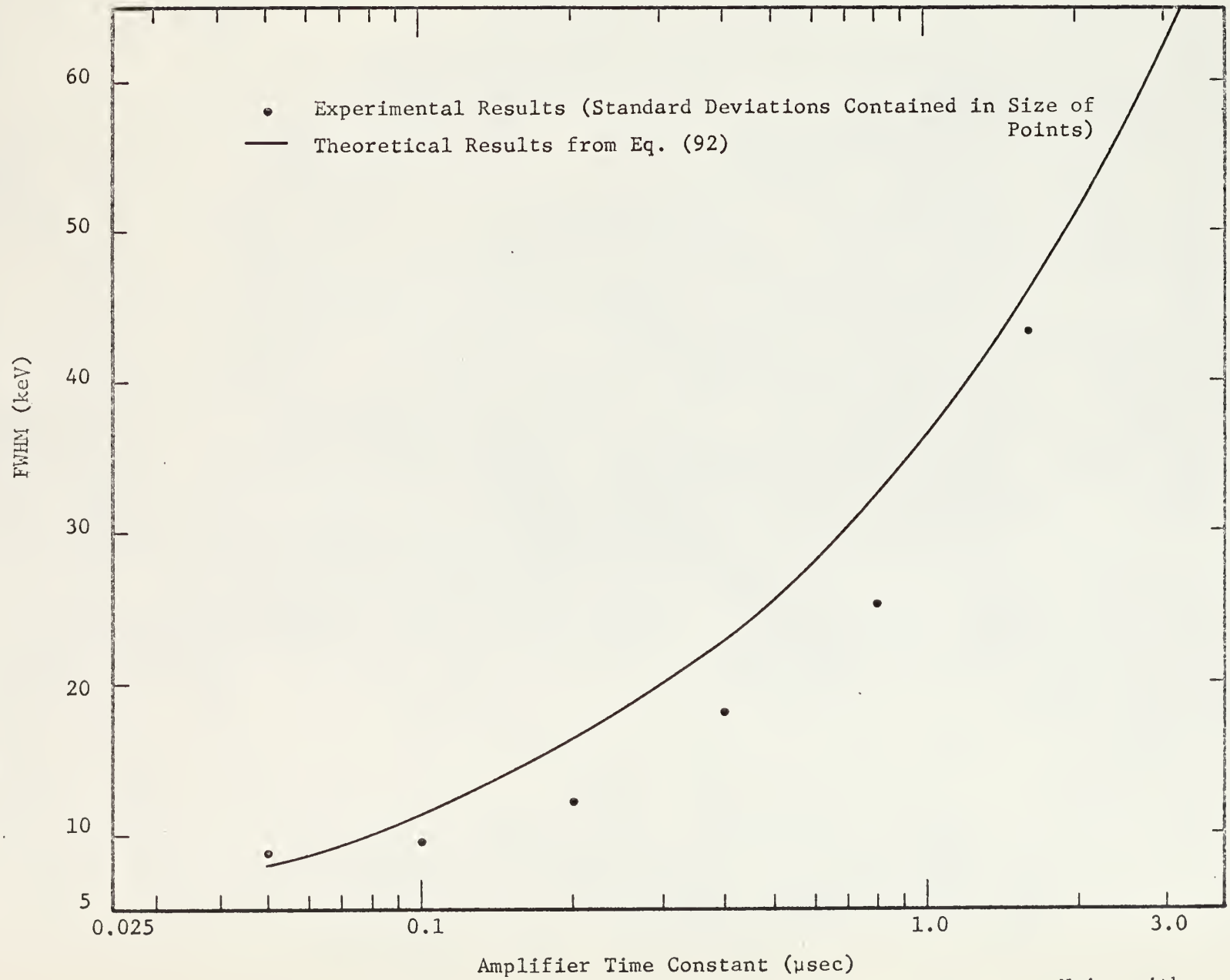

Fig. 25. Variation of Energy Resolution Spreading Due to Detector Noise with Amplifier Time Constant (Detector Bias = 100 Volts)

detector noise and predictions according to Eq. (92), an attempt was made to fit the data (FWHM vs $I_d\tau$) by the least-squares method to several functions. These functions and the data are shown in Fig. (26). The prediction of Eq. (92) is included for comparison purposes. For values of $I_d\tau$ less than 0.1, the FWHM data begins to increase in value, and these data were not used in the fitting procedure. The function FWHM = $a_1 + b_1 I_d\tau$ fits the data very well for the range of $I_d\tau$ of most utility ($0.1<I_d\tau<2.5$). The function FWHM = $a_3 + b_3\sqrt{I_d\tau} + C_3 I_d\tau$ fits the data most closely over the range of $0.1<I_d\tau<5.0$.

When the detector temperature was reduced to approximately 9°C, the detector current decreased from 1.68 μA to 1.52 μA, and experimental detector noise (FWHM) increased from 18.1 ± 0.1 keV to 20.8 ± 0.1 keV. Eq. (92) predicts 22.6 keV. Cooling the detector should have reduced the noise as well as the detector leakage current (20). It is possible that the cooling reduced only the surface leakage current not contributing to the detector noise. This author can give no explanation for the slight increase in detector noise as the detector temperature was lowered.

Optimum spectrometer operating conditions based only on Eq. (92) are low values of detector bias voltage (low leakage current) and low values of τ. Other considerations such as charge collection must be taken into account when determining the true optimum conditions.

4.3 Spectrometer Response to ^{241}Am Alpha Particles

Two representative alpha particle energy spectra taken with the experimental apparatus are shown in Figs. (27) and (28). The spectrum of Fig. (27) was taken at 298°K with a detector bias of 40 Volts and an amplifier time constant of 0.4 μsec. The spectrum of Fig. (28) was taken at 298°K

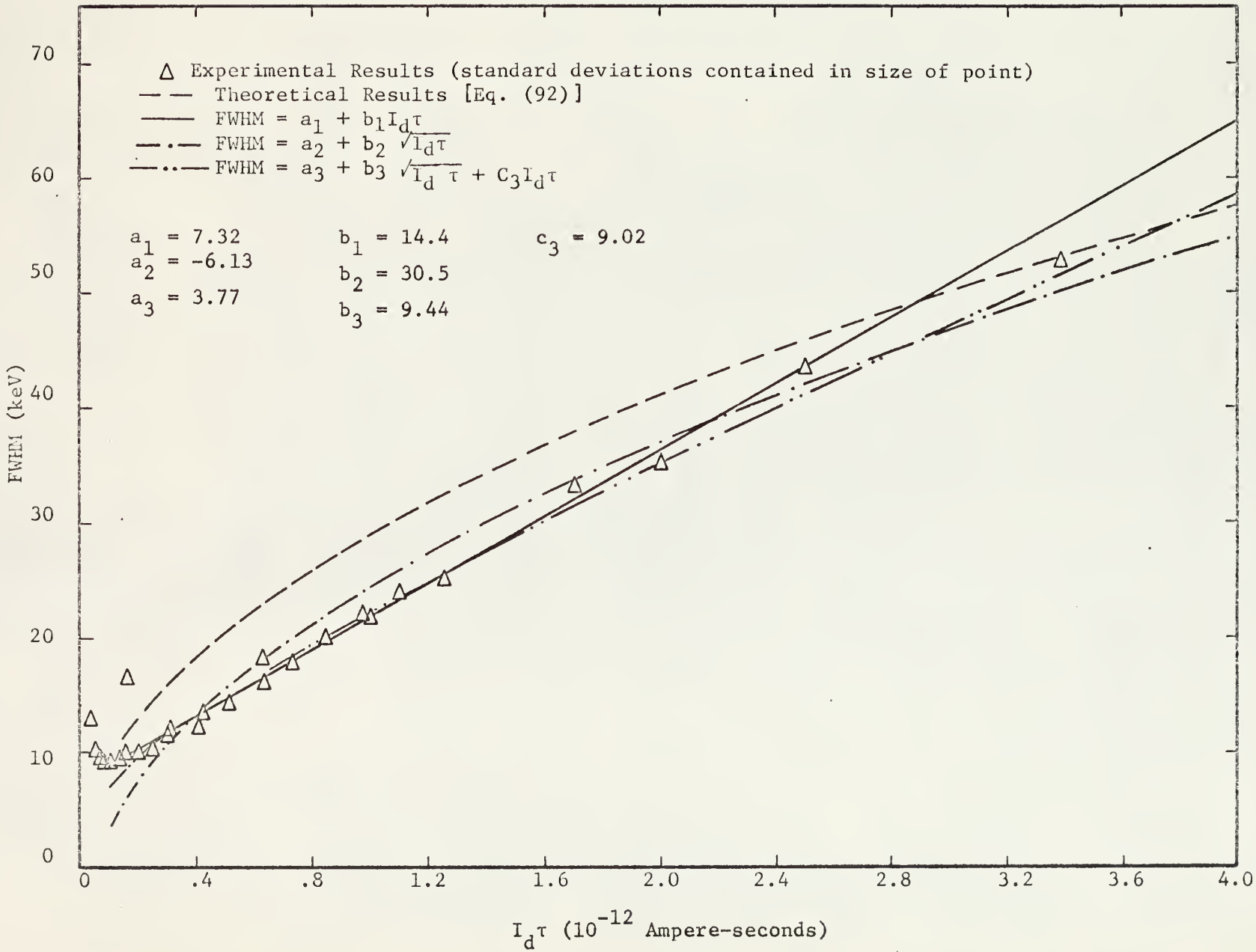

Fig. 26. Least Squares Fit of Several Functions to the Energy Resolution Spreading FWHM Due to Detector Noise as a Function of $I_d\tau$

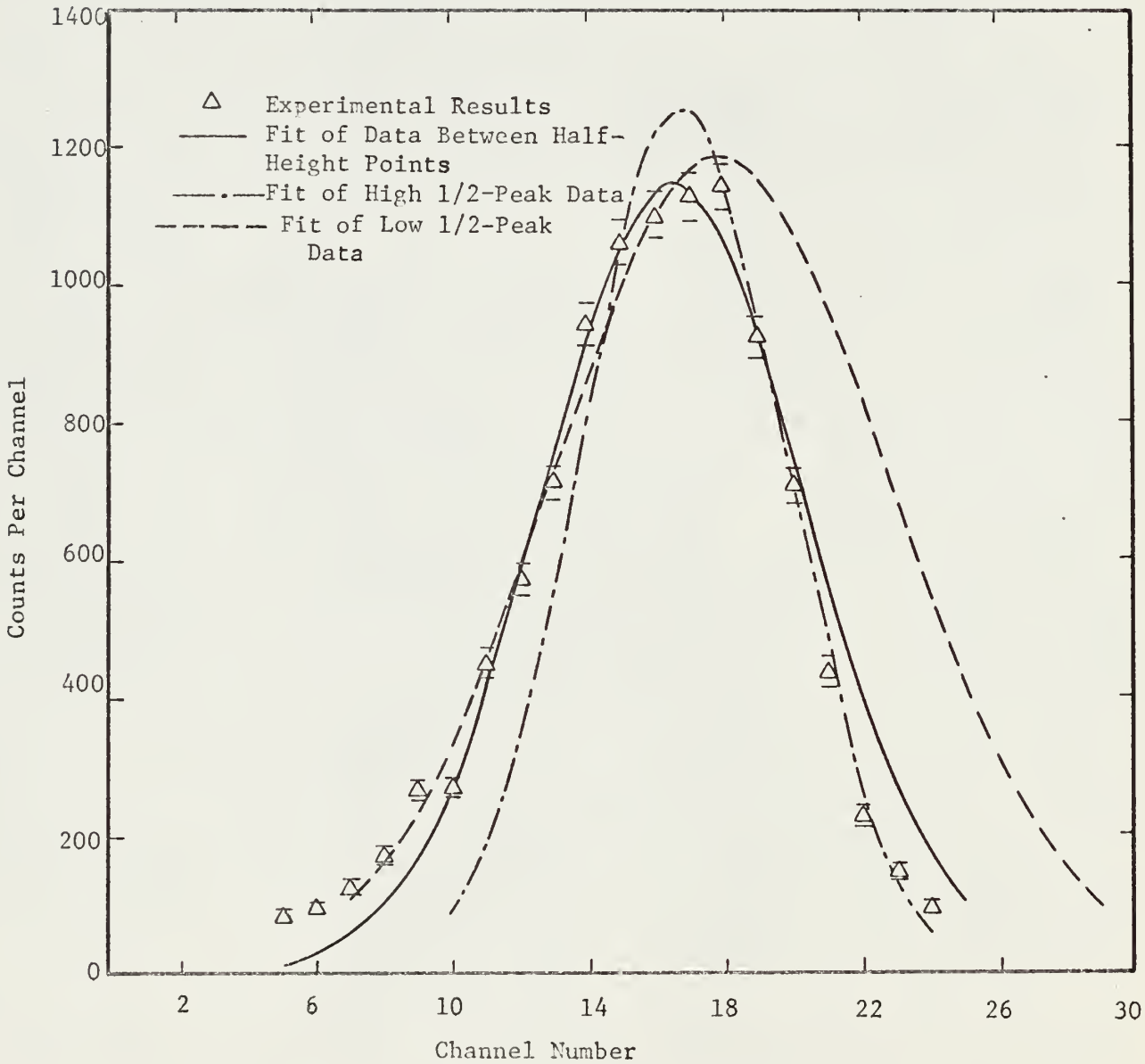

Fig. 27. Measured Alpha Particle Energy Spectrum Showing Three Different Data Fitting Procedures (V_{bias} = 40 Volts and τ = 0.4 μsec)

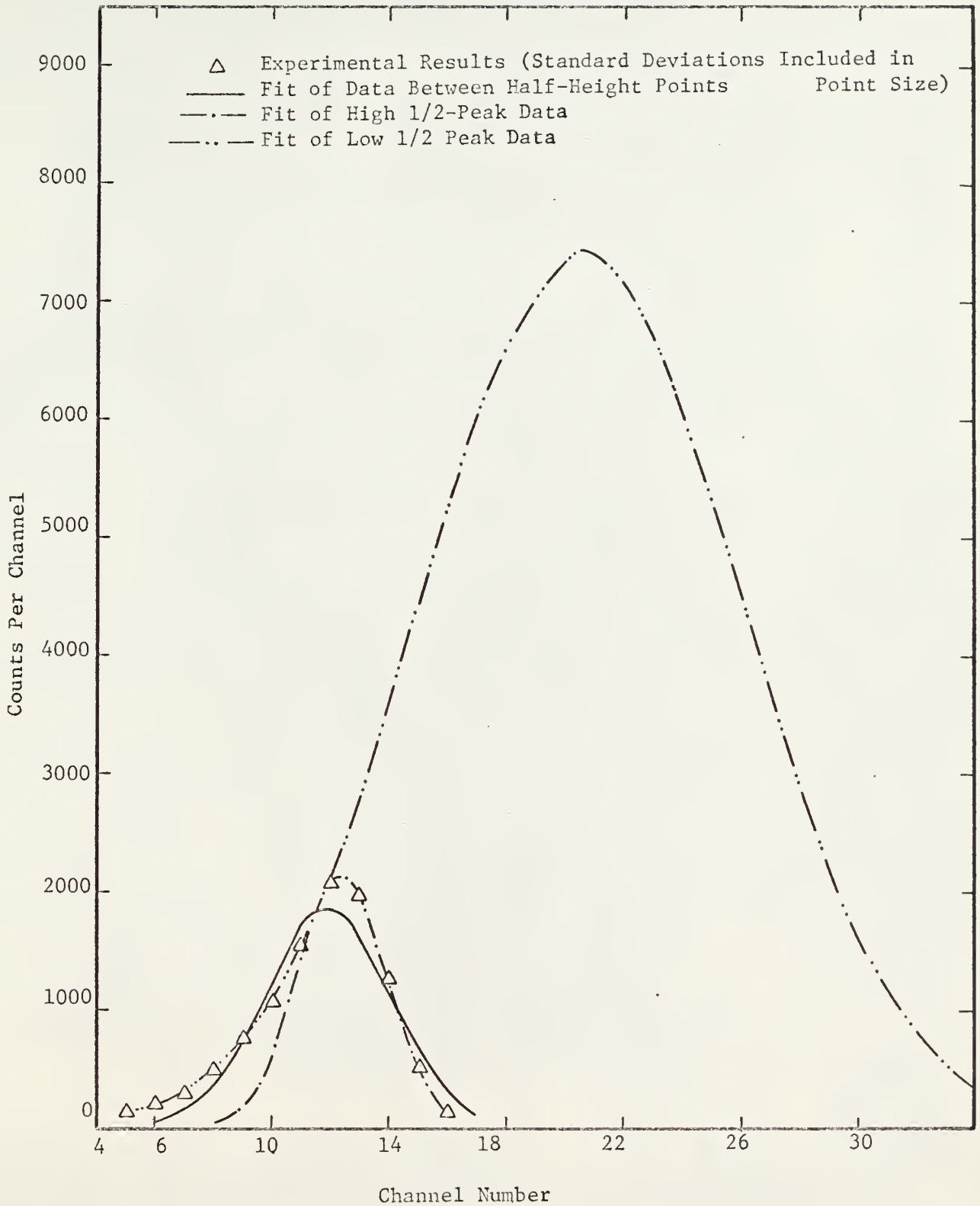

Fig. 28. Measured Alpha Particle Energy Spectrum Showing Three Different Data Fitting Procedures (V_{bias} = 100 Volts and τ = 0.4 μsec)

with a detector bias of 100 Volts and an amplifier time constant of 0.4 μsec. It is clear that neither of the spectra exactly follows a normal distribution. Both have higher counts in the lower channel numbers than would be expected of a true normal distribution. Two explanations for this deviation of the data from the normal distribution are as follows: Roux (22) found that the energies of uncollimated alpha particles which had traversed a thin absorber were described by an energy distribution having a higher probability for low energy particles than that predicted by a normal distribution [see Fig. (4)]. Collimation of the alpha particles in the experiment was achieved by a relatively large source-to-detector distance. The detector thus intercepted a small solid angle as measured from the source, and the alpha particle paths were nearly parallel to each other. This collimation may not have been adequate, and some low energy tail on the energy distribution may have resulted.

Another possible cause of the low energy tail is the existence of 5.435 MeV alpha particles from the ^{241}Am source. These emissions are given off 12 per cent of the time, while the emissions of main concern in this work, 5.477 MeV alpha particles, are emitted 85 per cent of the time. Alpha particles of several other energies are given off very rarely and may be assumed to have a negligible effect on the measured energy spectra. The 5.435 MeV alpha particles are emitted only 42 keV lower in energy than the 5.477 MeV particles. The resolution of the spectrometer was not sufficient to separate these two particle energies adequately. Therefore, the lower energy peak contributes to the low energy tail of the alpha particle spectrum.

In order to compare the theoretical predictions for the FWHM of the

alpha particle spectra, each experimental energy spectrum was fitted with three normal distributions represented by Figs. (27) and (28). The first data fit used only the data appearing between the channels corresponding to the half-heights of the energy distribution. The second data fit used only the data appearing in channel numbers equal to and greater than the channel in which the most counts were collected. The third data fit used only the data appearing in channel numbers equal to or less than the channel number in which the most counts were collected. The theoretical expression for the alpha particle spectrum FWHM was derived assuming a normally distributed spectrum. No allowance was made in the theoretical expression for uncollimated alpha particles or for lower energy emitted alpha particles. Therefore, the theoretical predictions for the FWHM were compared with the FWHM of the experimental data determined by the data fit using only the data in channels higher than or equal to the channel in which the most counts were collected. The data fit using data in channel numbers lower than or equal to the channel in which the most counts were collected is shown in Figs. (27) and (28) to illustrate the low energy tail effect.

The FWHM of the data shown in Figs. (27) and (28) for the different fits used are given in Table II.

TABLE II. Alpha Particle Energy Spectrum FWHM for Different Data Fitting Procedures.

Figure	V_{bias} (Volts)	FWHM (keV) (Data Used Between Half-Height)	FWHM (keV) (High Energy 1/2 Fit)	FWHM (keV) (Low Energy 1/2 Fit)
27	40	124.6 ± 3.0	95.1 ± 6.4	159.7 ± 5.0
28	100	64.51 ± .82	45.6 ± 1.1	163. ± 20.

The variation of the alpha particle energy spectrum FWHM with respect to detector bias voltage is given in Fig. (29). Agreement between the theoretical expression [Eq. (90)] and data does not become close except at the highest bias voltages. This disagreement can be explained by charge collection problems in the detector (explained in Section 2.3) which become more acute as the detector bias is decreased.

The variation of the alpha particle energy spectrum FWHM with respect to τ, the amplifier time constant, for different detector bias voltages is given in Fig. (30) for V_{bias} = 40 Volts, Fig. (31) for V_{bias} = 70 Volts, and Fig. (32) for V_{bias} = 100 Volts. Both theoretical and experimental values are given. Agreement is generally not close except for the case where V_{bias} = 100 Volts and τ = 0.8 μsec.

The experimental FWHM's exhibit a minimum value as τ is varied. This minimum value occurs at smaller values of τ as the detector bias is increased (and thus detector leakage current is increased). This variation of $\tau_{optimum}$ with detector bias voltage is qualitatively predicted by the theoretical expression, but predicted τ's are lower in value than measured quantities.

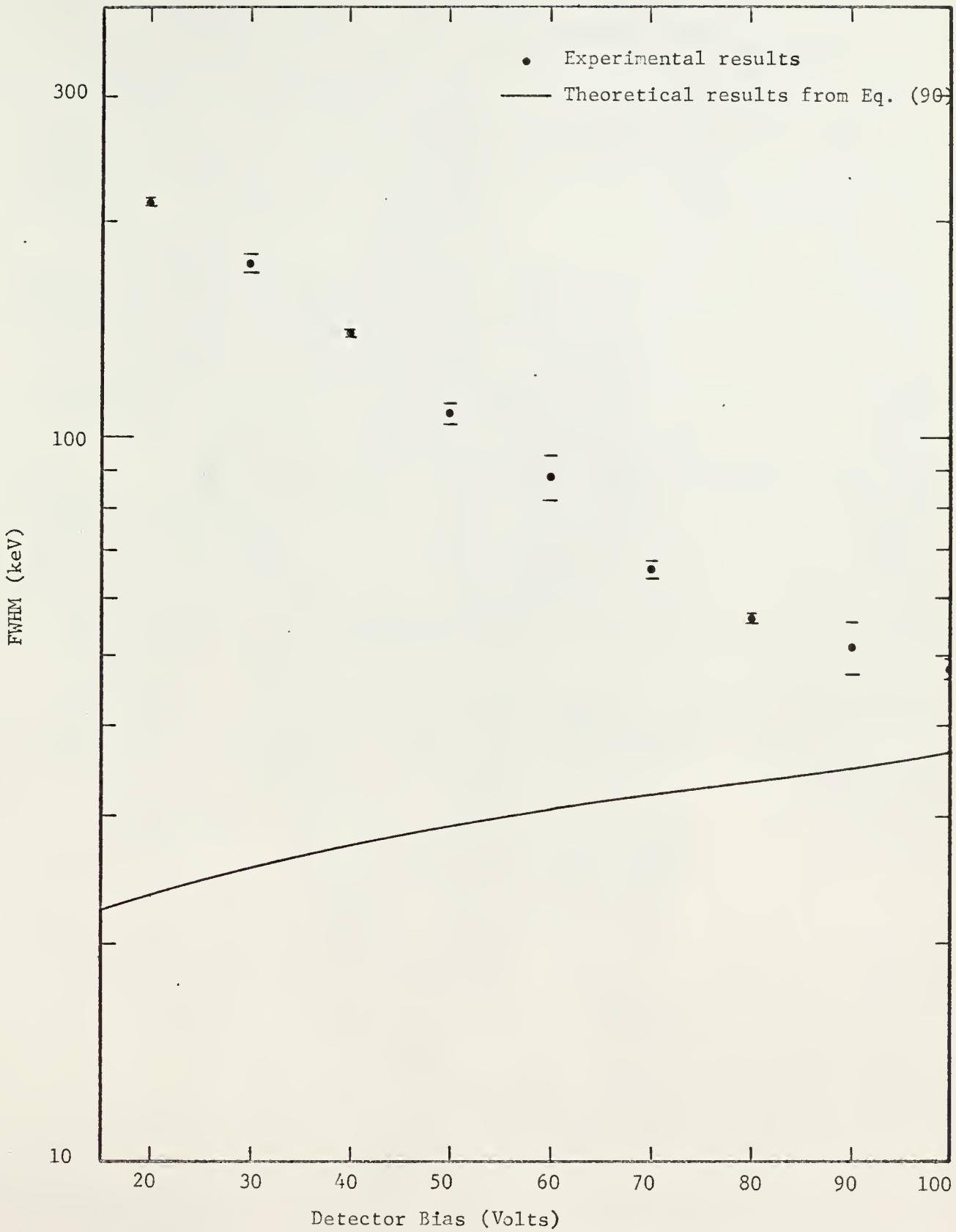

Fig. 29. Variation of Energy Resolution of the Spectrometer to ^{241}Am Alpha Particles with Detector Bias Voltage (τ = 0.8 μsec)

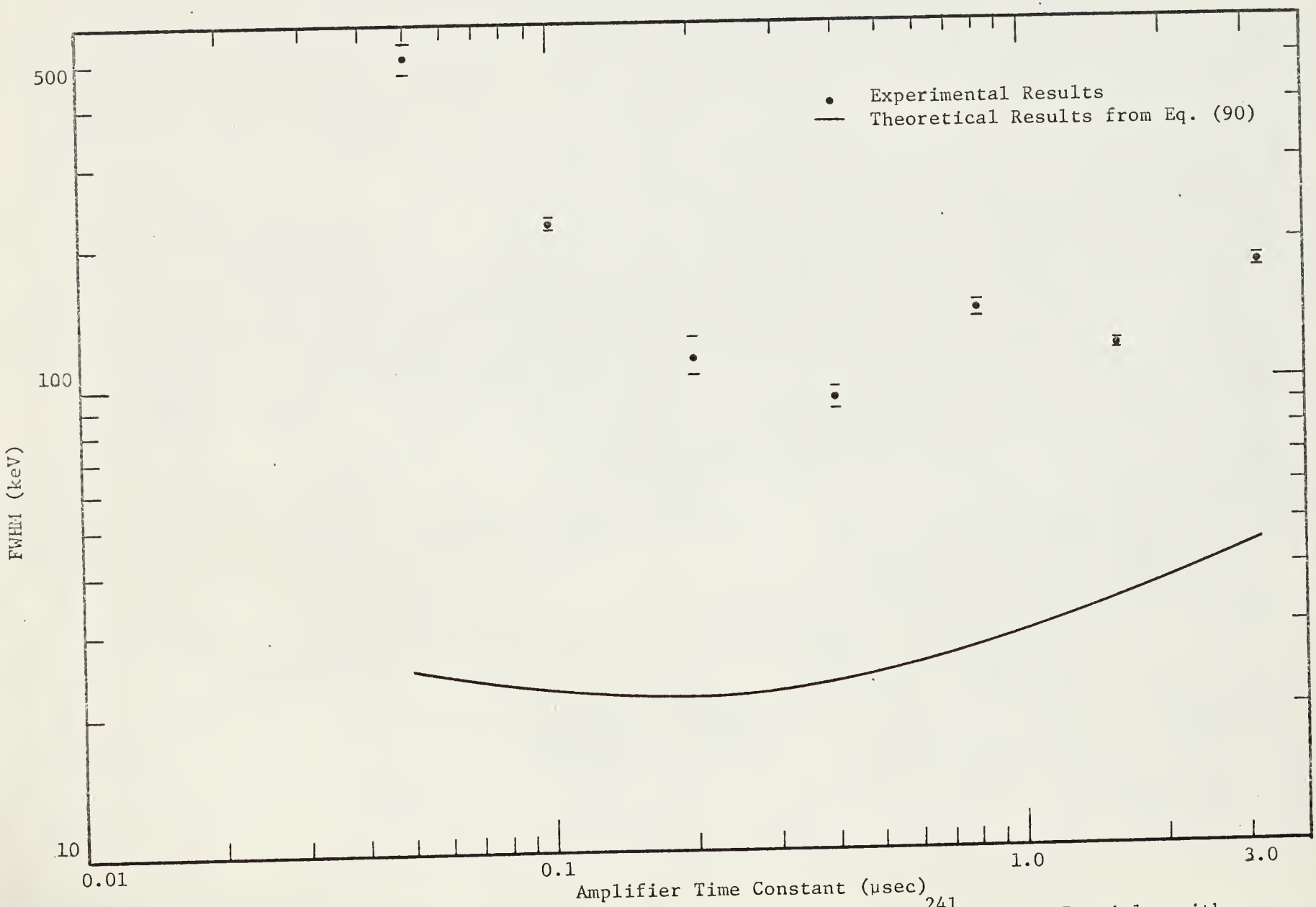

Fig. 30. Variation of Energy Resolution of the Spectrometer to ^{241}Am Alpha Particles with Amplifier Time Constant (V_{bias} = 40 Volts)

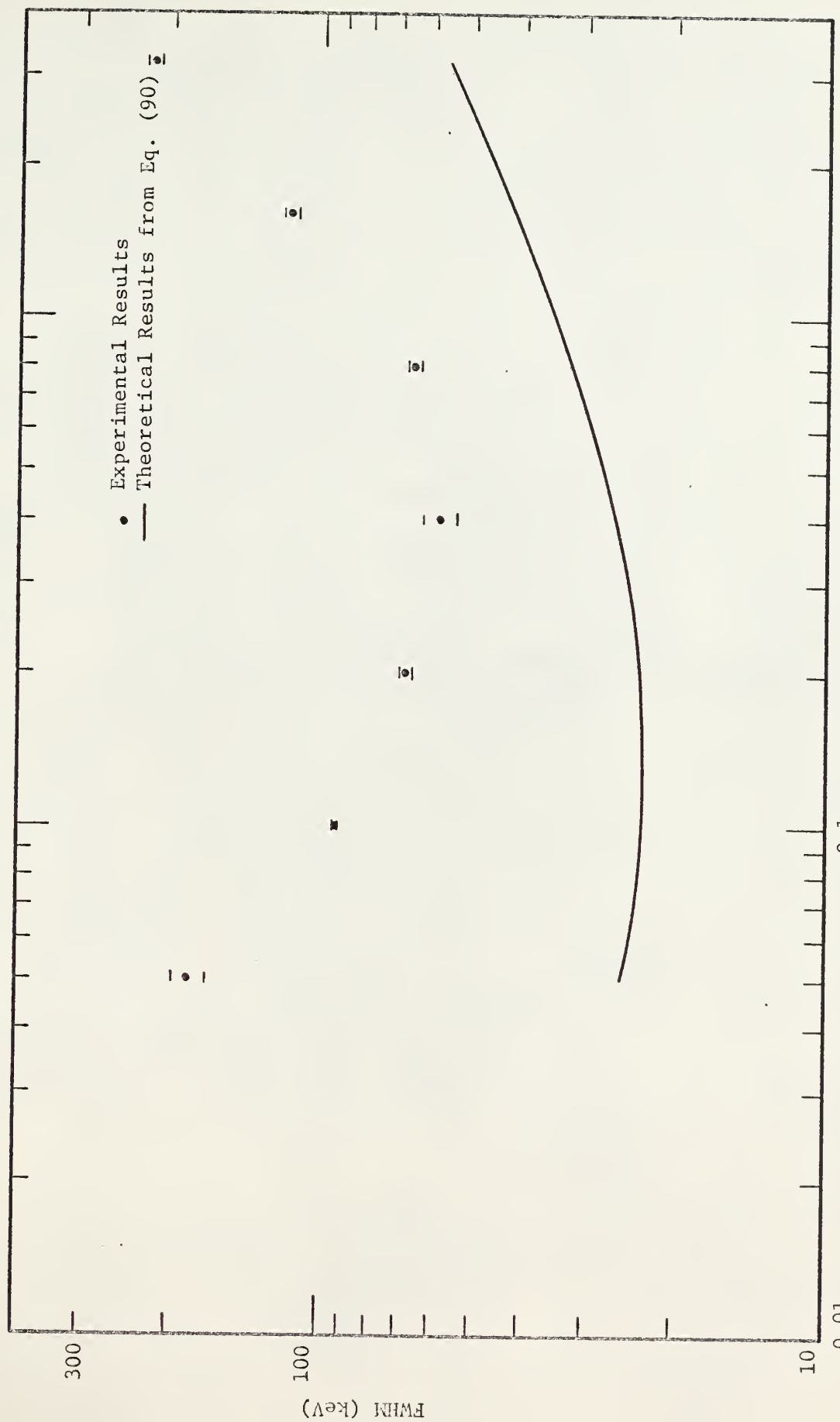

Fig. 31. Variation of Energy Resolution of the Spectrometer to ^{241}Am Alpha Particles with Amplifier Time Constant (V_{bias} = 70 Volts)

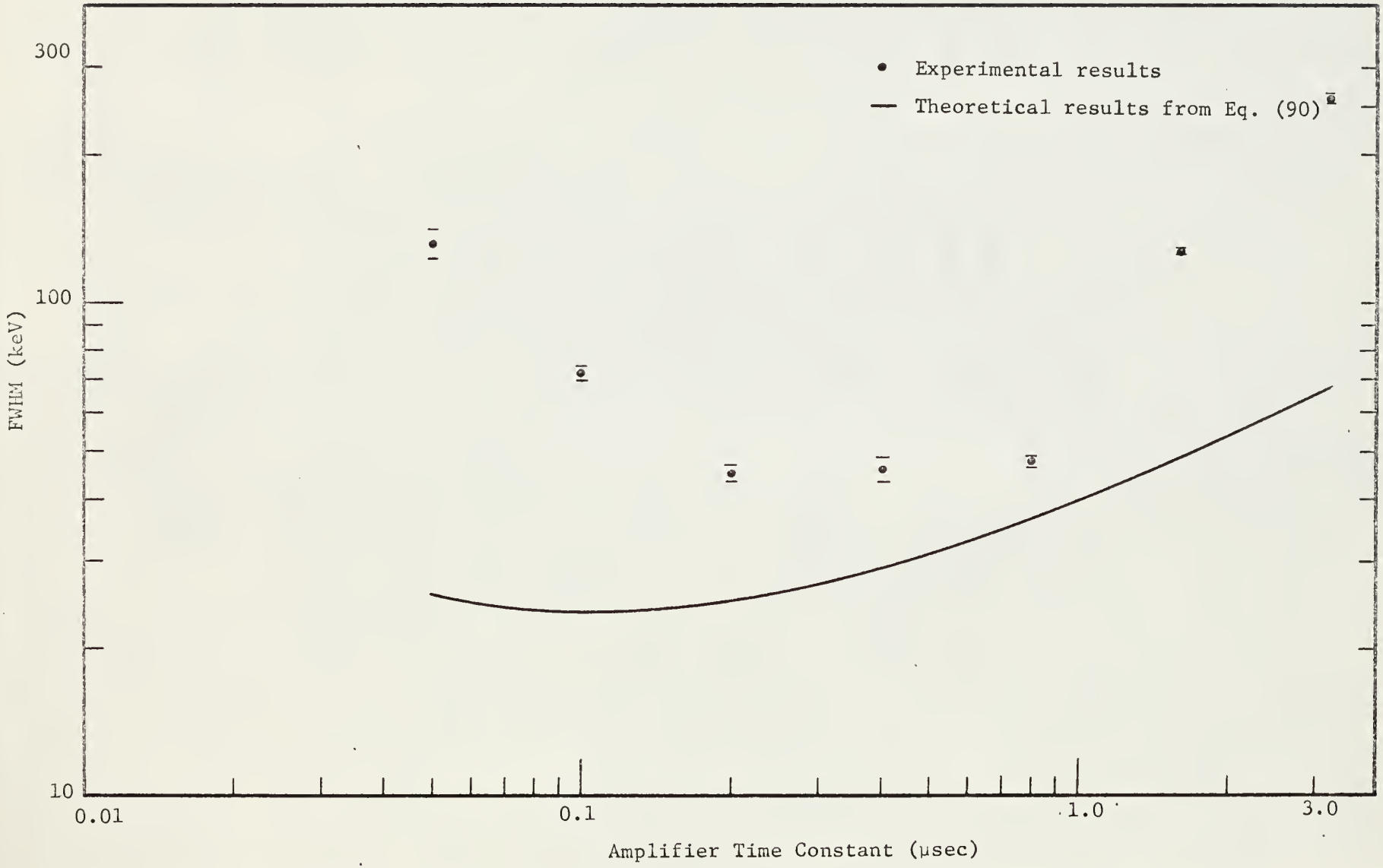

Fig. 32. Variation of Energy Resolution of the Spectrometer to ^{241}Am Alpha Particles with Amplifier Time Constant (V_{bias} = 100 Volts)

The FWHM resulting from subtracting the theoretical energy resolution variances due to particle statistics in the detector, detector window, source self-absorption, and measured amplifier plus detector noise from the total alpha particle energy spectrum is shown in Fig.'s (33) and (34). This FWHM is a measure of the energy resolution spreading due to incomplete charge collection and possibly other unknown energy resolution spreading effects. Fig. (33) shows the variation of this excess FWHM with respect to the detector bias voltage. The excess FWHM decreased as the bias voltage increased. This behavior of the excess FWHM corresponds to that behavior expected from charge collection problems.

Fig. (34) illustrates the variation of the excess FWHM with respect to amplifier time constant. The excess FWHM seems to depend on two competing effects as τ is varied. One effect is proportional to some positive power of τ, the other proportional to some negative power of τ. This author can offer no explanation of a charge collection mechanism which would behave in this manner with respect to τ.

Lowering the detector temperature from $298^{o}K$ to $282^{o}K$ reduced the alpha spectrum FWHM from 46.0 ± 2.6 keV to 37.9 ± 2.7 keV. The detector bias was 100 Volts, and the amplifier time constant was 0.4 μsec when these data were taken. The decrease of FWHM with decreasing temperature was not due to a decrease in detector noise. Different PHA's were used to take data at the different temperatures. This could account for some of the difference in FWHM taken at the two temperatures.

A Student's t-test (4) was performed on the FWHM's and standard deviations taken at the two temperatures to determine if the difference in the mean values was significant. It was found that the difference was not

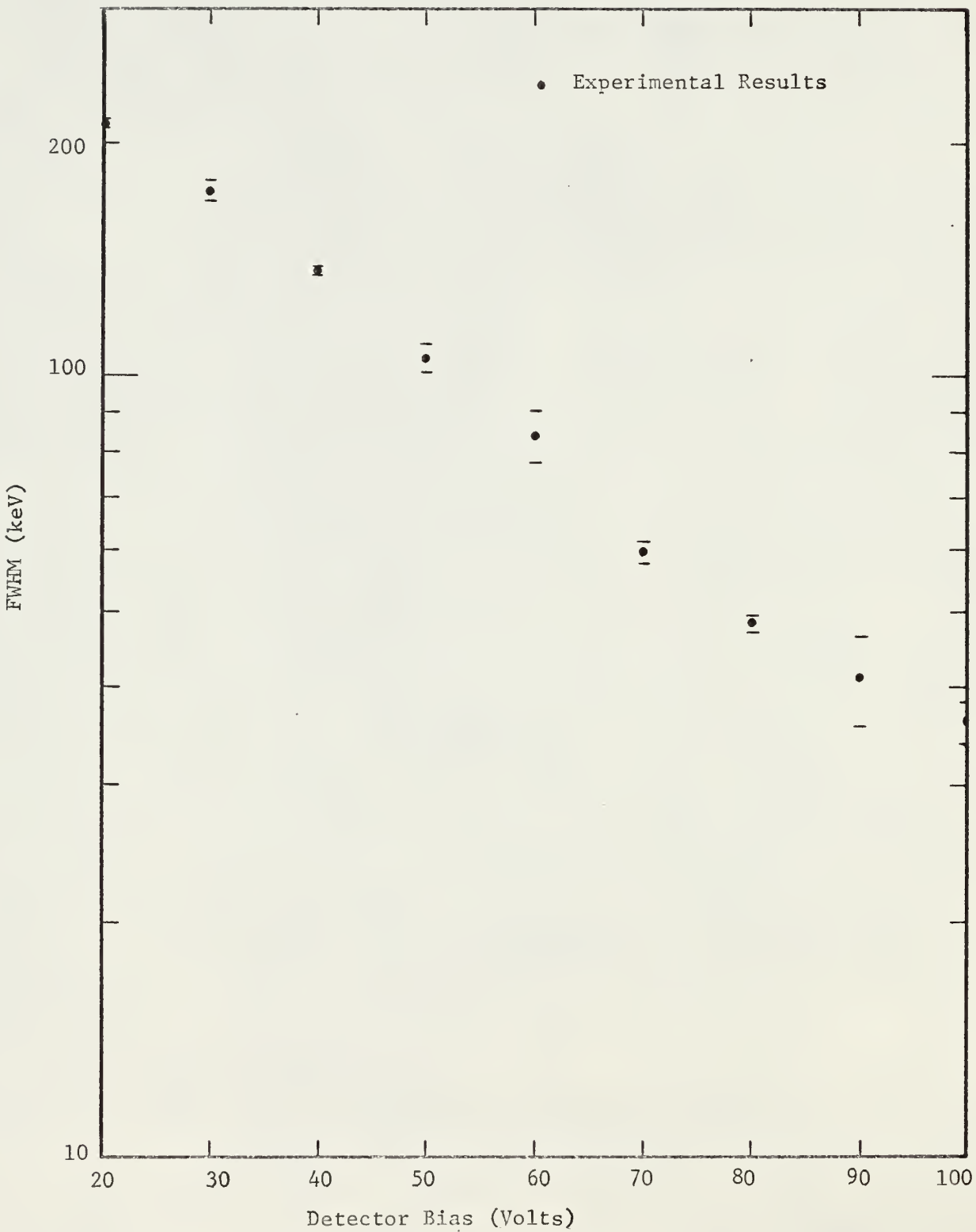

Fig. 33. Variation of Excess Energy Resolution Spreading FWHM with Detector Bias Voltage (τ = 0.8 μsec)

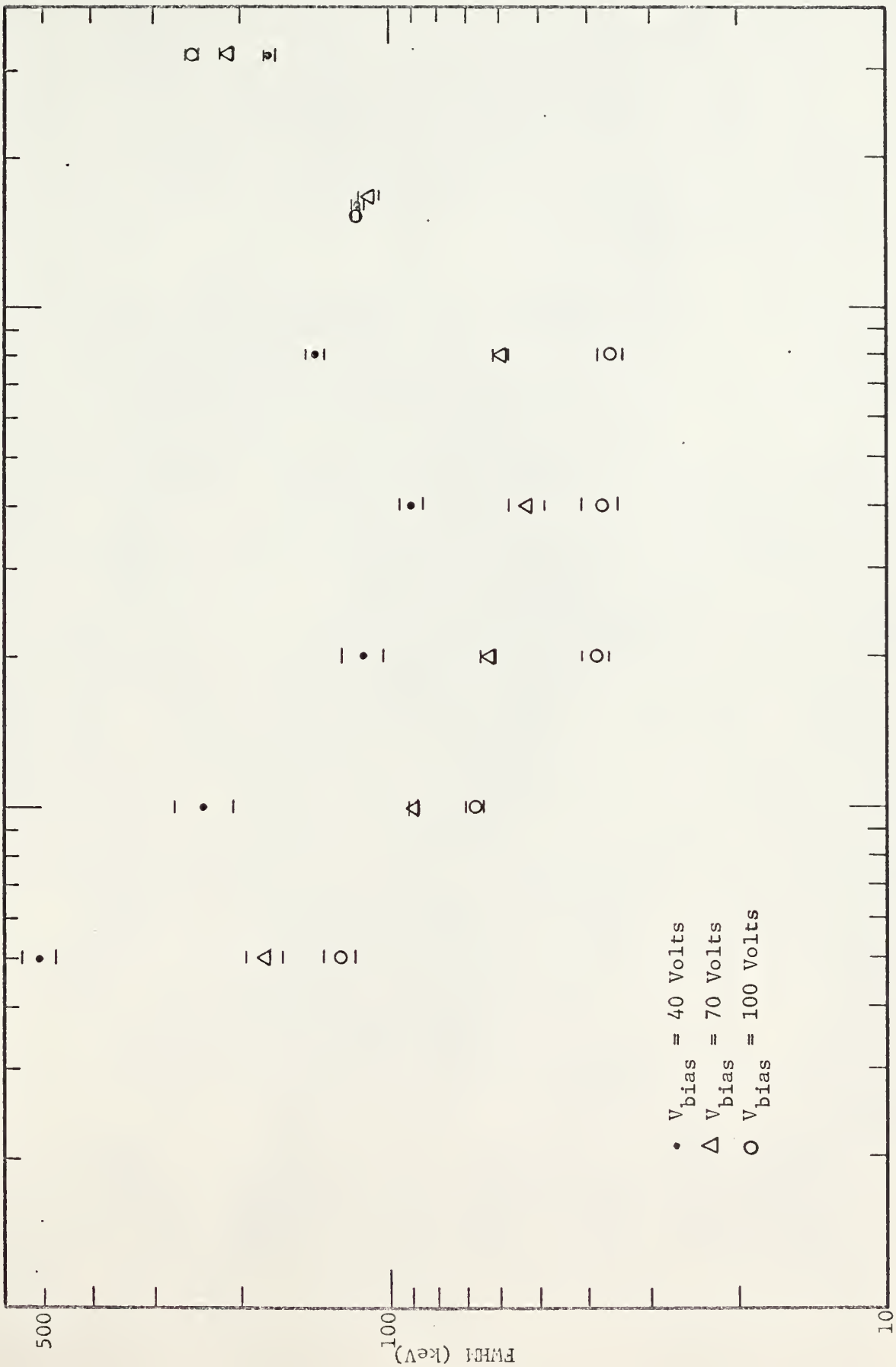

Fig. 34. Variation of Excess Energy Resolution Spreading FWHM with Amplifier Time Constant (V_{bias} = 40, 70, and 100 Volts)

significant at the .05 level.

4.4 Conclusions

The attempt to predict the contributions to the total alpha particle energy spectrum resolution spreading due to amplifier and detector noise was a qualified success. The detector leakage current was excessive, which led to relatively high predictions of detector noise. Predicted values of total alpha particle spectrum FWHM were lower than experimental FWHM's due to serious charge collection problems in the detector. In most cases this charge collection difficulty contributed more to the energy resolution spreading than the total of all other known effects. The agreement between the predicted optimum amplifier time constant for the spectrometer to incident alpha particles was fortuitous since the theoretical expression for the total FWHM could not account for the charge collection effect, the major contributor to the FWHM. A valid prediction for the total FWHM must await a quantitative theory for the resolution degradation due to charge collection difficulties.

The improvement of energy resolution due to reduced detector temperature was not verified by this work. The equipment was not suitable to reduce the detector temperature significantly.

5.0 SUGGESTIONS FOR FURTHER STUDY

The detector used in this work appeared to suffer from a deterioration of surface conditions after being placed in the vacuum chamber. Part of this problem may have been caused by vacuum pump oil contamination. The contamination problem could be reduced in further work by a better pump and a zeolite trap between the pump and the detector chamber.

Detector energy resolution could be improved by cooling the detector temperatures significantly lower than ambient. A new detector chamber designed with a cooling provision would be required.

Premium grade detectors are available which have better energy resolution characteristics than the device used in this work. Future work requiring good energy resolution should be performed with a premium grade detector.

More study is warranted of the charge collection problem inherent in this type of detector. The relative importance of the recombination effect could be studied by taking FWHM measurements of beta particle energy spectra. The beta particles produce fewer ion pairs per unit path length and therefore recombination effects would be reduced. Study of the behavior of the excess noise (as defined in this paper, not $^{1}/_{f}$ noise) with respect to the amplifier time constant is warranted. This excess noise is believed to be linked to the charge collection process.

Autocorrelation techniques could be used to determine the frequency distribution of detector noise power, both with and without ionizing particles intercepting the detector. This technique could yield information about noise producing mechanisms in the detector.

6.0 ACKNOWLEDGMENTS

The author wishes to express his sincere gratitude to Drs. N. D. Eckhoff and R. E. Faw for their guidance, assistance, and contributions to this work. Appreciation is given to Dr. C. G. Chezem, Head of the Department of Nuclear Engineering, for his assistance. Thanks are extended to R. E. Hightower for his instrumentation advice and to G. W. Abshire for his help in constructing the experimental apparatus. The assistance of the KSU Computing Center is acknowledged, and the loan of equipment by the Departments of Electrical Engineering and Mechanical Engineering is sincerely appreciated. The contributions of members of the staff and of other graduate students in the Department of Nuclear Engineering were valuable. Thanks are given to Mrs. Sonja L. Robinson for her help with the manuscript preparation. Gratitude is given to the Office of Civil Defense under whose fellowship program this work was done. Of course, the author's warmest appreciation is given to his wife Nancy, for her assistance, understanding, and encouragement.

7.0 LITERATURE CITED

1. Assembling and Using Your Heathkit Vacuum Tube Voltmeter, Model V-7A, Heath Co., Benton Harbor, Michigan.

2. Baldinger, E., Czaja, W. and Gutman J.
Proceedings of Symposium on Nucl. Instr. (Harwell, Sept. 1961), edited by J. B. Birks, Heywood & Co., London, 1962.

3. Bliss, C. E., Eckhoff, N. D. and Donnert, H. J. A.
Fluence Measurement of 14.7 MeV Neutrons, Unpublished Paper, Dept. of Nuclear Engineering, Kansas State University.

4. Brownlee, K. A.
Statistical Theory and Methodology In Science and Engineering, John Wiley & Sons, Inc., New York, 1965.

5. Dearnaley, G. and Northrop, D. C.
Semiconductor Counters for Nuclear Radiations, Barnes and Noble, Inc., 1966.

6. Ehrlich, W. K.
Private communication, Nuclear Supplies Inc., Encino, California, Nov. 1968.

7. Elmore, W. C.
Electronics for the Nuclear Physicist, Nucleonics, Vol. 2, Feb. 1948.

8. Fano, U.
Ionization Yield of Radiations II. The Fluctuations of the Number of Ions, Phys. Rev., Vol. 72, No. 1, pp. 26-29, July, 1947.

9. Gillespie, A. B.
Signal, Noise, and Resolution in Nuclear Counter Amplifiers, McGraw-Hill Book Co., New York, 1953.

10. Goulding, F. S. and Hansen, W. L.
Leakage Current in Semiconductor Junction Radiation Detectors and Its Influence on Energy-Resolution Characteristics, Nucl. Instr. & Methods, Vol. 12, pp. 249-262, 1961.

11. Harris, E. J.
Noise Data for Low Audio Frequency Apparatus, Paper II of C.V.D. Discussion on Flicker Noise, Dept. of Physical Research, Admiralty, July 1947.

12. Instruction Manual for 515A Oscilloscope, Tektronix Inc., Beaverton, Oregon, 1960.

13. Instruction Manual for Model 101-201 Low Noise Amplifier System, Oak Ridge Technical Enterprises Corp., Oak Ridge, Tennessee.

14. Instruction Manual for Model. PA-10 FET Preamplifier, Nuclear Equipment Corp., San Carlos, Calif.

15. Instruction Manual for Surface Barrier Detectors, Oak Ridge Technical Enterprises Corp., Oak Ridge, Tennessee, 1964.

16. Johnson, J. B.
Thermal Agitation of Electricity in Conductors, Phys. Rev., Vol. 32, pp. 97-109, July 1928.

17. Masuda, M. and Takeda, S.
Leakage Current and Noises In Surface Barrier Particle Detectors, Nucl. Instr. & Methods, Vol. 49, pp. 77-85, 1967.

18. Monteith, L. K.
Correlation of I-V Characteristic with Noise for Ion Drifted p-i-n Junction Particle Detectors, Rev. Sci. Instr., Vol. 35, No. 3, pp. 388-392, 1964.

19. Pell, E. M.
Ion Drift in an n-p Junction, J. Appl. Phys., Vol. 31, No. 2, pp. 291-302, Feb. 1960.

20. Practical Guide to Semiconductor Detectors, Technical Measurements Corp., North Haven, Conn., 1965.

21. Price, W. J.
Nuclear Radiation Detection, McGraw-Hill Book Co., New York, 1964.

22. Roux, G.
Influence of the Dead Layer of Semiconductor Detectors on the Precision of Energy Measurements of Particles, Nucl. Instr. Methods, Vol. 33, pp. 329-331, March 1965.

23. Schottky, W.
Spontaneous Current Fluctuations in Various Conductors, Ann. Physik, Vol. 57, 1918.

24. Shockley, W.
B.S.T.J., Vol. 30, 1951.

25. Taylor, J. M.
Semiconductor Particle Detectors, Butterworths, London, 1963.

26. van der Ziel, A.
Noise, Prentice-Hall, Inc., N. J., 1956.

27. Williamson, C. and Boujot, J. P.
CEA-2189 (1962).

APPENDIX A

Theory of the Lithium-Drifted Semiconductor Detector

Many references are available concerning the theory of operation of lithium-drifted semiconductor detectors (5, 21, 25). The following discussion reviews the literature cited and is not intended to be a complete development of detector theory.

The lithium-drifted semiconductor detector is similar in operation to the diffused p-n junction radiation detector. It has the advantage of a relatively thick sensitive volume allowing accurate measurement of the total ionization produced by incident high energy particles. This detector is noted for low leakage current at ambient temperatures.

The technique of producing lithium-drifted detectors was originated by Pell (19). The detector material usually employed is very high purity silicon containing a small percentage of the acceptor impurity, boron, which is the most difficult impurity to remove. Lithium, an interstitial donor impurity, has a diffusion coefficient nearly 10^7 times that of the more common n-type doping materials (phosphorus, gallium, etc.). In an electric field, lithium ions migrate very readily. The effects of the drifted lithium ions may be made to predominate over diffusion in the temperature range from $100^{\circ}C$ to $400^{\circ}C$.

At room temperature, the boron impurity atoms in the silicon are fully ionized. Donor impurities can be added to the p-type silicon to the extent that the concentration of ionized donors is approximately equal to the concentration of ionized boron acceptors. The concentration of extrinsic carriers is equal to the difference between the two impurity concentrations and is much smaller than either one (5). The only difference be-

tween exactly compensated silicon and true intrinsic silicon is the lower carrier mobilities and lifetimes due to the charged impurity centers in the lattice of the compensated silicon (5).

The compensation of extrinsic carriers is accomplished by the lithium ions drifting in an electric field in the silicon. One surface of a very pure p-type silicon wafer is coated with a lithium suspension. The wafer is heated, and the lithium diffuses into the wafer. The lithium concentration as a function of the distance x into the wafer is shown in Fig. (A-1):

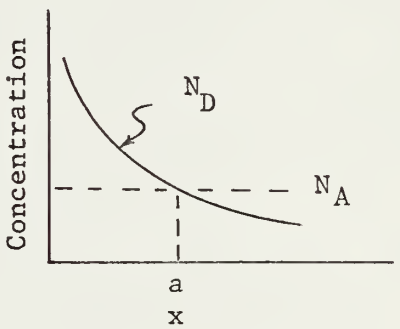

Fig. A-1 Donor and acceptor impurity concentrations. N_D and N_A are the donor and acceptor impurity concentrations, respectively.

At x = a, the concentration of lithium is equal to the acceptor impurity concentration. A reverse electric potential of 10-300 Volts is applied across the thickness of the silicon wafer. The temperature of the wafer is kept between 120°C and 250°C. Under the influence of the electric field, the lithium ions drift deeper into the depleted region of the wafer. The forward ion drift is much larger than the back diffusion in this region:

$$E\mu N_D >> D\vec{\nabla}.N_D \quad , \qquad \text{(A-1)}$$

where E = electric field intensity,

μ = lithium ion mobility,

D = lithium diffusion coefficient.

Where $x<a$, N_D cannot become less than N_A because of the electric field. In the region where $x>a$, N_D cannot be greater than N_A since the resulting space charge would reduce the electric field in that region. The reduced electric field would reduce N_D. In this manner, a region where $N_D = N_A$ exists on both sides of $x = a$ as shown in Fig. (A-2):

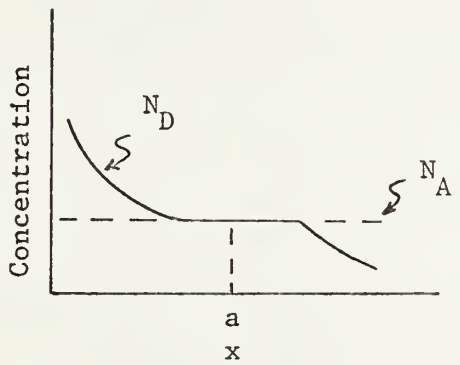

Fig. A-2 Donor and acceptor impurity distributions after drifting process.

The maximum width of the depletion region is attained when back diffusion of the lithium ions equals the forward drift:

$$E\mu N_D = D\vec{\nabla}\cdot N_D \quad . \qquad \text{(A-2)}$$

At deep lithium ion penetrations, the electric field causing the drift is reduced because of the accumulation of the space charge produced by the thermal generation current (25). Thermal generation current is caused by thermally excited charge carriers being swept from the depletion region by the electric field.

When the lithium-drifted detector is operated with a reverse bias, the residual carriers are swept from the intrinsic region. A space charge is developed at both edges of the intrinsic region which results in an electric field distribution as shown in Fig. (A-3):

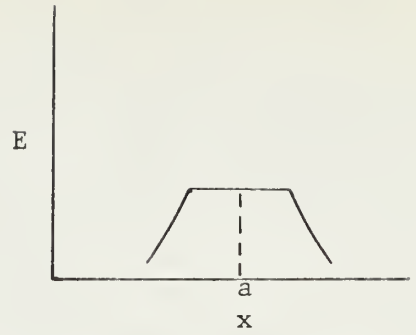

Fig. A-3 Electric field distribution in a lithium-drifted detector under reverse bias

The resistance of the depletion region is very high. Thus, most of the bias voltage appears across the depletion region, thereby producing a very high electric field intensity. Very little leakage current passes through the high resistance of the depletion region. This condition minimizes current leakage noise and detector heating.

When an energetic charged particle traverses the depletion region of a semiconductor detector, it dissipates its energy by producing electron-hole pairs. The average energy dissipated by a 5 MeV alpha particle while producing one electron-hole pair in silicon is 3.61 $\pm$ .01 eV (5). This average amount of energy, which is needed to produce one electron-hole pair, is somewhat dependent on the mass and energy of the primary particle (5).

The electron-hole pairs are immediately swept from the sensitive volume to the oppositely charge electrode. These moving charges induce charges in the external circuit connected to the detector. A typical detector circuit is shown in Fig. (A-4). R_L is the detector load resistor, and V_{bias} is the d.c. detector bias voltage.

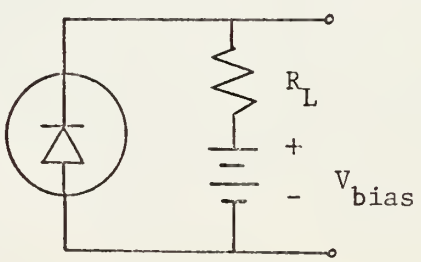

Fig. A-4 Schematic diagram of the detector and external bias circuit

The charge Q induced in the external detector circuit by the motion of a charge Ne through a distance Δx is

$$Q = Nw \frac{\Delta V}{V} \quad , \tag{A-3}$$

where N = total number of ion pairs produced,

w = energy dissipated per ion pair,

V = total potential across the detector,

ΔV = potential difference corresponding to Δx.

It is assumed for Eq. (A-3) that no charge is trapped in the detector. When the electron-hole pairs released in the detector reach the collecting electrodes, no more charge is induced in the detector circuit.

The induced charge Q produces a voltage pulse V_o in the associated detector circuitry:

$$V_o = \frac{Q}{(\Sigma C)} \quad , \tag{A-4}$$

where (ΣC) = sum of all amplifier input capacitances (detector, cables, amplifier housing, etc.).

It has been found that the capacitance of lithium-drifted silicon detectors remains relatively constant as the detector bias voltage is varied (21).

The detector charge collection time is the time required for the electron-hole pairs generated by incident radiation to move to their respective electrodes. The collection time for holes is longer than for electrons, assuming they both travel the same distance. Technical Measurements Corporation (TMC) (20) gave the following equation and constants to be used to compute the collection time for their lithium-drifted silicon detectors:

$$t_c = \frac{W_{dd}^2}{\mu V_{bias}} \text{ seconds} , \qquad \text{(A-5)}$$

where W_{dd} = depth of depletion region (cm.),

μ = mobility of particular charge carrier ($1350 \frac{cm^2}{sec\ Volt}$ for electrons, $480 \frac{cm^2}{sec\ Volt}$ for holes),

V_{bias} = detector bias (Volts).

Accurate determination of the particle energy by a lithium-drifted detector requires that all of the ions be collected at the electrodes of the detector. Several processes work to oppose complete ion collection. Trapping and recombination may prevent released electrons and holes from traversing the detector. Trapping of both electrons and holes may occur at crystal imperfections. Such trapping may set up a space charge which reduces the electric field in the region. Recombination of charge carriers may occur at recombination centers along the path of the primary particle before the charges are separated. This phenomenon is especially important for heavy ionized particles such as alpha particles and fission products. The recombined pair cannot contribute to the detector signal.

Lithium-drifted silicon detectors have been used to detect many kinds of nuclear particles: alpha, beta, gamma, and fission fragments. Sensitive volumes as thick as 1 cm have been constructed by carefully controlling the lithium-ion-drifting process (21). The wide range of depletion depths available allows one to discriminate against detection of unwanted particles which have mean path lengths greater than the detector depletion layer.

Lithium-drifted silicon detectors offer great utility in particle energy spectrometry. Their resolution capability is greater than that of scintillation crystals. Low cost, reliability, and convenience of operation

recommend the use of lithium-drifted detectors for applications requiring good energy resolution. Lithium-drifted detectors are thus an important class of detectors offering much flexibility in particle research.

APPENDIX B

Variance and Mean of the Total Energy Resolution Spreading Normal Distribution Due to Normally Distributed Energy Resolution Effects

Assume that E_1 and E_2 are independent random energy variables, normally distributed. Each variable corresponds to the energy contribution of a particular energy resolution spreading effect, such as amplifier noise. $p_1(E_1)$ and $p_2(E_2)$ are the normal distribution functions giving the relative frequency of appearance per unit energy of the random energy variables E_1 and E_2:

$$p_1(E_1) = \frac{1}{\sqrt{2\pi}\,\sigma_1} \exp\left\{ \frac{-(E_1-\bar{E}_1)^2}{2\sigma_1^2} \right\} , \qquad \text{(B-1)}$$

and

$$p_2(E_2) = \frac{1}{\sqrt{2\pi}\,\sigma_2} \exp\left\{ \frac{-(E_2-\bar{E}_2)^2}{2\,\sigma_2^2} \right\} , \qquad \text{(B-2)}$$

where

σ_1 = standard deviation of $p_1(E_1)$,

σ_2 = standard deviation of $p_2(E_2)$,

$\bar{E}_1$ = mean of $p_1(E_1)$ distribution,

$\bar{E}_2$ = mean of $p_2(E_2)$ distribution.

Let the probability that E_1 has a value between constants a_1 and b_1, i.e., that E_1 is in condition $\{ G \}$, be $P\{ G \}$. Let the probability that E_2 has a value between constants a_2 and b_2 be $P\{ H \}$. If events G and H are independent, the probability that they occur simultaneously is

$$P\{G \cap H\} = P\{G\} \cdot P\{H\} \quad , \tag{B-3}$$

where the symbol $\cap$ signifies the intersection of events G and H.

Since

$$P\{G\} = \int_{a_1}^{b_1} p_1(E_1)\, dE_1 \quad , \tag{B-4}$$

and

$$P\{H\} = \int_{a_2}^{b_2} p_2(E_2)\, dE_2 \quad , \tag{B-5}$$

then

$$P\{G \cap H\} = \int_{a_1}^{b_1} \int_{a_2}^{b_2} p_1(E_1) p_2(E_2) dE_1 dE_2 \quad . \tag{B-6}$$

The probability that the sum of E_1 and E_2 is less than or equal to a constant t is given by

$$P\{E_1 + E_2 \leq t\} = \int \int_{E_1+E_2 \leq t} p_1(E_1) p_2(E_2) dE_1 dE_2 \quad . \tag{B-7}$$

The range of integration of the integral in Eq. (B-7) will be examined with the aid of Fig. (B-1):

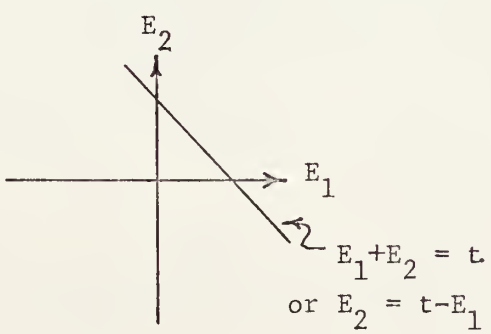

Fig. (B-1) Graph Illustrating Range of Integration of Eq. (B-7).

The integration area of interest in Eq. (B-7) lies below and to the left of the line whose equation is $E_1 + E_2 = t$. Performing the integration in Eq. (B-7) first over E_1 and then over E_2 yields

$$P\{E_1+E_2\leq t\} = \int_{-\infty}^{\infty} dE_1 p_1(E_1) \int_{-\infty}^{t-E_1} dE_2 p_2(E_2) \quad . \tag{B-8}$$

If

$$E = E_1 + E_2 \quad , \tag{B-9}$$

then

$$P\{E\leq t\} = \int_{-\infty}^{\infty} dE_1 p_1(E_1) \int_{-\infty}^{t} dE\ p_2(E-E_1) \quad , \tag{B-10}$$

or

$$P\{E\leq t\} = \int_{-\infty}^{t} dE \int_{-\infty}^{\infty} dE_1 p_1(E_1) p_2(E-E_1) \quad . \tag{B-11}$$

If

$$p(E) = \int_{-\infty}^{\infty} p_1(E_1)\ p_2(E-E_1) dE_1 \quad , \tag{B-12}$$

then

$$P\{x\leq t\} = \int_{-\infty}^{t} p(E) dE \quad . \tag{B-13}$$

Eq.'s (B-1) and (B-2) can be substituted into Eq. (B-12) with the result

$$p(E) = \frac{1}{2\pi\sigma_1\sigma_2} \int_{-\infty}^{\infty} \exp\left\{ \frac{-(E_1-\bar{E}_1)^2}{2\sigma_1^2} - \frac{(E-E_1-\bar{E}_2)^2}{2\sigma_2^2} \right\} dE_1 \quad . \tag{B-14}$$

Eq. (B-14) may be integrated and simplified to

$$p(E) = \frac{1}{\sqrt{2\pi}\sigma} \exp\left\{ \frac{-(E-\bar{E})^2}{2\sigma^2} \right\} , \qquad \text{(B-15)}$$

where

$$\sigma^2 = \sigma_1^2 + \sigma_2^2 , \qquad \text{(B-16)}$$

$$\bar{E} = \bar{E}_1 + \bar{E}_2 . \qquad \text{(B-17)}$$

Eq.'s (B-16) and (B-17) may be generalized easily to predict the standard deviation and mean of the total energy resolution spreading distribution due to n independent component energy resolution spreading distributions:

$$\sigma_{total}^2 = \sigma_1^2 + \sigma_2^2 + \ldots + \sigma_n^2 \qquad \text{(B-18)}$$

or

$$\sigma_{total} = \sqrt{\sigma_1^2 + \sigma_2^2 + \ldots + \sigma_n^2} \qquad \text{(B-19)}$$

and

$$\bar{E}_{total} = \bar{E}_1 + \bar{E}_2 + \ldots + \bar{E}_n . \qquad \text{(B-20)}$$

APPENDIX C

Relationship Between the FWHM and Standard Deviation of a Normal Pulse-Height Energy Distribution

Assume the following normal distribution of particle energy. The integral of this distribution with respect to energy between the limits $-\infty$ and $+\infty$ has been normalized to one.

$$p(E) = \frac{1}{\sqrt{2\pi}\sigma} \exp\left\{\frac{-(E-\bar{E})^2}{2\sigma^2}\right\}, \qquad \text{(C-1)}$$

where E = random energy variable,

$p(E)$ = probability per unit energy of detecting a particle of energy E,

σ = standard deviation in units of energy,

$\bar{E}$ = mean particle energy.

The function $p(E)$ is a maximum at $E = \bar{E}$. The value of $p(E)$ at $E = \bar{E}$ is

$$[p(E)]_{max} = \frac{1}{\sqrt{2\pi}\,\sigma} . \qquad \text{(C-2)}$$

The value of $p(E)$ at the "half-maximum" points is

$$[\,p(E)\,]_{max} / 2$$

or

$$\frac{1}{2\sqrt{2\pi}\,\sigma} .$$

The values of E for $p(E) = \frac{1}{2\sqrt{2\pi}\,\sigma}$ may be obtained by solving for E in the relationship

$$\frac{1}{2\sqrt{2\pi}\,\sigma} = \frac{1}{\sqrt{2\pi}\,\sigma} \exp\left\{\frac{-(E-\bar{E})^2}{2\sigma^2}\right\} . \qquad (C-3)$$

The result is

$$E = \bar{E} \pm 1.177\sigma . \qquad (C-4)$$

The FWHM is defined as the width (energy) between the values of $[\ p(E)\ ]_{max}/2$, therefore

$$FWHM = 2.35\ \sigma . \qquad (C-5)$$

APPENDIX D

Determination of the Mean Energy Loss and Energy Loss Variance Due to Source Self-Absorption

The FWHM of the energy resolution spreading due to source self-absorption in alpha particle sources similar to the source used in this work was given as 8 keV (6). According to Eq. (18), the standard deviation of the mean energy loss due to fluctuations in the mean energy loss of alpha particles traversing a thin absorber (window) is

$$\sigma_{window} = E_o \left[0.01 \, (1-\varepsilon_1)^{1/2} \right] \quad , \tag{D-1}$$

where E_o = alpha particle energy before traversing the absorber,

$$\varepsilon_1 = \frac{\bar{E}_o'}{E_o} \quad ,$$

$\bar{E}_o'$ = mean energy of the alpha particles after traversing the absorber.

The FWHM of the energy loss distribution is

$$FWHM = 2.35 \left[0.01 E_o \left(1 - \frac{\bar{E}_o'}{E_o}\right)^{1/2} \right] \tag{D-2}$$

or

$$FWHM = .0235 \left[E_o \, (E_o - \bar{E}_o') \right]^{1/2} \quad . \tag{D-3}$$

The quantity $(E_o - \bar{E}_o')$ is the mean energy loss of the alpha particles and

$$(E_o - \bar{E}_o') = \left[\frac{FWHM}{(.0235)} \right]^2 \frac{1}{E_o} \quad . \tag{D-4}$$

Since E_o = 5.477 MeV for ^{241}Am alpha particles,

$$(E_o - \bar{E}'_o) = \left[\frac{8 \text{ keV}}{.0235} \right]^2 \left[\frac{1}{5477 \text{ keV}} \right] \quad \text{(D-5)}$$

or

$$(E_o - \bar{E}'_o) = 21 \text{ keV}. \quad \text{(D-6)}$$

Since

$$\text{FWHM} = 2.35 \ \sigma,$$

$$\sigma^2 = \left[\frac{\text{FWHM}}{2.35}\right]^2 \quad \text{(D-7)}$$

and

$$\sigma^2_{\substack{\text{source} \\ \text{self-absorption}}} = \left[\frac{8 \text{ keV}}{2.35} \right]^2 \quad \text{(D-8)}$$

or

$$\sigma^2_{\substack{\text{source} \\ \text{self-absorption}}} = 12 \text{ keV}^2 \ . \quad \text{(D-9)}$$

APPENDIX E

Determination of the Mean Energy Loss and Energy Loss Variance Due to the Detector Window

TMC (20) suggests the use of 0.5 micron of silicon as a representative estimate of the window or insensitive region of their lithium-drifted silicon detectors. The mean energy of the alpha particles incident on the surface of the detector window is obtained by subtracting the mean energy loss due to source self-absorption (see Appendix D) from the emitted energy of ^{241}Am alpha particles. The mean energy of alpha particles incident on the detector face is

$$E_o' = 5477 \text{ keV} - 21 \text{ keV}, \qquad \text{(E-1)}$$

where 21 keV = the mean energy loss due to source self-absorption

or

$$E_o' = 5456 \text{ keV} \quad . \qquad \text{(E-2)}$$

The specific energy loss of 5.456 MeV alpha particles in silicon is approximately 136 keV/micron (27). Since the detector window is assumed to be 0.5 micron of silicon, the mean alpha particle energy loss in the detector window is 68 keV.

Since

$$\text{FWHM} = .0235 \left[\bar{E}_o' \left(\bar{E}_o' - \bar{E}_o'' \right) \right]^{1/2} \quad , \qquad \text{(E-3)}$$

where $\bar{E}_o'$ = mean alpha particle energy before traversing detector window,

$\bar{E}_o''$ = mean energy of the alpha particles having traversed the detector window,

[see Appendix D, Eq. (D-3)], then

$$\text{FWHM}_{\substack{\text{detector}\\\text{window}}} = .0235\ [\ 5456\ \text{keV}\ (68\ \text{keV})\ ]^{1/2} \qquad \text{(E-4)}$$

or

$$\text{FWHM}_{\substack{\text{detector}\\\text{window}}} = 14.5\ \text{keV}\ . \qquad \text{(E-5)}$$

Since

$$\sigma = \frac{\text{FWHM}}{2.35}\ , \qquad \text{(E-6)}$$

then

$$\sigma^2_{\substack{\text{detector}\\\text{window}}} = \left[\ \frac{14.5\ \text{keV}}{2.35}\ \right]^2 \qquad \text{(E-7)}$$

or

$$\sigma^2_{\substack{\text{detector}\\\text{window}}} = 38\ \text{keV}^2\ . \qquad \text{(E-8)}$$

APPENDIX F

Calculation of Detector Capacitance

The detector capacitance was calculated using Eq. (98):

$$C_{det} = \frac{1.1\ k'A}{4\pi W_{dd}} \times 10^{-12}\ F \quad ,$$

where k' = relative permittivity of silicon (12)

A = detector area (1.1 cm^2),

W_{dd} = detector depletion depth (.05 cm).

The final expression for C_{det} may be obtained by substituting the values of the constants given into Eq. (98):

$$C_{det} = \frac{(1.1)(12)(1.1)(10^{-12})}{4\pi\ (.05)}\ F$$

or

$$C_{det} = 23 \times 10^{-12}\ F \quad .$$

APPENDIX G

Tabulation of Experimental Results

Detector Leakage Current Variation
with Detector Bias Voltage

V_{bias} (Volts)	Manufacturer's I_D (μA)	Initial I_D (μA)	Equilibrium I_D (μA)
10	.25	.17	.200
20	---	.22	.365
30	---	.25	.505
40	---	.28	.640
50	.35	.32	.785
60	---	.36	.910
70	---	.39	1.06
80	---	.43	1.21
90	---	---	1.37
100	.39	---	1.56

Energy Resolution Spreading Due to Amplifier Noise
as a Function of Amplifier Time Constant

τ (μsec)	Mean FWHM (keV)
.05	24.1 ± 2.5
.1	16.80 ± .51
.2	11.95 ± .22
.4	8.74 ± .13
.8	8.29 ± .28
1.6	6.06 ± .10
3.2	6.18 ± .04

Variation of Energy Resolution Spreading Due to Detector Noise with Amplifier Time Constant for V_{bias} = 40, 70, and 100 Volts

V_{bias} (Volts)	τ (μsec)	Mean FWHM (keV)
40	.05	12.97 ± .36
40	.10	9.67 ± .16
40	.20	9.01 ± .10
40	.40	9.92 ± .08
40	.80	14.23 ± .08
40	1.6	21.72 ± .22
40	3.2	35.12 ± .09
70	.05	10.24 ± .22
70	.10	8.98 ± .19
70	.20	9.96 ± .17
70	.40	13.69 ± .26
70	.80	19.88 ± .05
70	1.6	33.07 ± .09
70	3.2	52.62 ± .30
100	.05	8.89 ± .68
100	.10	6.39 ± .27
100	.20	12.11 ± .03
100	.40	18.07 ± .08
100	.80	25.08 ± .02
100	1.6	43.36 ± .18
100	3.2	68.50 ± .40

Variation of Excess Energy Resolution Spreading FWHM with Amplifier Time Constant (V_{bias} = 40, 70, and 100 Volts)

V_{bias} (Volts)	τ (μsec)	Mean FWHM (keV)
40	.05	509. ± 40.
40	.10	239. ± 33.
40	.20	113. ± 11.
40	.40	90.4 ± 4.8
40	.80	141.1 ± 6.4
40	1.6	115.6 ± 3.1
40	3.2	173.6 ± 5.3
70	.05	180. ± 16.
70	.10	89.2 ± 0.8
70	.20	63.4 ± 2.2
70	.40	53.3 ± 4.5
70	.80	59.7 ± 2.0
70	1.6	109.6 ± 3.9
70	3.2	212.4 ± 7.2
100	.05	127.3 ± 9.1
100	.10	67.6 ± 2.6
100	.20	38.5 ± 1.9
100	.40	37.8 ± 3.1
100	.80	36.1 ± 2.1
100	1.6	117.6 ± 0.9
100	3.2	249.9 ± 6.5

Variation of Energy Resolution Spreading Due to Detector Noise with Detector Leakage Current and Bias Voltage

V_{bias} (Volts)	I_D (μA)	Mean FWHM (keV)
10	.200	16.45 ± .12
20	.365	11.73 ± .05
30	.505	12.36 ± .09
40	.640	14.23 ± .08
50	.785	15.97 ± .08
60	.910	17.80 ± .14
70	1.06	19.88 ± .05
80	1.21	21.84 ± .13
90	1.37	23.76 ± .07
100	1.56	25.08 ± .02

Variation of the Energy Resolution of the Spectrometer to ^{241}Am Alpha Particles with Detector Bias Voltage (τ=0.8 μsec)

V_{bias} (Volts)	Mean FWHM (keV)
10	811. ± 26.
20	211.8 ± 2.0
30	174.7 ± 5.4
40	139.0 ± 0.5
50	108.2 ± 3.6
60	87.9 ± 6.2
70	65.7 ± 1.8
80	56.3 ± 0.9
90	51.3 ± 4.3
100	47.8 ± 1.5

Variation of the Excess Energy Resolution Spreading FWHM with Detector Bias Voltage (τ = 0.8 μsec)

V_{bias} (Volts)	Mean FWHM (keV)
10	810. ± 26.
20	210.6 ± 2.0
30	173.3 ± 5.4
40	137.0 ± 0.5
50	105.4 ± 3.8
60	84.0 ± 6.5
70	59.7 ± 2.0
80	48.2 ± 1.1
90	41.1 ± 5.4
100	36.1 ± 2.1

Variation of the Energy Resolution of the Spectrometer to ^{241}Am Alpha Particles with Amplifier Time Constant

(V_{bias} = 40, 70, and 100 Volts)

V_{bias} (Volts)	τ (μsec)	Mean FWHM (keV)
40	.05	510. ± 40.
40	.10	224.1 ± 6.4
40	.20	115. ± 11.
40	.40	92.9 ± 4.6
40	.80	143.0 ± 6.3
40	1.6	119.0 ± 3.0
40	3.2	178.1 ± 5.1
70	.05	182. ± 15.
70	.10	92.7 ± 0.8
70	.20	67.4 ± 2.1
70	.40	58.2 ± 4.2
70	.80	65.7 ± 1.8
70	1.6	115.9 ± 3.6
70	3.2	219.5 ± 7.0
100	.05	130.7 ± 8.8
100	.10	72.2 ± 2.4
100	.20	45.3 ± 1.6
100	.40	46.0 ± 2.6
100	.80	47.8 ± 1.5
100	1.6	126.6 ± 0.9
100	3.2	259.8 ± 6.2

ENERGY RESOLUTION OF A LITHIUM-DRIFTED SILICON SEMICONDUCTOR DETECTOR ALPHA PARTICLE SPECTROMETER

by

ROBERT ALAN NUTTELMAN

B.S. Kansas State University, 1967

AN ABSTRACT OF A MASTER'S THESIS

submitted in partial fulfillment of the

requirements for the degree

MASTER OF SCIENCE

Department of Nuclear Engineering

KANSAS STATE UNIVERSITY

Manhattan, Kansas

1969

ABSTRACT

A study of the contributors to the resolution spreading of a lithium-drifted silicon semiconductor detector energy spectrometer to ^{241}Am alpha particles was completed. Theoretical expressions for the energy resolution spreading due to amplifier noise, detector noise, particle statistics, source self-absorption, and detector entrance window were reviewed and combined into one expression. This theoretical expression was a function of, among others, three parameters which could be varied experimentally. These parameters were τ, the amplifier time constant of differentiation and integration, I_d, the detector reverse leakage current, and T, the detector and amplifier ambient temperature. The variation of the full-width at half-maximum (FWHM) of the alpha particle energy distribution with the parameters τ, I_d, and T is presented by comparing experimental and theoretical results. The contributions to the total FWHM of the alpha particle energy distribution due to both detector noise and amplifier noise were predicted and compared with values of FWHM determined by noise measurements.

The theoretical variation of the amplifier FWHM contribution to the total energy resolution with amplifier time constant was found to represent the experimental variation well; however, the amplifier noise was found to be a minor contributor to the total energy resolution spreading.

The measured FWHM contribution due to detector noise was generally lower than that predicted theoretically. The detector noise contribution to the FWHM was found experimentally to vary linearly as $I_d\tau$ over the range of $I_d\tau$ used most commonly. Cooling the detector from $298^{o}K$ to $282^{o}K$ reduced the detector leakage current slightly, but did not decrease the measured FWHM due to detector noise. It is believed that part of the detector leakage current was not responsible for any detector noise.

The FWHM's of the experimental alpha particle energy spectra were generally much larger than those predicted theoretically. It was found experimentally that the best resolution obtained was 45. $\pm$ 2. keV FWHM for 5.477 MeV alpha particles from ^{241}Am. This value was measured with an amplifier time constant of 0.2 μsec and a detector bias of 100 Volts. The predicted resolution spreading for the same operating conditions is 25. keV FWHM. The disagreement between theoretical and experimental FWHM was attributed to charge collection problems. Decreasing the detector temperature from 298°K to 282°K had no significant effect on the resolution.